NORTHWESTERN UNIVERSITY

The Mechanism of Activation and Sensitivity-Tuning of the Calcium-Sensing Receptor

A DISSERTATION

SUBMITTED TO THE GRADUATE SCHOOL

IN PARTIAL FULFILLMENT OF THE REQUIREMENTS

For the degree

DOCTOR OF PHILOSOPHY

Field of Interdisciplinary Biological Sciences

By

Michael Robert Schamber

EVANSTON, ILLINOIS

August 2022

ABSTRACT

The Mechanism of Activation and Sensitivity-Tuning of the Calcium-Sensing Receptor

Michael Robert Schamber

Transfer of information across membranes is fundamental to the function of all organisms and is primarily initiated by transmembrane receptors. This is an allosteric process and involves conformational coupling between ligand-binding domain and signaling domain of a receptor. This allosteric mechanism of activation is unclear for many receptors. Moreover, for many receptors, how ligand sensitivity is fine-tuned and how disease associated mutations modulate receptor conformation to allosterically affect receptor sensitivity are unknown. The calcium-sensing receptor (CaSR) is a dimeric class C G protein-coupled receptor (GPCR) responsible for maintaining stable extracellular calcium levels in vertebrates. CaSR is more broadly activated by polyamines (spermine and spermidine) and polycations (Ca^{2+}, Mg^{2+}, Sr^{2+}, Ba^{2+}, Gd^{3+}, and La^{3+}), and the sensitivity of CaSR to these ligands is augmented by L-amino acids.

At the beginning of this dissertation work in 2016, there were only two published structures of a truncated CaSR construct. These structures provided a basis for understanding the structural rearrangement necessary for receptor activation, but a critical understanding of the individual contributions of polycations and L-amino acids was lacking. Furthermore, the published structures represent a static image and may not represent the dynamic activation process of full length CaSR. Additionally, it has been demonstrated that CaSR from different species can have large differences in ligand sensitivity.

In this study, single-molecule FRET (smFRET), computational analysis, and a cell signaling assay is used to answer these questions. I found that CaSR undergoes unique conformational rearrangements compared to other class C GPCRs owing to specific structural features. Moreover, the analysis of disease associated mutations uncovered a large permissiveness in the architecture of the extracellular domain of CaSR with dynamics and not specific receptor topology determining the effect of a mutation. Finally, a structural hub at the dimer interface allosterically controls CaSR activation via focused electrostatic repulsion. Changes in the surface charge distribution of this hub, which is highly variable between organisms, finely tunes CaSR sensitivity. This design is likely a general tuning design for other dimeric receptors. Together, the studies in this dissertation highlight the importance of probing the conformational change of proteins in real time.

ACKNOWLEDGEMENTS

Research is often thought of as the pursuit of a solitary individual or small group, but there are many people that deserve credit for this work. Without them, this would not exist. I would like to first thank my advisor, Prof. Reza Vafabakhsh for taking me on as his first student and for approaching me about rotating in his lab during the faux poster session in my first year. Through Reza's guidance and support, I have learned much about what it means to be an effective scientist and communicator, and I was fortunate to have a mentor that cares so deeply about the success of their students. Reza provided many opportunities to learn new techniques and explore what I found interesting, and he went out of his way to support my ideas and provide opportunities. Being one of the first members of a lab is a unique opportunity, and I thank you for believing in me. I have been fortunate in my career to have a string of amazing mentors - you most of all.

To my family, without your support, I would not have had the opportunities to pursue this career. I owe all my academic success to my parents and the time you spent in the living room with me as I diligently worked through all the Hooked on Math and Hooked on Phonics, and for providing other educational games that made it fun to learn. It instilled a love for math, science, and learning without which I would not be where I am today. Kaitlin and Allison, your love and support mean the world to me, and I only hope that I have and continue to live up to your expectations. I am proud of all that you have persevered through, have accomplished, and will achieve in the future.

To my Aunts Jeanette, Diane, and Uncle Rex, without your financial support none of this would have been possible, and it is likely that I would never have graduated from the University of California – Santa Cruz much less finished a doctoral program at Northwestern University.

Brandon Liauw, Miranda Jacobs, and Ashley Ives are the best friends I could have hoped for. You have served as my personal and professional sounding boards for over half a decade, and without you I would have surely lost my sanity. Your friendship has made graduate school a wonderful experience, and I only wish a pandemic hadn't kept us from doing more together before we all moved on from graduate school.

LIST OF ABBREVIATIONS

ACP – Acyl Carrier Protein

CaSR – Calcium-Sensing Receptor

CD2 – Compliment of Differentiation 2

CRD – Cysteine-Rich Domain

FRET – Förster Resonance Energy Transfer

GPCR – G-Protein Coupled Receptor

hAGT- human O^6-alkylguanine DNA alkyltransferase

HMM – Hidden Markov Model

mGluR – metabotropic Glutamate Receptor

OGB-1AM – Oregon Green BAPTA -1 AM

PAM – Positive Allosteric Modulator

smFRET – single-molecule Förster Resonance Energy Transfer

TIRF – Total Internal Reflection Fluorescence

TMD – Transmembrane domain

ECD – Extracellular domain

UAA – Unnatural Amino Acid

VFT – Venus Flytrap

For Caroline Elizabeth Roy, no Chicago winter could dampen the warmth you have given me.

TABLE OF CONTENTS

LIST OF FIGURES

LIST OF TABLES

CHAPTER 1: INTRODUCTION TO CASR BIOLOGY

INTRODUCTION

Calcium has long been identified as a critical structural component in organisms where it has been identified in exoskeletons, bones, and teeth. Organisms can store calcium in different ionic compositions. Lower organisms may have an exoskeleton of calcium carbonates or sulfates while higher organisms use calcium phosphate as the primary salt of bones and teeth. It was not until 1883 that calcium was considered a carrier of information when Sydney Ringer realized buffers had been mistakenly made with London tap water instead of distilled water[1]. This early experiment started the history of research into calcium as a signaling molecule.

Inside the cell, the concentration of calcium is regulated, and cytosolic concentrations are approximately 100 nM, but in select compartments, such as the endoplasmic reticulum (ER), calcium concentration can reach to 1 μM[2]. This differential allows calcium flux into the cytosol to act as a carrier of information. It is used to communicate information within a cell to coordinate cellular processes from fertilization, proliferation, differentiation, and cell death. This ambivalence has led to a system of tight spatial and temporal regulation calcium within the cell.

Even outside of the cell, the ionic composition is carefully regulated. Tight control over the ionic composition of the extracellular milieu is a critical biological function of complex organisms, and in humans the concentration of extracellular plasma calcium is maintained between 2.2-2.7 mM[3,4]. To accomplish this, a complex homeostatic system has evolved that is designed to buffer and maintain a near constant concentration of calcium. There are two necessary components

of such a calciostat system: (1) a mechanism to sense and communicate changes of the calcium concentration and (2) a means for tissues to respond and adjust calcium concentrations.

In vivo and *in vitro* evidence for a parathyroid Ca^{2+} sensing mechanism

Surgical removal of the parathyroid gland has been known to cause hypocalcemia in animal models and humans for over 100 years dating back to 1909 where hypocalcemia induced seizures were referred to as tetany[5-8] suggesting it is vital for calcium homeostasis. In addition, intravenous injections of calcium salts to induce hypercalcemia or Ca^{2+} chelators to induce hypocalcemia induce rapid negative and positive changes in serum parathyroid hormone (PTH) respectively[9,10]. PTH regulates serum calcium levels by inhibiting bone resorption[11], excretion from the kidney[12], or intestinal absorption[13,14]. These studies demonstrated that the parathyroid is capable of Ca^{2+} sensing and responds by modulating PTH secretion.

Successful preparation of bovine parathyroid cells using collagenase enabled the assessment of the tissue Ca^{2+} sensing mechanism in tissue and *in vitro*[15]. Similar observations were also made in porcine[16] and human[17-19] suggesting the generality of this mechanism. In every instance, the endogenous secretion of PTH in mammalian parathyroid cells was attenuated by elevation of extracellular Ca^{2+}. The first functional parathyroid cell preparation demonstrated a 60% drop of PTH secretion when stimulated with 1.5 mM Ca^{2+} compared to 0.5 mM Ca^{2+} [15]. Magnesium demonstrated the same ability to decrease PTH secretion, but at much lower potency than Ca^{2+} [15]. It was also demonstrated that stimulation of the β-adrenergic receptor using its agonist, isoproterenol, would stimulate PTH secretion. Together, this indicated the existence of a

specific divalent cation sensor in the parathyroid, and PTH secretion could be stimulated by cAMP producing GPCRs.

Identification of a novel calcium sensor

The relationship between PTH and extracellular calcium had been established by 1983[20,21], but the exact molecule responsible for sensing calcium was not known until 1993 when a novel receptor that conferred calcium sensitivity was successfully cloned from bovine parathyroid tissue[22]. The cloned receptor exhibited pharmacological and functional properties nearly identical to the native receptor in parathyroid cell preparations. Expression and functional characterization in *xenopus* oocytes indicated that the protein was not an ion channel or a transporter[22]. A hydropathy plot identified 7 transmembrane regions – typical of a G-protein coupled receptor (GPCR)[22]. The receptor was named the calcium-sensing receptor, and based on its large extracellular domain and sequence homology, it was classified as a class C GPCR[22].

GPCRs are characterized by their ability to transfer extracellular information across the plasma membrane by coupling to the heterotrimeric G proteins consisting of the G_{α}, G_{β}, and G_{γ} subunits. Of these, the G_{α} subunit is responsible for signaling through a specific downstream effector pathway. There are four main families of G_{α} proteins that are responsible for stimulating or inhibiting cAMP production (G_s and $G_{i/o}$, respectively), Ca^{2+} release from the endoplasmic reticulum (G_q), or by activating Rho GTPases ($G_{12/13}$). It was originally thought that GPCRs would signal through a single G_{α} pathway, but it has become increasingly clear that GPCRs are capable of simultaneously coupling to multiple signaling pathways resulting in more complicated signaling profiles[23]. CaSR is an exceptional example of pleiotropic signaling with evidence to support its

ability to signal through all G_α protein families[24], but most commonly signals through the G_q pathway. It is through this pathway that CaSR activation ultimately reduces PTH secretion.

In addition to Ca^{2+} and Mg^{2+}, CaSR is activated by the polycations, Sr^{2+}, Ba^{2+}, Gd^{3+}, and La^{3+} or charged polyamines like spermidine, spermine, and β-amyloid peptides[25]. The activity of CaSR can also be modulated by L-amino acids, and in the presence of L-amino acids, the sensitivity of CaSR to polycations is increased[26-29]. Upon activation, CaSR couples to the G_q, $G_{i/o}$, $G_{12/13}$, and G_s pathways depending upon cellular context. The well documented coupling to Gq and Gi/o result in activation phospholipase C (PLC) or inhibition of adenyl cyclase (AC), respectively.

Binding of ligands to CaSR activates the receptor enabling it to couple to several G-protein pathways such as the G_q, $G_{i/o}$, $G_{12/13}$, and G_s depending upon cellular context (Figure 1.1). In the G_q pathway, one of the dominant effector pathways of CaSR, phospholipase C (PLC) becomes activated resulting in the cleavage of phosphatidylinositol-4,5-bisphosphate (PIP_2) to form 1,2-diacylglycerol (DAG) and 1,4,5-trisphosphate (IP_3). The production of IP_3 causes the opening of Ca^{2+} channels in the ER resulting in release of intracellular calcium stores from the ER to the cytosol of the cell. The increase in Ca^{2+} and production of DAG activate protein kinase C (PKC) and ultimately results in activation of the mitogen-activated protein kinase (MAPK) signaling pathway. The ability of CaSR to couple to the G_q pathway is frequently used to quantify its sensitivity to ligands, and it was determined to have an EC_{50} for Ca^{2+} of 2-8 mM[28].

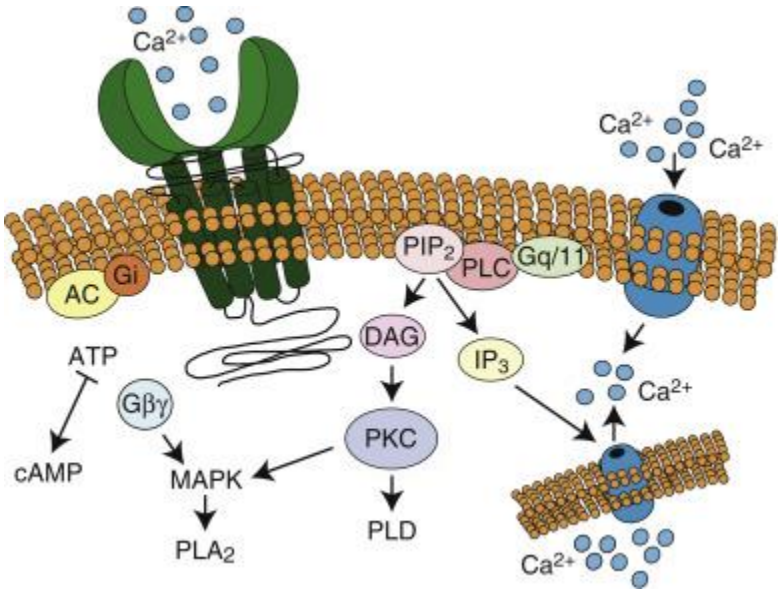

Figure 1.1 – CaSR coupling to G_q and G_i signaling pathways.

Schematic of signaling pathways activated by CaSR. This figure was created by Geoffrey Hendy in Vitamin D, Volume I: Biochemistry, Physiology and Diagnostics, Chapter 28, 2018.

CaSR physiology

Distribution of CaSR throughout the body

While CaSR was first identified in the parathyroid, it has since been identified in many other tissues with diverse roles at the cellular and organismal level beyond calcium homeostasis[30-32] (Figure 1.2a,b). For example, it has been reported to play a role in the contraction of vascular smooth muscle tissue[33,34], but in the skin, it has been implicated in keratinocyte differentiation[35]. During development of the peripheral nervous system, modulation of CaSR function has been

shown to regulate axonal and dendritic growth[36]. Due to its broad expression pattern in the body, mutation of CaSR can result in both calcitropic and non-calcitropic disorders.

a

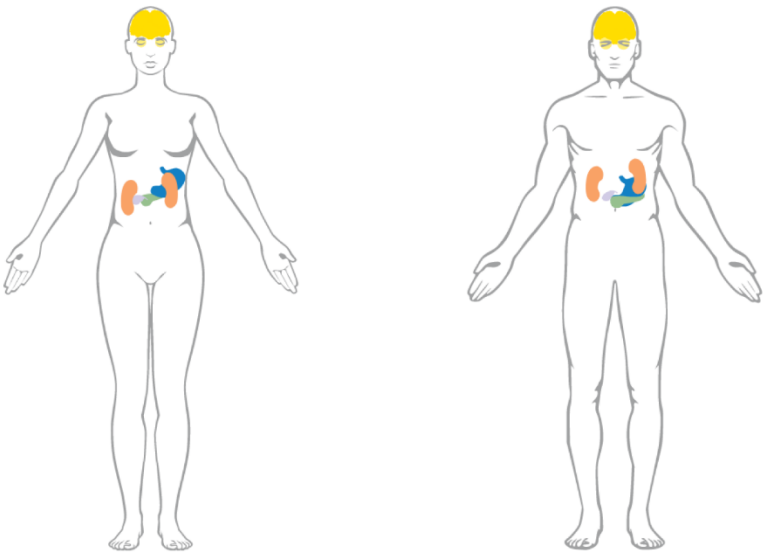

b

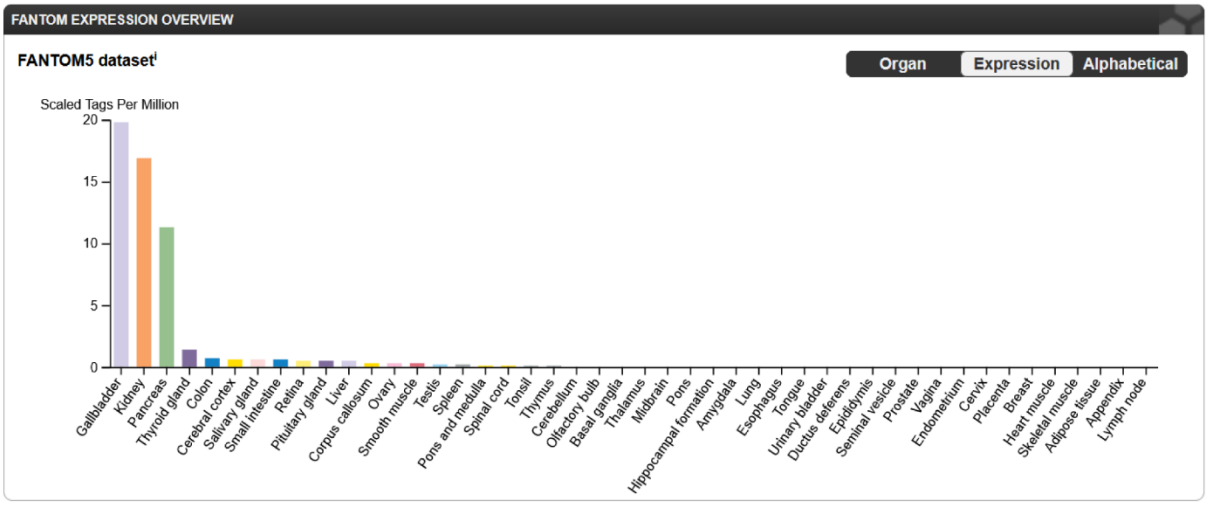

Figure 1.2 – Tissue distribution of CaSR.

a This figure shows the location of CaSR RNA and protein expression in the bod. **b** Summary of the FANTOM5 expression dataset showing the relative RNA expression of CaSR in different tissues. This figure was created by the human protein atlas; version 21.1.

Diseases caused by CaSR

The isolation of bovine, rat, and human CaSR cDNAs[22,37,38] made it possible to assess the relationship between human diseases of calcium metabolism and CaSR. Today, there are over 200 known CaSR mutations in the ECD that are associated with human disease[39,40]. Specifically, mutations resulting in an increase in Ca^{2+} sensitivity result in autosomal dominant hypocalcemia (ADH), Bartter syndrome type V, or hypoparathyroidism. Conversely, mutations that desensitize the receptor ultimately cause elevated calcium levels that can manifest as familial hypocalciuric hypercalcemia (FHH) or neonatal severe primary hyperparathyroidism (NSHPT). But the broader expression profile of CaSR implicates it in non-calcitropic disorders as well.

Due to its expression in neurons[41] and reports of CaSR activation by β-Amyloid peptides have led some to suggest a role in Alzheimer's disease[42]. There has been reports that a mutation altering an arginine-rich retention motif increases CaSR plasma membrane trafficking, and ultimately results in epilepsy[43,44]. There are also reports that CaSR can act as an oncogene or a tumor suppressor depending upon cellular context, and it has been shown to increase the risk of bone metastases[45-52].

CaSR is found in vertebrates

Since its identification, CaSR or CaSR-like genes have been identified throughout the phylogenetic tree where it is expressed in all vertebrates (Figure 1.3) and some non-vertebrate species like the sea tunicates[53]. It is thought to function similarly in vertebrates to maintain calcium homeostasis, but it may serve species-specific roles as well. In fish, where CaSR is expressed in the gills, kidney, tubule, rectal gland, intestine, and olfactory epithelia[55], it is thought to function also as a salinity sensor[54]. Additionally, its broad phylogenetic expression raises the question of how the orthologous receptors have evolved to the specific calcium needs of the organism.

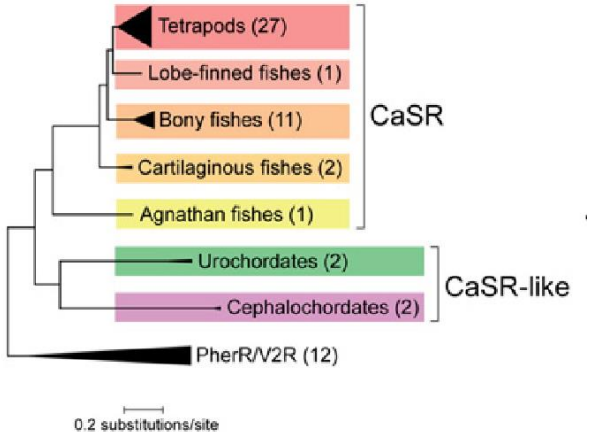

Figure 1.3 – Phylogenetic tree of CaSR and CaSR-like proteins.

The phylogenetic tree estimate of CaSR and CaSR-like proteins with the pheromone and vomeronasal type 2 receptors (PherR/V2R) as the outgroup for reference. This figure was created by Herberger, et al., 2013.

Class C GPCR structure and activation

GPCRs are divided into 5 classes based on their sequence identity and structure. Among these groups, class C GPCRs are constitutive dimers with a large ~600 amino acid extracellular domain that is responsible for sensing its ligand[29,56-61]. For most members of Class C GPCRs, the ectodomain is comprised of a venus flytrap domain (VFT) responsible for ligand recognition, a semi-rigid cysteine-rich domain (CRD), and the canonical GPCR transmembrane domain (TMD) that is responsible for coupling to intracellular effector proteins (Figure 1.4). This architecture presents an interesting question: how is ligand binding transmitted over 100 Å to the intracellular side of the TMD?

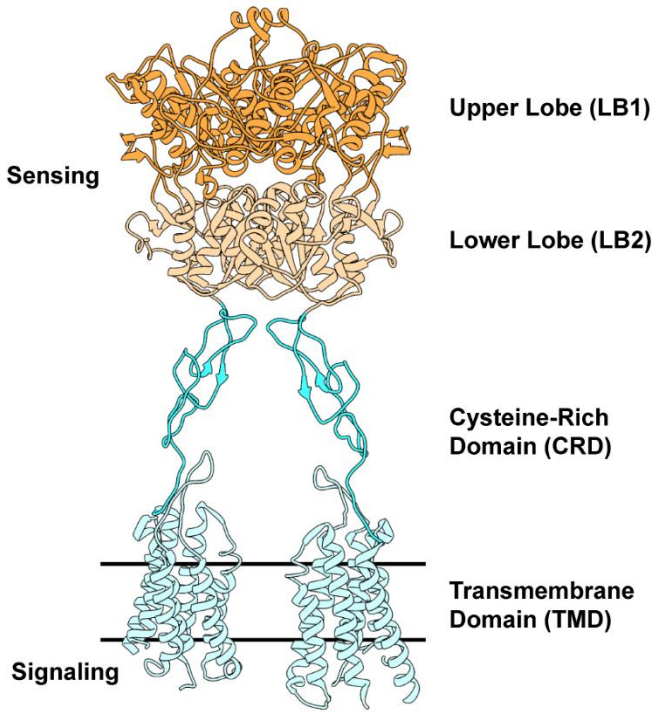

Figure 1.4 – Architecture of the Class C GPCR family.

Ribbon representation the CaSR structure (PDB ID: 7DTW) colored to highlight the upper lobe (orange), lower lobe (pale orange), cysteine-rich domain (cyan), and the transmembrane domain (pale cyan).

In the canonical class C activation mechanism as typified by the metabotropic glutamate receptors (mGluRs), ligand binding to the VFT drives its closure, which in turn results in a large rearrangement of the dimer interface (Figure 1.5a,b). This conformational change results in the overall compaction of the CRD and TMD forming novel CRD and TMD interfaces. There is also a slight twisting of the lower domains that causes the primary helical interface to shift from TM4 and TM5 to TM6[62]. It is through this conformational rearrangement that the TMDs undergo an asymmetric conformational change[63-66] (Figure 1.5c,d) where the TM6 of one TMD shifts upward of 10 Å to expose the G-protein binding pocket[64,65] required for downstream effector function.

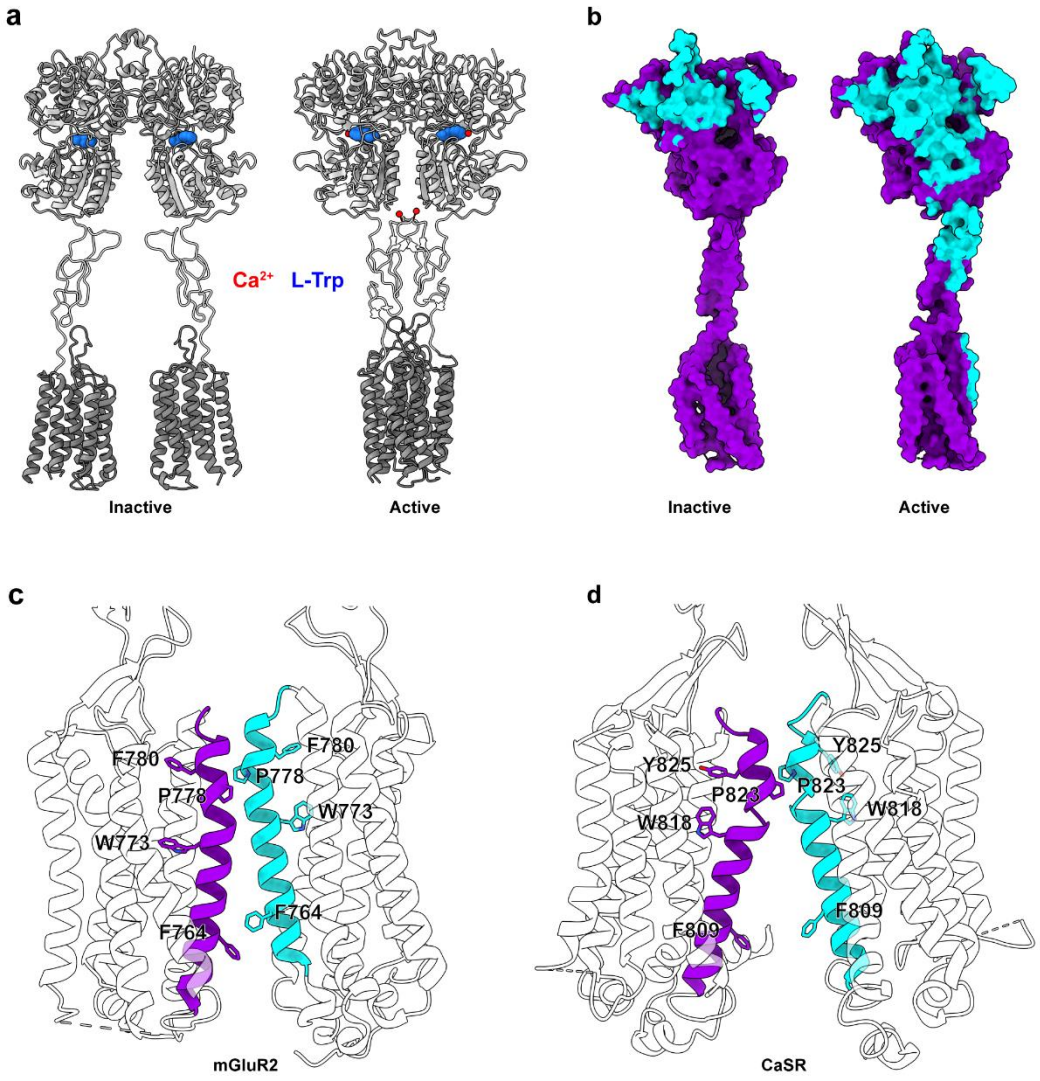

Figure 1.5 – Activation of Class C GPCR creates new dimer interfaces.

A Ribbon representation CaSR with L-Trp (blue) bound in the flytrap or Ca^{2+} (red) and L-Trp (PDB ID: 7DTU, 7DTV). **B** Comparison of the interprotomer interfaces for the inactive and active structures of CaSR (PDB IDs: 7DTW, 7DTV). Contact regions (cyan) show residues within 4 Å of the adjacent protomer. **c,d** Asymmetric TMDs in the active state mGluR2 and CaSR structures (PDB IDs: 7MTS, 7M3F). TM6 are shown as solid cartoon with representative residues shown as sticks to highlight asymmetry.

mGluR1 was the first class C GPCR with a published structures[67]. Accordingly, this structure was used as the basis to more broadly understand the activation mechanism of class C GPCRs. However, the mGluR1 structure does not provide insight to where or how calcium binds to activate CaSR. It was noted that the sequence of the ECD of CaSR has a high number of negatively charged residues. Specifically, glutamate and aspartate account for 32.7% of residues 214-262, and this sequence of amino acids comprises the lower lobe interface between the two protomers. Because of the density of negatively charged residues in this region, it was thought that the ability of positively charged ligands to counter-screen the negative charge led to receptor activation[68,69]. Early work to determine the residues responsible for coordinating Ca^{2+} used an algorithm to computationally predict calcium binding sites, and biochemical and NMR experiments provided functional support for the predicted sites' relevance in the activation of CaSR.

In 2007, Huang, et al. predicted the binding sites of Ca^{2+} using MetalFinder, and they found three potential binding sites consisting of residues E224, E228, E229, E231, E232 (Site 1), E378, E379, T396, D398, E399 (Site 2), and S147, S170, D190, Y218, E297 (Site 3)[70]. These structural motifs were grafted onto a protein, cluster of differentiation 2 (CD2), that does not bind calcium, and the ability of the grafted sites to bind calcium was verified via NMR[70]. Huang, et al. followed up on this work in 2009 expanding the total number of five potential binding sites made up of residues D215, L242, S244, D248, Q253 (Site 4), E350, E353, E354, N386, and S388 (Site 5). Rather than grafting individual sites onto CD2, they chose subdomains of CaSR that are ~200 amino acids in length for deeper analysis[71]. Using NMR, luminescence energy transfer, and ANS fluorescence, they demonstrated the ability of the CD2-CaSR fusions to bind calcium[71]. Mutations

of the proposed binding sites showed a reduction of Ca^{2+}-sensitivity of CaSR, suggesting these residues are responsible for binding Ca^{2+} in full-length CaSR. However, a major limitation of those experiments is that they were done on recombinant fusion proteins and not done on full-length CaSR or even on a dimeric VFT. Additionally, the process of GPCR activation is allosteric, and it has been shown that mutations outside of the ligand binding site may alter the sensitivity of the receptor to its cognate ligand[72]. Therefore, despite insights from structure-function studies, where calcium binds in the receptor and how calcium binding activates the receptor is unclear.

In 2016 the first atomic structure of truncated ECD of CaSR, including the ligand binding sites, was published. Crystal structures of CaSR extracellular domain (ECD) have provided insights into the ligand binding pockets and structural rearrangements upon agonist binding[68,73]. More recently, cryo-electron microscopy (cryo-EM) has provided insights into how conformational changes are propagated to the seven-transmembrane-helix domain (7TM) in the full-length CaSR and how various calcilytic or calcimimetic compounds target CaSR[64,74-76]. In total, 12 structures have been published and show that CaSR does have specific calcium binding sites where there are four consensus binding sites that appear in multiple structures and a fifth present in only one structure (Figure 1.6).

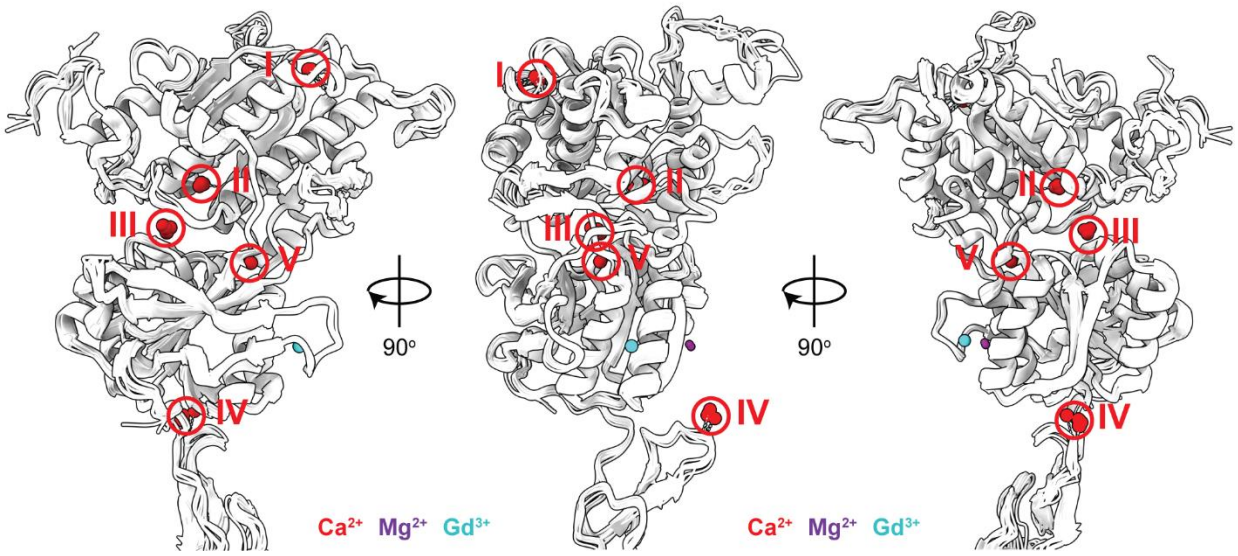

Figure 1.6 – Comparison of active CaSR structures.

a Ribbon representation of CaSR structures bound to ions (PDB IDs: 5K5S, 5FBK, 5FBH, 7M3F, 7M3E, 7DTV, 7DTT, 7E6T, 7DD7, 7DD6, 7DD5, 7M3G). Ca^{2+} binding sites I-V circled in red.

Although it was proposed that CaSR and the mGluRs share a common activation pathway from the very first structures[68,73], there are some noticeable structural differences. Specifically, the VFT domain of unliganded CaSR structure adopts a conformation that more closely resembles the mGluR active conformation[67,68,73]. The similarity between the inactive CaSR structure and active mGluR structures also results in a much smaller conformational change of VFT domain upon the binding of ligand for CaSR. The lack of a published structure with only Ca^{2+} present leaves it unclear what ions and amino acids contributed individually to CaSR activation.

Amino acids and CaSR.

As previously mentioned, CaSR activity is modified by the L-amino acids: His (ΔEC_{50}:1.9), Phe (ΔEC_{50}:1.8 mM), Tyr (ΔEC_{50}:1.8 mM), Trp (ΔEC_{50}:1.6 mM), Cys (ΔEC_{50}:1.6 mM), Ala (ΔEC_{50}:1.4 mM), Thr (ΔEC_{50}:1.1 mM), Asn (ΔEC_{50}:1.1 mM), Gln (ΔEC_{50}:1.0 mM), Ser (ΔEC_{50}:1.0 mM), Glu (ΔEC_{50}:0.9 mM), and the remaining amino acids elicit a $\Delta EC_{50} < 0.7$ mM[29], where ΔEC_{50} is the change in EC_{50} when the amino acid is present. However, there has been controversy over the precise role and mechanism of action of amino acids in the activation pathway of CaSR. In one view, L-amino acids function as co-agonists with calcium, and are equal and required contributors to activation[68,73]. One reason for this is that other members of the Class C family rely on the binding of amino acids in the VFT to activate, and therefore, CaSR must also require amino acids for activation. Some research show amino acids are capable of direct activation of CaSR, but this effect requires a base concentration of 0.5 mM Ca^{2+} to be observed[27]. When the residues that coordinate binding of L-amino acids in the cleft of the VFT were mutated (S170A, Y218S, E297K, S147A, T145I), there was a marked reduction in the ability of CaSR to respond to extracellular Ca^{2+} [68,73]. However, these mutations are not conservative, and they do not preserve either the functional group or the structure of the side chain, and this may result in effects on the structure of CaSR outside of the amino acid binding pocket. Additionally, earlier research demonstrated that different mutations of some of the same residues (S170T, T145A) left the ability of CaSR to sense Ca^{2+} intact[77]. On the other hand, conflicting research suggested that amino acids served merely to allosterically modulate the Ca^{2+} sensitivity of CaSR in a hetero-cooperative manner[78]. This presented an alternative view for the role of amino acids to act as positive allosteric modulators of CaSR.

In this view, the binding of amino acids is neither necessary nor sufficient for receptor activation, but they increase the affinity of CaSR for Ca^{2+} in a hetero-cooperative manner. This model is consistent with the observation that the double point mutant T145A/S170T can disentangle activation of CaSR by Ca^{2+} and amino acid binding[79]. Despite this, the belief that amino acids and Ca^{2+} were co-agonists persists[73,80]because the first structures of CaSR reported that amino acids or their derivatives could remain bound through the purification process and during sample preapartion[24,64,73-75]. Attempts to answer this question through functional studies have been confounded by the possibility of trace contamination by amino acids shed in cell culture, but a recent study overcame this by dialyzing membrane fractions of CaSR expressing cells for 48-hours. In their work, Liu, et al. showed that Ca^{2+} alone was sufficient to activate CaSR[80].

SCOPE OF THESIS

The process of transducing information across the plasma membrane through conformational change is a dynamic and allosteric process. While structural information is available for CaSR, structures represent static snapshots in time, and they do not provide any insight into the dynamic process of activation. This missing information is critical to understand the conditions leading to and regulation of CaSR activation. As such, the goals of this dissertation were three-fold: (1) elucidate the dynamic process of CaSR activation via single-molecule Förster Resonance Energy Transfer (smFRET) and determine the molecular role of amino acids in CaSR activation, (2) identify structural elements that could be the basis of tuning Ca^{2+}-sensitivity and (3) determine the structure-function relationship of disease associated mutations.

To study these questions, I use sequence analysis, signaling assays, and single-molecule FRET (smFRET) imaging and map the conformational dynamics of the extracellular domain of CaSR in the presence of different CaSR ligands. I use a site-specific labeling method based on unnatural amino acid incorporation to avoid local structure disruption caused by conventional labeling strategies. I find that the extracellular domain of CaSR is dynamic, and the receptor continuously samples the active state in the absence of ligands. I show that two unique structural features in CaSR contribute to the unique conformational dynamics of CaSR compared with other class C GPCRs. Specifically, I identify a role for a focused negatively charged patch at the dimer interface of CaSR that limits the receptor residency in the active state via electrostatic repulsion, and I demonstrate an interprotomer loop restricts the conformation space of the VFT of CaSR and reduces the effect of amino acid binding on Ca^{2+} sensitivity. I propose that this design is likely a general mechanism for fine-tuning sensitivity in many dimeric receptors and a plausible strategy for therapies.

CHAPTER 2: DESIGN OF FRET SENSORS TO TRACK CONFORMATIONAL CHANGES OF CASR

INTRODUCTION

The ability to site-specifically label proteins is essential for single-molecule Förster Resonance Energy Transfer (smFRET) experiments. Two powerful methods to label proteins are the genetically encoded SNAP and CLIP tags, which are based off a modified human DNA repair protein, O^6-alkylguanine DNA alkyltransferase (hAGT). They were developed for *in vivo* cell labeling and have commonly been used due to their high labeling efficiency[81]. Both SNAP and CLIP tags utilize the formation of a covalent bond between the enzyme and either an O^6-benzylquanine[81] or O^6-benzylcytosine[82] respectively, which enables irreversible, orthogonal protein labeling. However, the size of these tags, roughly 150 amino acids, makes them suitable for the termini of the protein, which makes them less suitable for intradomain labeling.

In the case of CaSR, the size of the SNAP-tag is approximately the size of a VFT lobe[83] (Figure 2.1) makes it probable the tag will disrupt the overall fold of the protein or the arrangement of internal domains. Due to these considerations, we tested the alternate labeling strategies that rely on genetically incorporated tags of smaller size such as the ACP-tag, SpyCatcher-SpyTag, and incorporation of unnatural amino acids. The incorporation of unnatural amino acids requires only a single point mutation making it the least perturbative and most efficient labeling method available.

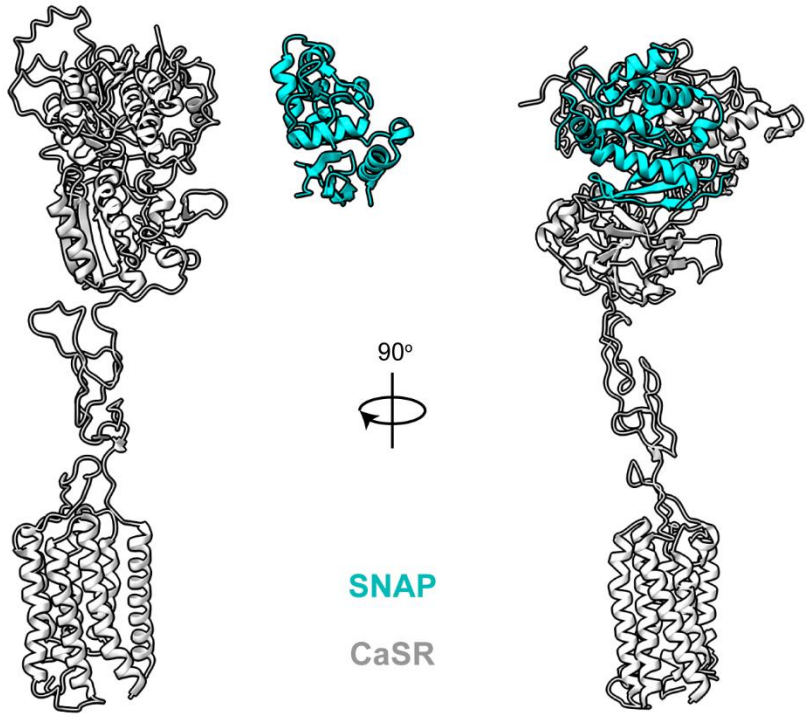

Figure 2.1 – Comparison of CaSR and SNAP-Tag.

Ribbon representation of CaSR (PDB ID: 7DTV) (white/gray) and SNAP-tag (PDB ID: 6Y8P) (cyan) structures for size comparison.

Before sensors are characterized by smFRET, it is necessary to verify that the insertion of the genetically encoded label has not substantially altered the ability of CaSR to sense Ca^{2+}. One of the primary downstream effector systems that CaSR couples to is the G_q pathway, which results in calcium flux from the ER to the cytosol and can be tracked using calcium-sensitive dyes such as Oregon Green Bapta-1 AM (OGB1-AM) or Fura-2 whose fluorescence increases upon binding Ca^{2+}. Using these dyes, it has been demonstrated that activation of CaSR by extracellular Ca^{2+}

results in transitory spikes of intracellular Ca^{2+}. These oscillations are the result of the phosphorylation of T888 in the C-terminal tail of CaSR by protein kinase C (PKC), which decouples CaSR from the G_q pathway[84]. The phosphorylation of T888 is thought to be removed by protein phosphatase-2A (PP2A)[85], which allows CaSR to again couple to the G_q pathway. The frequency of intracellular Ca^{2+} oscillations increase in proportion to the concentration of extracellular Ca^{2+}, and at a sufficiently high concentrations of extracellular Ca^{2+}, the intracellular Ca^2 concentration remain elevated[85]. The use of calcium-sensitive dyes is an established method of quantifying CaSR activation but has predominantly been done in multi-well plates or cuvettes[27,29,77,86]. Here, I demonstrate the use of UAA for protein labeling has superior results for intra-domain labeling compared to the ACP or SpyCatcher-SpyTag methods, and I develop a method of quantifying CaSR activation using confocal microscopy.

RESULTS AND DISCUSSION

Cell surface localization of CaSR

Because CaSR is perennially surrounded by its cognate ligand, it must resist desensitization to affect its biological function. This means there must be a large intracellular pool of CaSR to maintain the cell surface receptor population. There is a large intracellular pool of CaSR that undergoes agonist driven insertional signaling (ADIS) that will promote anterograde trafficking of the receptor from the ER, through the Golgi apparatus, to the plasma membrane[87]. This is in stark contrast with mGluR2, which localizes well to the plasma membrane. An arginine rich region of

the C-terminal tail is responsible for retarding CaSR trafficking[44,87], though the precise signaling and molecular mechanisms governing ADIS is not clear.

It has been reported that partial truncations of the CaSR C-terminal tail can improve trafficking to the membrane[44,88]; however, these are the results of western blotting or fixed immune staining, and they do not show how much of the intracellular CaSR pool remains. Truncation of the C-terminal tail of CaSR-GFP fusion resulted in little, if any, improvement of cell membrane localization (Figure 2.2a,b). Despite the sequence similarity between mouse CaSR and human CaSR (huCaSR), we tested to see if the huCaSR showed increased surface localization in the human derived cell line HEK293T. Surprisingly, our results suggested that mouse CaSR exhibited better surface expression than huCaSR (Figure 2.3a,b). Even with reduced localization compared to mGluR2, we achieved suitable membrane labeling of SNAP-CaSR as verified by confocal microscopy and smTIRF microscopy. Despite the remaining issues with cell surface expression, we moved forward with testing multiple labeling methods.

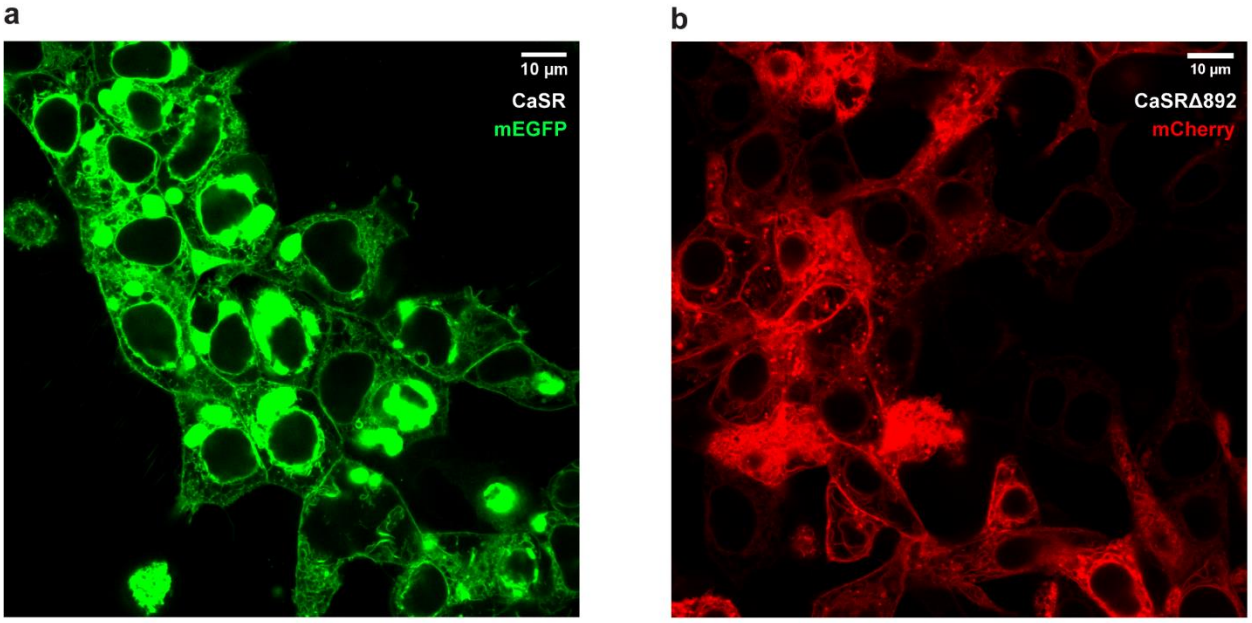

Figure 2.2 – Comparison of CaSR with truncation of C-terminus.

a Confocal image of CaSR c-terminally fused to mEGFP expressed in HEK293T cells. **b** Confocal image of CaSR truncated zxat residue 892 (CaSRΔ892) c-terminally fused to mCherry expressed in HEK293T cells.

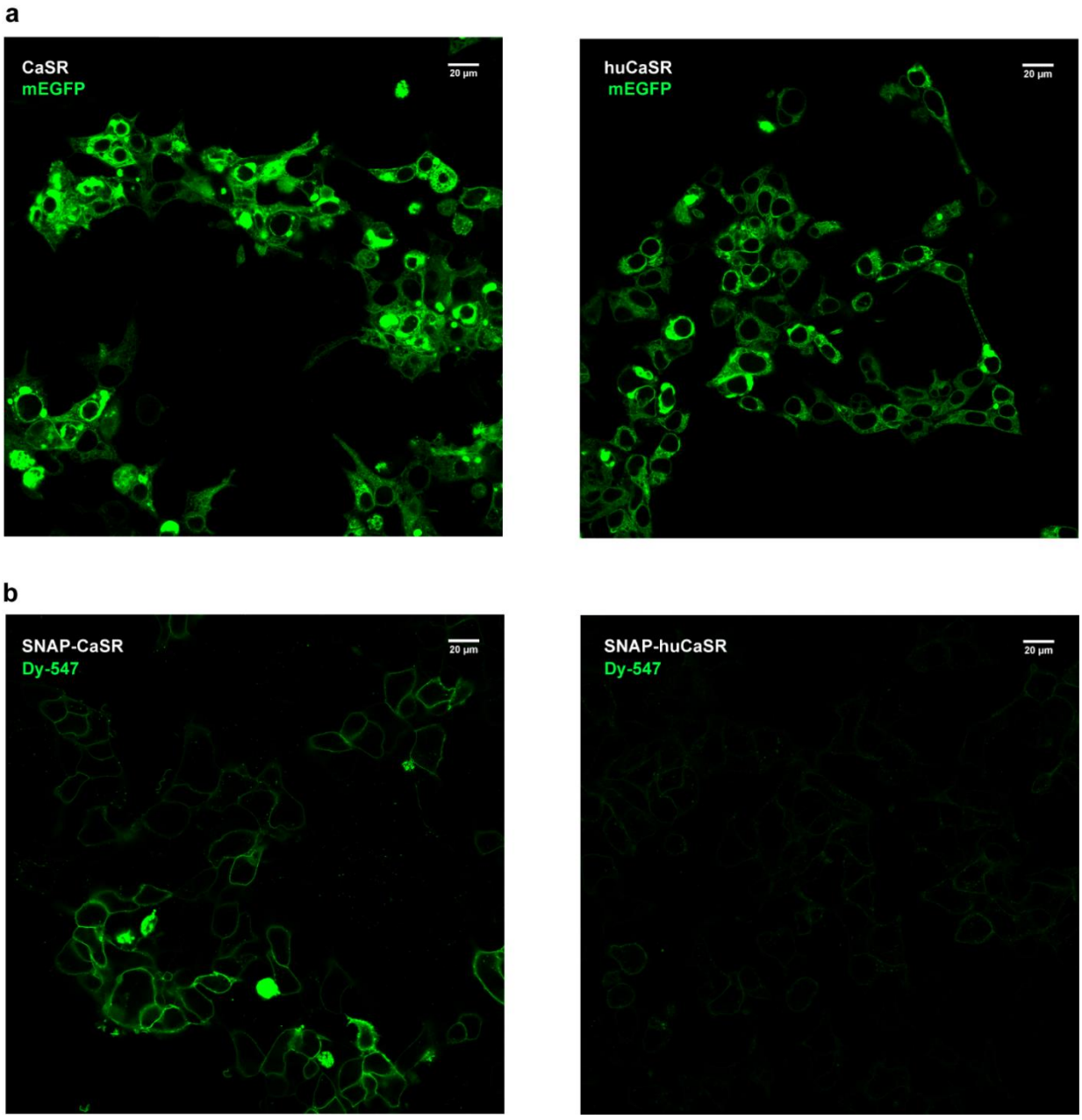

Figure 2.3 – Images of HEK293T cells expressing mouse and human CasR constructs.

a Membrane localization of C-terminal mEGFP CaSR and huCaSR fusion proteins expressed in HEK293T cells. **b** DY-547 labeling of N-Terminal SNAP CaSR and huCaSR fusion proteins expressed in HEK293T cells.

Acp-tag

The acyl carrier protein (ACP) labeling method takes advantage of the post-translational modification of ACP by the Sfp phosphopantetheinyl transferase (Sfp Synthase) to covalently attach fluorophores to a protein of interest [89,90]. While tags derived from the hAGT are 182 amino acids in size, the ACP-tag is only 77 amino acids making it more amenable loop insertion. In fact, The ACP-tag was successfully used to track conformational rearrangement of the Class C GPCR GABAB where it was inserted into an extracellular loop[91]. Based on this, we validated a method of *in vivo* labeling using on an N-terminal fusion of the ACP-tag to mGluR2, which localizes better to the plasma membrane than CaSR. When visualized by smFRET, we can see clear labeling of mGluR2 indicating the method for labeling is effective (Figure).

I created several potential candidates that inserted the ACP tag at residues E412, D480, E515, E536 of a CaSR-mCherry fusion (Figure 2.4a). The fusion of the fluorescent protein mCherry verified the protein was properly folded and could be used to determine labeling efficiency. While confocal results did not suggest successful labeling, we were able to detect some immobilized receptors via smFRET (Figure 2.4b). However, poor co-localization between the ACP linked Cy5 fluorophore and the mCherry fluorescent tag suggests labeling efficiency is too low for useful smFRET experiments (Figure 2.4b). It was not clear if issues with labeling efficiency were caused by tag accessibility or if the relatively large tag affected receptor trafficking. Fortunately, the ACP labeling method was improved when the tag was reduced from the original 77 amino acids to an 8 amino acid minimal peptide sequence [92], and new constructs were created and screened for labeling. Unfortunately, the improved ACP tag failed to show any improvement in labeling.

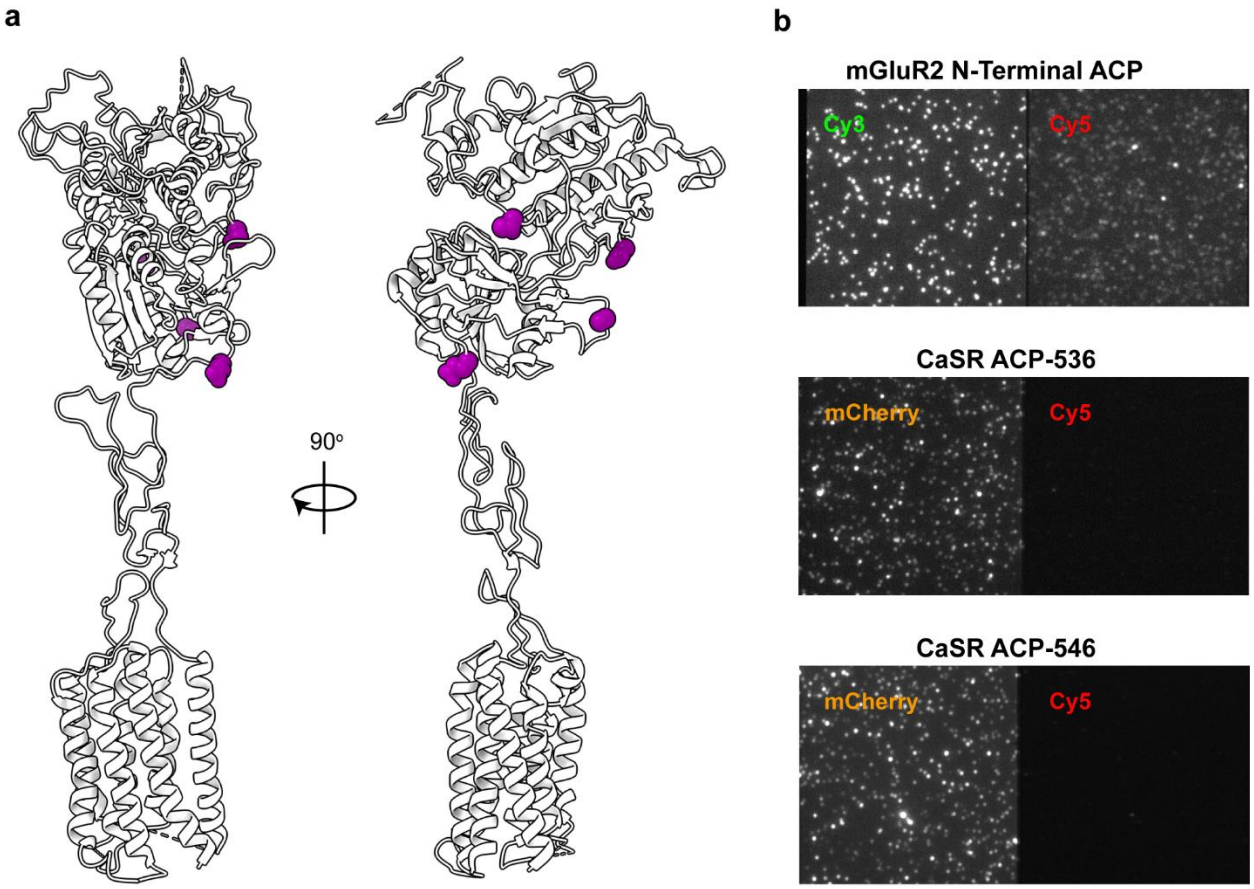

Figure 2.4 – ACP labeling of CaSR.

a Ribbon representation of CaSR (PDB ID: 7DTV). Residues where ACP-Tag was inserted are represented as spheres (purple). **b** Sample images from single-molecule TIRF movies showing the presence of immobilized and fluorescently labeled CaSR.

SpyCatcher-SpyTag

A major limitation of the ACP labeling system that could hinder labeling efficiency is the requirement of three separate components: (1) a tag, (2) an enzyme, and (3) a fluorescent substrate. The SpyCatcher-SpyTag system method for protein labeling that was originally developed for super-resolution microscopy simplifies this system into two components only[93] and has been used a protein ligation method[94]. It relies on a 13 amino acid peptide (SpyTag) 'bait' and a modified domain from the *Streptococcus pyogenes* surface protein (SpyCatcher) pre-labelled with a fluorophore. I inserted the SpyTag into regions I felt would least disrupt the CaSR protein structure (Figure 2.5a), and while this system did see a marked improvement in labeling (Figure 2.5b), downstream analysis showed poor co-localization of Cy3 and Cy5 fluorophores indicating that labeling efficiency was still too poor for smFRET. A phage-display evolved version of the SpyCatcher-SpyTag system improved binding between the two components[95], but also failed to produce results.

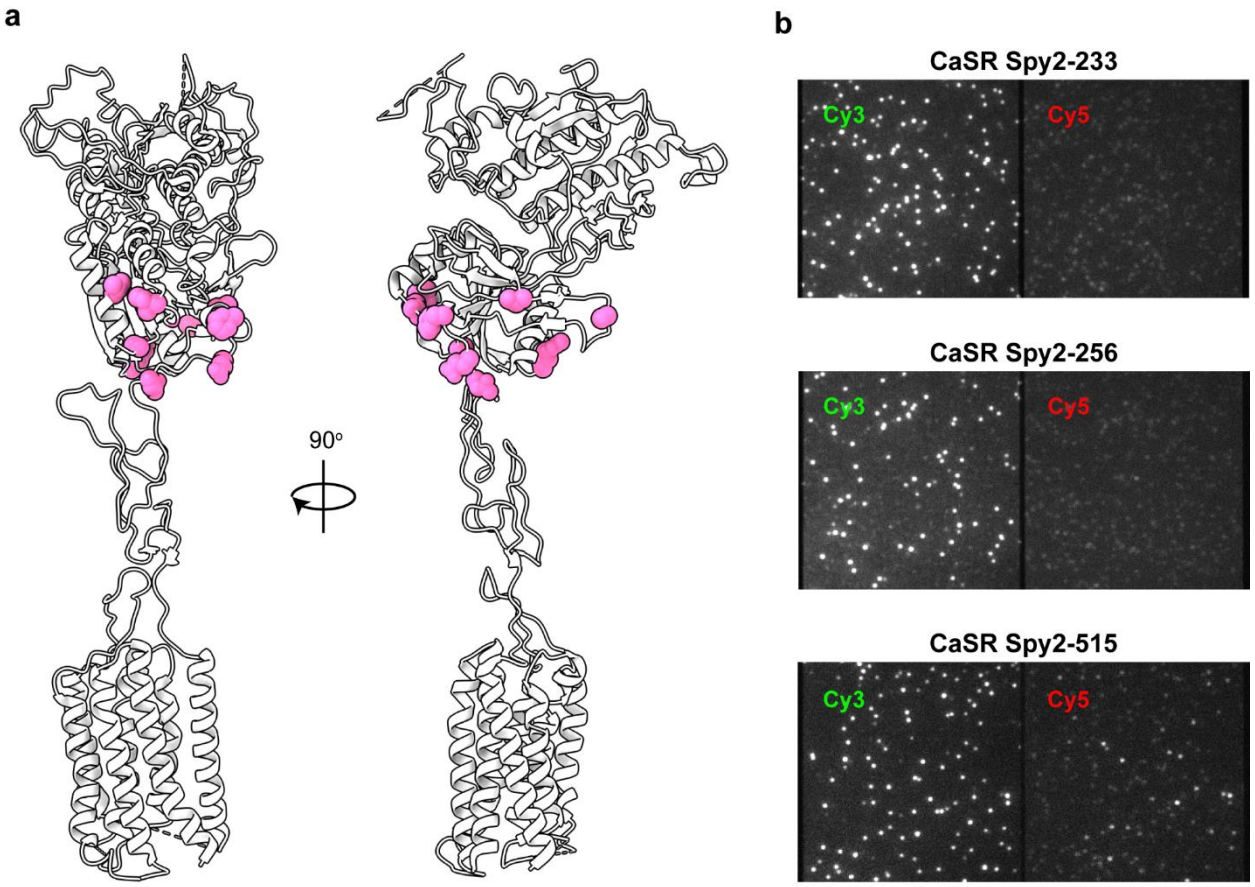

Figure 2.5 – SpyTag-SpyCatcher labeling of CaSR.

a Ribbon representation of CaSR (PDB ID: 7DTV). Residues where SpyTag was inserted are represented as spheres (pink). **b** Sample images from single-molecule TIRF movies showing the presence of immobilized and fluorescently labeled CaSR.

Unnatural amino acids

To truly minimize structural perturbation, we adopted an unnatural amino acid-incorporation strategy of labeling, which was described in 1989 and has since been optimized[96-99]. Co-transfection of an amber codon (TAG) tRNA suppressor, an evolved tRNA synthetase, and a plasmid with a TAG point mutation in our protein of interest, we were able to express recombinant CaSR with an 4-azido-l-phenylalanine to facilitate click chemistry with alkyne dyes[100]. Eighteen constructs were created (Figure 2.6a) to screen for optimal expression and labeling. There were multiple successful hits proving it to be a much more effective method of protein labeling (Figure 2.6b). Interestingly, changing the location of UAA incorporation by a single amino acid could result in different labeling efficiencies (Figure 2.6c) showing that even UAA-based labeling strategies need to be screened for an optimal position.

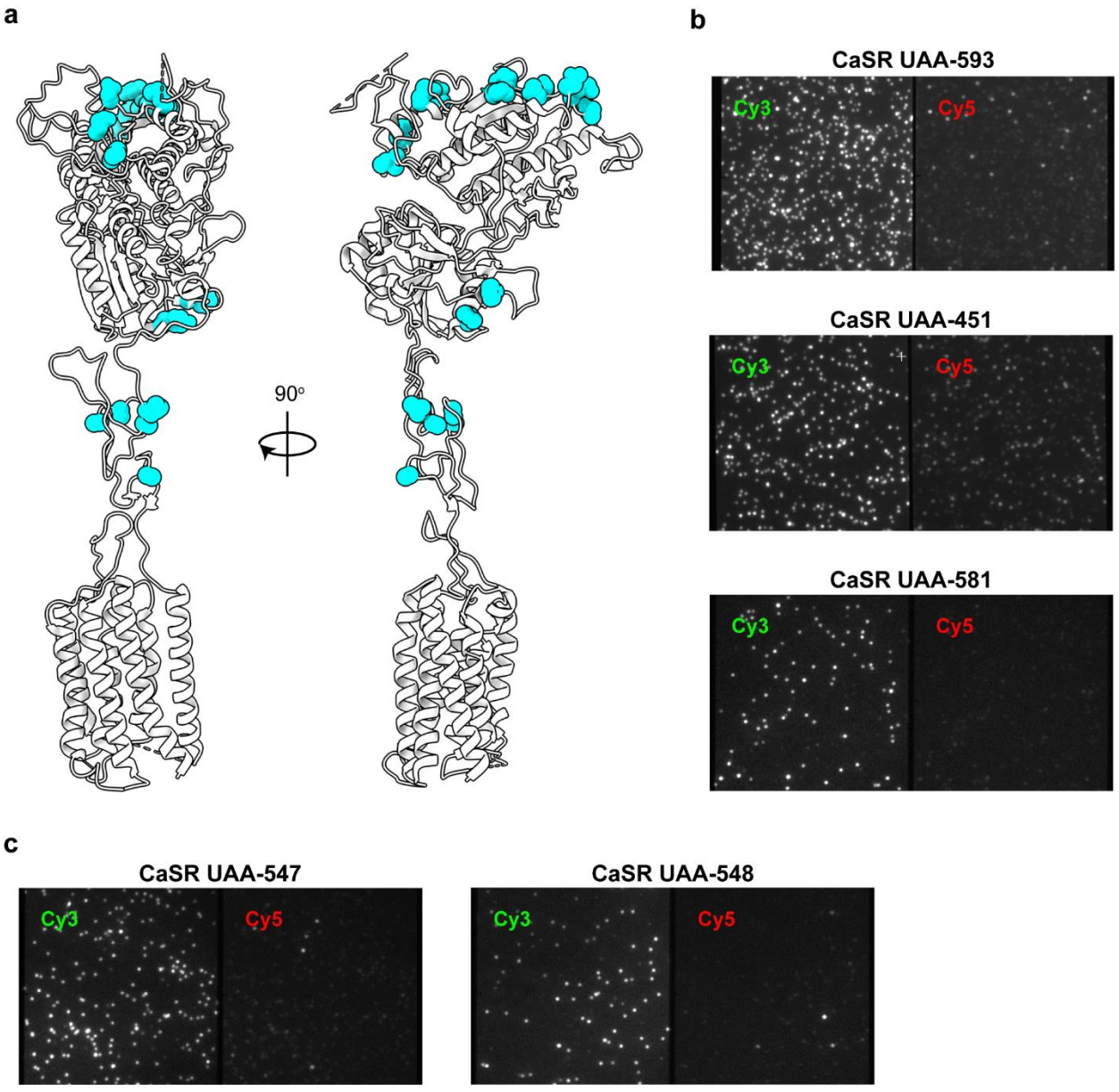

Figure 2.6 – UAA labeling of CaSR.

a Ribbon representation of CaSR (PDB ID: 7DTV). Residues where an UAA was inserted are represented as spheres (cyan). **b, c** Sample images from single-molecule TIRF movies showing the presence of immobilized and fluorescently labeled CaSR.

Developing a confocal microscopy signaling assay for CaSR

HEK293T cells expressing CaSR loaded with the Oregon Green BAPTA-1 AM (OGB1-AM) (Figure 2.7a) calcium sensitive dyes were sequentially stimulated with varying concentrations of calcium. Initially, quantification of the response was done on the entire field of view, but due to the length of data acquisition, analyzing the entire field of view made the data more susceptible to significant drift. Quantification of single cells proved to be a more reliable means of quantifying the response, but it presented another problem. A major limitation of this dye is the inability to control for the concentration of dye within the cell, which affects the brightness of the cell and results in the brightest cells contributing more to the final response than others (Figure 2.7a).

Cells could be normalized so that each cell contributed equally using:

$$Normalized\ Intensity(t) = (I_t - I_{min})/(I_{max} - I_{min})$$

where I_t is the fluorescence intensity at time t, I_{min} is the minimum intensity for the cell, and I_{max} is the maximum intensity for the cell (Figure 2.7b). Individual cells were then summed together and normalized by the total number of cells in the data set so that all datasets contribute equally to the calculation of potency (Figure 2.7c). The strength of response was quantified for each concentration of Ca^{2+} by integrating the normalized intensity during stimulus, which is used for fitting to a dose response curve.

To aide with downstream analysis of the calcium imaging data, I developed the *calcium-analysis* R package to make it available to other lab members. The package enables the normalizing and visualization of many individual cell traces automatically, and cells that do not respond or

show significant drift can be removed from further analysis. It integrated over a specified window, and these values could be exported to origin for fitting to a dose-response curve using a log-likelihood model. Using this method, CaSR had an EC50 of 2.84 mM (figure), which is within the established sensitivity range of 2-8 mM[28].

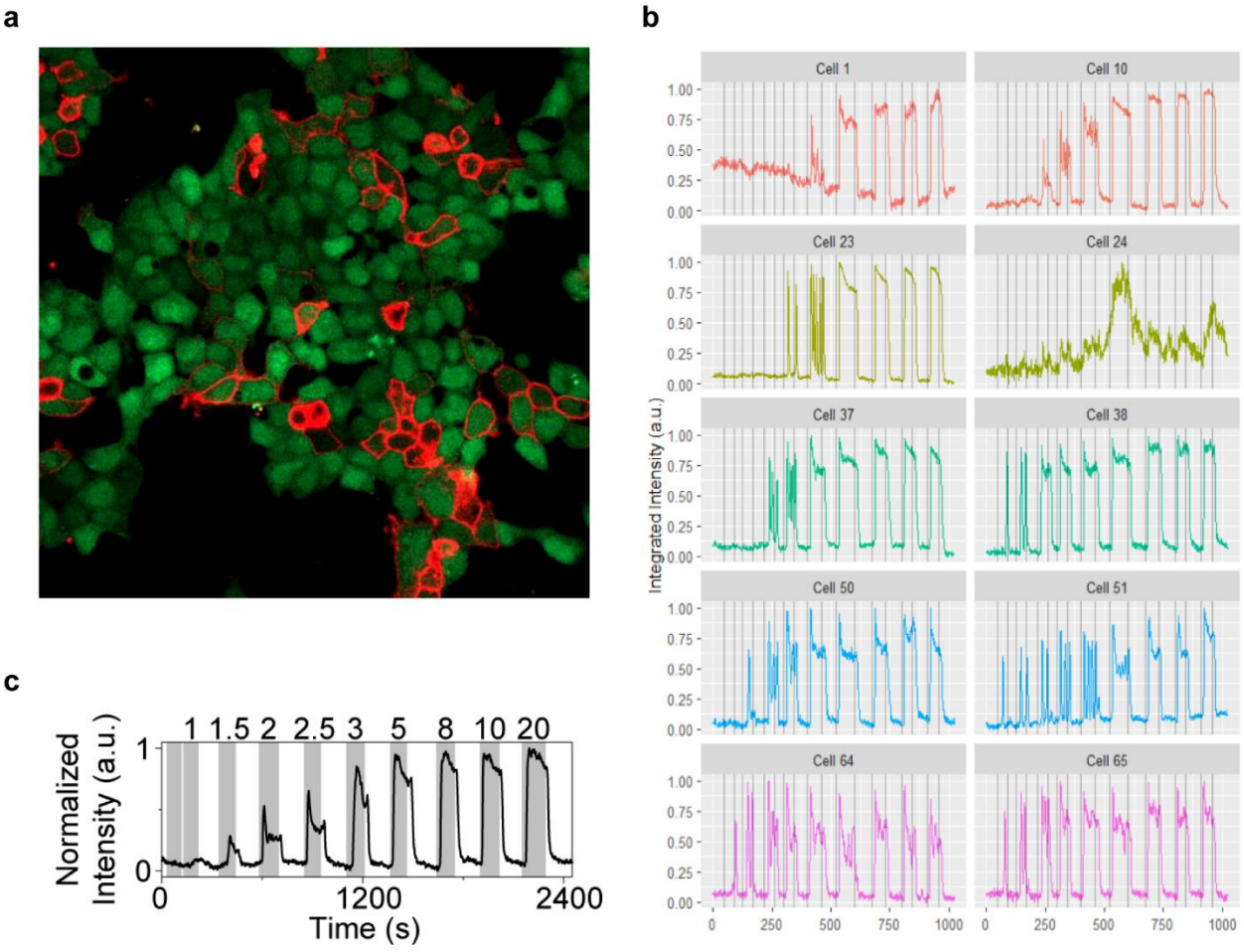

Figure 2.7 – Workflow of calcium imaging.

a Sample confocal image of cells expressing CaSR (red) and labeled with DY-649 and loaded with OGB1-AM dye (green). **b** Sample OGB1-AM fluorescence intensity traces for individual cells. **c** Example summed intensity trajectory used for determining dose-response relationship.

DISCUSSION

In the pursuit of optimizing labeling strategies, over 37 human and mouse CaSR constructs were made, and their results summarized in (Table 2.1). The ACP and SpyCatcher-SpyTag methods were not able to reliably label within a domain, and the placement of the tag requires significant optimization; however, they are capable of labeling protein termini. Incorporation of unnatural amino acids for site-specific bioconjugation overwhelmingly proved to be the most successful strategy available. One limitation of the method used is the reliance on copper for catalyzing the click reaction drastically reduces cell viability. Fortunately, other click reactions chemistries are available that do not rely on copper catalysis are much gentler on cell viability. A method of quantifying CaSR activation using confocal microscopy was developed, and an accompanying R package, *calcium-analysis*, was created for data analysis.

Labeling Method	Site of Modification (Residue #)	Labeling Method	Site of Modification (Residue #)	Labeling Method	Site of Modification (Residue #)
ACP	412	SpyTag2	256	UAA	61
ACP	480	SpyTag2	264	UAA	90
ACP	515	SpyTag2	288	UAA	92
ACP	536	SpyTag2	290	UAA	203
ACP17	480	SpyTag2	508	UAA	349
ACP17	515	SpyTag2	515	UAA	451
ACP17	536	SpyTag2	533	UAA	453
SpyTag1	515	UAA	23	UAA	522
SpyTag1	536	UAA	28	UAA	547
SpyTag1	541	UAA	29	UAA	548
SpyTag1	722	UAA	31	UAA	579
SpyTag2	233	UAA	59	UAA	581
				UAA	593

Table 2.1 – List of created potential FRET sensors.

MATERIALS & METHODS

Molecular cloning

A mouse and human CaSR construct with a C-terminal FLAG-tag in pcDNA3.1^{+} expression vector was purchased from GenScript (ORF clones: OMu14241D and OHu15961) and validated by sequencing (ACGT). A SNAP-tag (pSNAP$_f$, NEB) flanked by GGS linkers was inserted at position 21 using HiFi DNA Assembly Master Mix (NEB). Truncation mutation Δ892

of CaSR was created using a QuikChange site-directed mutagenesis kit (Qiagen). The SNAP-tag CaSR construct was used as the template for mutation of amino acid E593 to an amber codon (TAG) via QuikChange mutagenesis. AscI restriction sites were used to insert mEGFP (mEGFP-N1, gift from Michael Davidson (Addgene plasmid # 54767) at the C-terminus of the GenScript constructs, and CaSR-mEGFP was used as the template for mutation of amino acid D451 to an amber codon (TAG) via QuikChange mutagenesis. All plasmids were verified by sequencing (ACGT). DNA restriction enzymes, DNA polymerase and DNA ligase were purchased from New England Biolabs. Plasmid preparation kits were obtained from Macherey-Nagel.

Cell culture conditions

Cells (HEK293T) purchased from Sigma were maintained in culture media consisting of: high glucose DMEM (Corning), 10% (v/v) fetal bovine serum (GE Healthcare), 100 unit/mL penicillin–streptomycin (Gibco), and 10 mM HEPES (pH 7.4, Gibco). Cells were incubated at 37 °C under 5% CO_2 during maintenance. A 0.05% trypsin–EDTA solution (Gibco) was used to passage cells. For unnatural amino acid-containing protein expression, the growth medium was supplemented with 0.65 mM 4-azido-l-phenylalanine (Chem-Impex International). All media were filtered by 0.2 μM aPES filters (Fisher Scientific).

Transfection and protein expression

At 24 h before transfection, HEK293T cells were cultured on 18-mm polylysine-coated glass coverslips (VWR). For unnatural amino acid labeling, one hour before transfection, cell culture medium was changed to growth medium supplemented with 0.65 mM 4-azido-l-phenylalanine. CaSR plasmids with amber codons as described above and pIRE4-Azi plasmid

(pIRE4-Azi was a gift from I. Coin, Addgene plasmid no. 105829) were co-transfected (1:1 w/w) into cells using Lipofectamine 3000 reagents (Invitrogen) (total plasmid: 1.6 μg per 18-mm coverslip). Growth medium containing 0.65 mM 4-azido-l-phenylalanine was refreshed after 24 h and the cells were grown for another 24 h (total 48 h expression). On the day of the experiment, 30 min before labeling, 4-azido-l-phenylalanine supplemented growth medium was removed, and cells were washed twice by extracellular buffer solution containing 128 mM NaCl, 2mM KCl, 2.5 mM $CaCl_2$, 1.2 mM $MgCl_2$, 10 mM sucrose, 10 mM HEPES, and pH 7.4 and were kept in growth medium without 4-azido-l-phenylalanine. Before the addition of labeling solution (below), cells were washed once with extracellular buffer solution. For SNAP-tag experiments, CaSR plasmids as described above were transfected into cells using Lipofectamine 3000 (Invitrogen) (1 μg per 18-mm coverslip).

SNAP-tag labeling in live cells

For SNAP labeling of the N terminus VFT domain, cells were incubated with 4 μM of benzylguanine Alexa-647 (NEB) and 4 μM of benzylguanine DY-549P1 (NEB) in extracellular buffer for 30 min at 37 °C. To remove excess dye after labelling, the coverslip was gently washed twice in extracellular buffer.

Unnatural amino acid labeling in live cells by azide-alkyne click chemistry

A modified version of previously reported protocols[100,101] was used to label the incorporated 4-azido-l-phenylalanine in live cells. For labelling, the following stock solutions were made: Cy3 and Cy5 alkyne dyes (Click Chemistry Tools) 10 mM in DMSO, BTTES (Click Chemistry Tools) 50 mM, copper sulfate (Millipore Sigma) 20 mM, aminoguanidine (Cayman

Chemical) 100 mM and (+)-sodium l-ascorbate (Millipore Sigma) 100 mM in ultrapure distilled water (Invitrogen). In 656 µl of extracellular buffer solution, Cy3 and Cy5 alkyne dyes were mixed to a final concentration of 20 µM and 16 µM of each, respectively. A solution of fresh copper sulfate solution and BTTES (1:5 molar ratio) was premixed and then added to a final concentration of 150 µM and 750 µM, respectively. Next, aminoguanidine was added for a final concentration of 1.25 mM and (+)-sodium l-ascorbate was added for a final concentration of 2.5 mM. The total labeling volume was 0.7 mL. The completed labeling mixture was kept at 4 °C for 8 min followed by 2 min at room temperature and kept in darkness before addition to the cells. Cells were washed before addition of the labeling mixture. During labeling, cells were kept in the dark at 37 °C and 5% CO_2 for 10-15 min. Post labeling, extracellular buffer was used to wash the cells twice.

Calcium Mobilization Assay

Coverslips with HEK293T cells expressing N-terminal SNAP CaSR were briefly washed in extracellular buffer solution before they were placed into 600 µL of extracellular buffer solution with 4 µM Oregon Green Bapta-1 AM (OGB1-AM) (ThermoFisher) and 2 µM of benzylguanine Alexa-647(NEB). During labeling, cells were kept in the dark at 37 °C and 5% CO2 for 30 min. Cells were washed twice after labeling with extracellular buffer solution to remove excess dye and were transferred to a flow chamber (Chamlide) for live-cell confocal imaging. The flow chamber was attached to a gravity flow control system (ALA Scientific Instruments) to switch between buffer application during experiments. Buffers were applied at the rate of 5 mL/min. A zero-calcium buffer (128.75 mM NaCl, 2 mM KCl, 1 mM $MgCl_2$, 0 mM $CaCl_2$, 20 mM HEPES, 5.5 mM D-Glucose, pH 7.4) and a high-calcium buffer (68.75 mM NaCl, 2 mM KCl, 1 mM $MgCl_2$,

40 mM $CaCl_2$, 20 mM HEPES, 5.5 mM D-Glucose, pH 7.4) were mixed to achieve desired $CaCl_2$ concentrations while maintaining constant osmolarity.

Time-series data was collected using a Zeiss Axio Observer 7 inverted confocal microscope equipped with an LSM800 GaAsP-PMT detectors and a Plan-Apochromat 40x objective (Zeiss, 1.3 numerical aperture, oil immersion). A pixel size of 0.312 µm x 0.312 µm resulted in field of view 319.45 µm x 319.45 µm. 488nm and 640 nm lasers were used to excite OGB1-AM and Alexa-647 dyes, respectively. Data was acquired at ~1 Hz.

Movies were analyzed in Fiji [102] by manually drawing a region of interest (ROI) centered on individual cells that showed labeling with Alexa-647 dye (50 to 100 cells per field of view resulting in a minimum of 150 cells across 3 individual biological replicates) indicating cells expressing CaSR. Cells without labeling did not respond to changes extracellular calcium. Built-in Fiji functions were used to calculate the integrated intensity for the ROI of the OGB1-AM signal over all frames. Cell response profiles were visualized and normalized by $y(t) = I_t - I_{min} / I_{max} - I_{min}$ where I_t is the intensity at time t, and I_{max} and I_{min} are the maximum and minimum values for the cell response profile using custom R scripts. Cells that did not respond to extracellular calcium or showed drift were discarded (10% to 25% of all cell ROIs). Response profiles of individual cells were summed and treated as a single ROI before quantification of response and fitting of a dose-response curve. Cellular response was quantified by integrating the response curve during application of extracellular calcium for each concentration. Dose-response curves were calculated using OriginPro (OriginLab) by fitting to $y(x) = A1 + \frac{(A2-A1)}{\left(1+10^{((LOGx0-x)*p)}\right)}$ where *A1* is the bottom asymptote, *A2* is the top asymptote, *LOGx0* is the center, and *p* is the hill slope.

CHAPTER 3: THE ACTIVATION OF CASR TRACKED BY SMFRET

INTRODUCTION

GPCRs are the largest family of allosteric membrane receptors in human. Among them, class C GPCRs are constitutive dimers with ~600 amino acid extracellular domain that, in some members, are covalently linked[24,103] (Figure 3.1a). Members of class C GPCRs include mGluRs, $GABA_BRs$, CaSR, and sweet and umami taste receptors, and are activated by L-amino acids and ions[29,67,104,105]. The canonical ligand recognition and binding site in class C GPCRs is within the conserved bilobed Venus flytrap (VFT) domain[67,68,73,74,105], which is evolutionarily related to bacterial periplasmic amino acid-binding proteins (PBPs), such as the leucine-binding protein and the leucine/isoleucine/valine-binding protein[64,65,75,76,83,106].

Because mGluRs and CaSR have a similar domain architecture, high structural homology (RMSD=1.7 Å) it is believed they possess a common activation mechanism[73]. Despite their shared ability to bind amino acids, they are required for mGluR activation, but are not required for CaSR activation[77]. The structural basis of this difference is unknown. In this study, I use smFRET to visualize in real-time the activation of CaSR in response to differing concentrations of Ca^{2+} and L-Trp. The VFT of CaSR has at least two FRET states that correspond with the active and inactive FRET conformations while the CRD demonstrates at least 4 FRET states that correspond to the inactive, active conformations, and two intermediates not found in published structures. The active

FRET states of both VFT and CRD were stabilized by Ca^{2+} alone while L-Trp is unable to stabilize the active FRET state of either the VFT or CRD of CaSR by itself, but L-Trp does enhance the ability of Ca^{2+} to increase the occupancy of the active FRET states, consistent with published data. Additionally, I show disrupting contacts made by an interprotomer loop through mutation or truncation of the loop increases the effect of L-Trp on the Ca^{2+} -sensitivity of CaSR.

RESULTS

Mapping the conformational dynamics of CaSR N-terminal domain.

Structural and spectroscopic studies[57,67,68,73,80,104,105,107-114] suggest a universal activation mechanism for class C GPCRs where ligand binding in the VFT domain results in a conformational rearrangement in the ECDs which propagates over 10 nm to rotate and bring the 7-transmembrane (7TM) domains closer and activate the receptor[80,99,105,107]. Structures of CaSR have shown different conformations with different degrees of rearrangement in various ligand states and generally implies an activation mechanism for CaSR similar to mGluRs[73-75] that consists of 3 conformational states: the inactive open-open (Ioo) conformation characterized by an open VFT and separation between LB2-LB2 and CRD-CRD interfaces; the inactive closed-closed (Icc) conformation characterized by a closed VFT and separation between LB2-LB2 and CRD-CRD interfaces; and the active closed-closed (Acc) conformation characterized by VFT closure and engagement of the LB2-LB2 and CRD-CRD interfaces (Figure 3.1b). However, a direct demonstration of the conformational dynamics underlying CaSR activation and how conformational changes between different domains of CaSR are coupled is lacking.

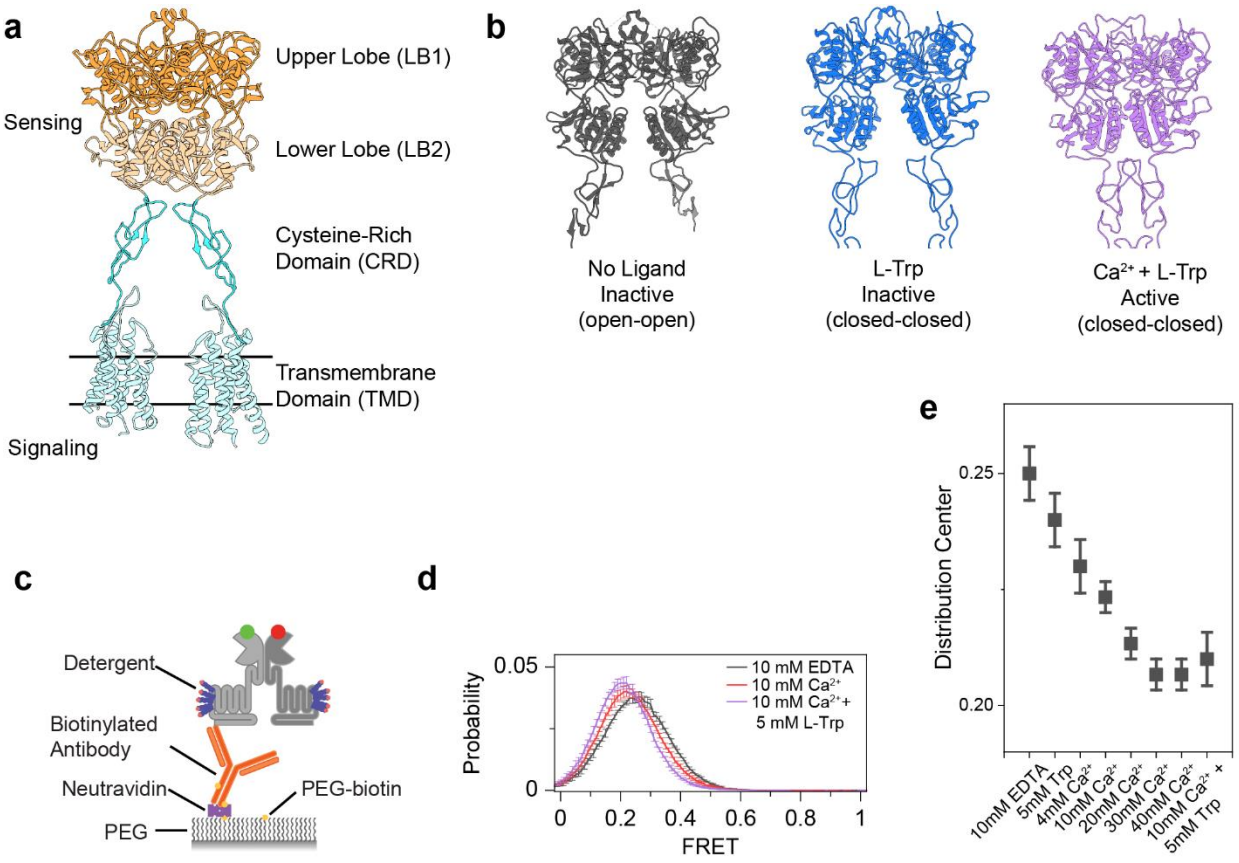

Figure 3.1 – CaSR is an intrinsically dynamic receptor, and ligands stabilize the active conformation.

a Ribbon representation the CaSR structure (PDB ID: 7DTW) colored to highlight the upper lobe (orange), lower lobe (pale orange), cysteine-rich domain (cyan), and the transmembrane domain (pale cyan). **b** Ribbon representation of the CaSR ectodomain in the Ioo, Icc, and Acc conformations (PDB IDs: 5K5T, 7DTU, and 7DTV respectively). **c** Schematic of single-molecule FRET experiments. **d** smFRET population histograms in the presence of 10 mM EDTA, 10 mM Ca^{2+}, or 10 mM Ca^{2+} and 5 mM L-Trp. Data represent mean ± s.e.m. of N=3 independent biological

replicates. **e** Center of a single gaussian distribution fit to FRET histograms. Data represents the mean ± s.e.m. of N=3 fits to independent biological replicates.

We first focused on resolving the ligand-independent and ligand-dependent conformational changes at the N-terminal domain of CaSR. Atomic structures of CaSR in the presence and absence of agonists suggest only a small movement of the N-terminal domain of CaSR upon activation[68,73-75] in contrast to mGluRs[57,67,107]. However, recent results from bulk time-resolved FRET measurements suggest ECD of CaSR undergoes large conformational rearrangement similar in the magnitude to the change in mGluRs[80]. Because receptors undergo rapid and unsynchronized transitions between multiple conformational states, it is inherently challenging to convert bulk FRET measurements to distances and map their activation process and kinetics. To overcome these limitations, we performed single-molecule Förster resonance energy transfer (smFRET) experiments to resolve the ligand-independent and ligand-induced conformational dynamics of CaSR.

First, we performed experiments on a CaSR construct with an N-terminal SNAP-tag for fluorescent labeling and a C-terminal FLAG-tag for surface immobilization (Figure 3.1c). This construct allows direct comparison with similarly tagged mGluR2 construct[57]. Functional experiments using calcium imaging in cells showed that this construct is active with an EC_{50} of 2.84 mM (Figure S3.1a,b), comparable to the wildtype receptor[22,77]. In single-molecule experiments, the FRET distribution showed a single peak centered at FRET=0.25 in the absence of CaSR ligands (and in the presence of 10 mM EDTA) (Figure 3.1d) corresponding to the Ioo conformation. The activating condition (10 mM Ca^{2+} and 5 mM L-Trp) shifts the FRET distribution to 0.21 FRET (~2.5 Å distance change) (Figure 3.1d) corresponding to the Acc

conformation. This FRET change is different from what was observed with a similarly SNAP-tagged mGluR2 that showed a large FRET shift from 0.45 to 0.2 (~12.2 Å) upon activation[57]. Therefore, this result is consistent with the smaller rearrangement of the VFT domains of CaSR observed in atomic structures and supports a unique activation mechanism for CaSR compared to mGluRs. Quantification of receptor dynamics by cross-correlation analysis showed that the receptor is most dynamic in the absence of any ligand compared to conditions with ligands as quantified by cross-correlation amplitude (Figure S3.1c, Supplementary Data 1). This is again in contrast with mGluR2 which was not very dynamic in the apo and fully active states[57]. The observation that CaSR frequently and very briefly visits the 0.21 FRET state at room temperature is consistent with the conformational heterogeneity observed for the ligand-free cryo-EM structures of CaSR[74]. In the presence of agonists, the amplitude of the cross-correlation was reduced (Figure S3.1c) and the FRET distribution narrowed (Figure S3.1d), suggesting that agonists stabilize VFT dynamics. Calcium alone was able to fully shift the FRET distribution to the FRET state corresponding to the Acc conformation (Figure 3.1e). To better visualize receptor dynamics, we acquired data at 5 ms and observed FRET histograms consistent with our 30 ms and 100 ms data (Figure S3.1e,f). At this increased time resolution, single-molecule traces were still very dynamic (Figure S3.1g) and, in the absence of ligand, showed very brief transitions, many within one time point (Figure S3.1g). This again is in contrast with mGluRs that are stable in the inactive state in the absence of ligand and show long-lived visits to the active state in the presence of agonists[57]. Together, these results confirm that in the absence of the ligand, CaSR visits the active state frequently, suggesting a low energy barrier between the active and inactive states in CaSR and in contrast with the mGluRs. However, these brief and unproductive visits do not result

in receptor activation. On the other hand, Ca^{2+} stabilizes the active state conformation to activate the receptor.

Because of the orientation of SNAP-tags in CaSR, the FRET change between the active and inactive FRET states is small (ΔFRET=0.04). This limited our ability to further quantify the kinetic details of the activation process. To overcome this limitation, we designed a new smFRET sensor, based on unnatural amino acid (UAA) 4-azido-l-phenylalanine incorporation[96-99] at the residue 451 (D451UAA hereafter), which expressed at high levels and labeled very efficiently[100,101] (Figure 3.2a). The residue 451 is at the top surface of the LB1 in CaSR with 51.5 Å distance between monomers (Figure 3.2b). This distance put donor and acceptor probes in the sensitive range for FRET and provide higher spatial resolution than the N-terminal SNAP construct. First, we verified that D451UAA showed similar conformational dynamics as the SNAP-tag construct. Both the inactive (10 mM EDTA) and fully active (10 mM Ca^{2+} + 5 mM L-Trp) conditions showed a single FRET distribution peak centered on 0.41 and 0.29 respectively (Figure 3.2c) corresponding to a FRET change of 0.12 or an approximate 4.8 Å change in distance. This is again consistent with our previous result of a small VFT domain conformational rearrangement upon activation and published structures that show 3.6 Å difference between the Ioo and Acc conformations (Figure 3.2b)[74,75]. Like the N-terminal SNAP sensor, addition of ligands reduced the cross-correlation amplitude of D451UAA (Figure 3.2d). Single-molecule traces showed brief visits to the active state (Figure 3.2e). Addition of Ca^{2+} increased the relative occupancy of the active state (Figure 3.2c). Analysis of single-molecule traces using a Hidden Markov model (HMM) also verified that ligand-independent and Ca^{2+}-dependent transitions are between the inactive (FRET=0.41) and active (FRET=0.29) states (Figure 3.2e,f and Figure S3.2a).

Together, these results show that the D451UAA sensor provides a higher sensitivity to conformational change and confirms the results from the SNAP sensor.

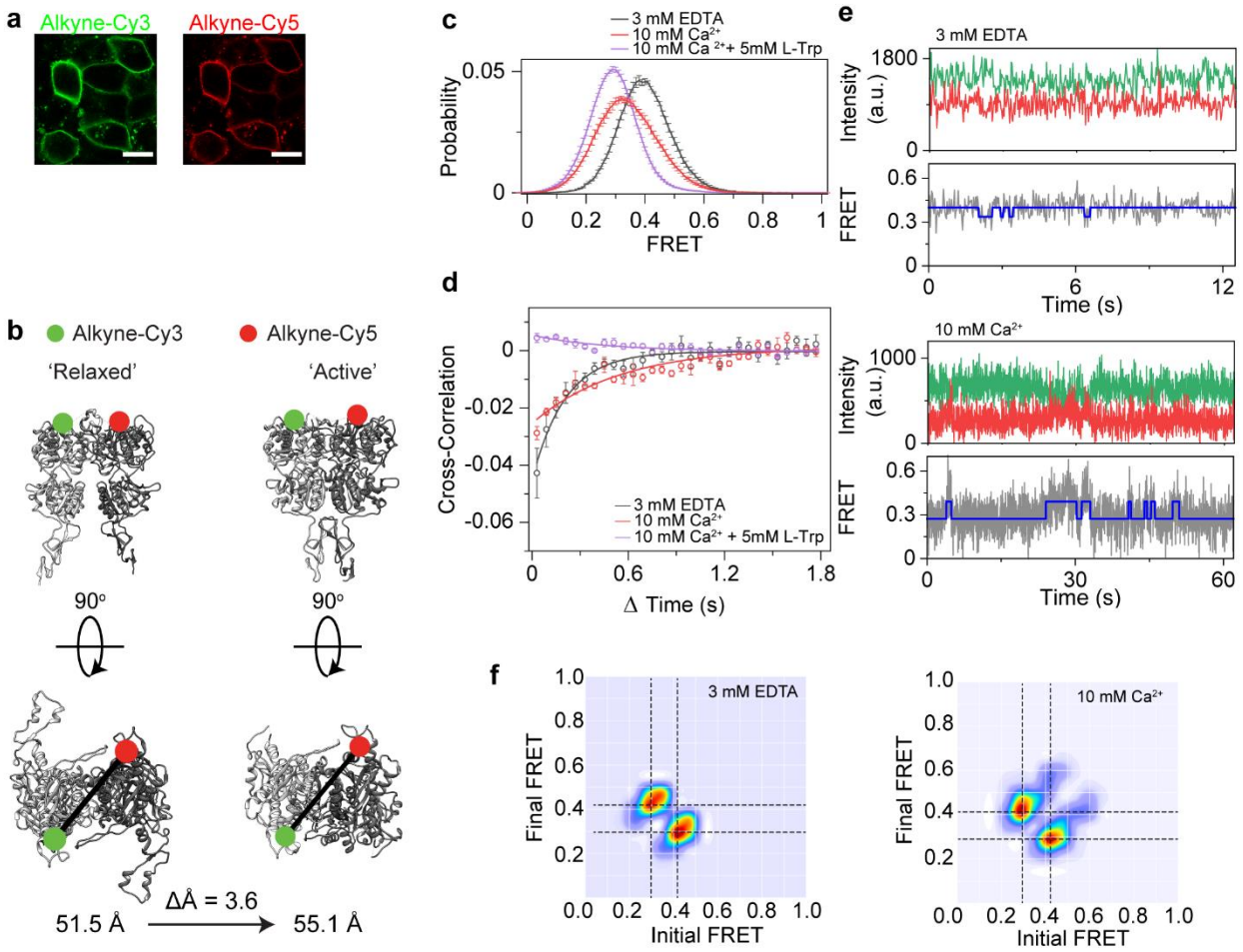

Figure 3.2 – D451UAA CaSR identifies transitions between two conformational states.

a Representative confocal image of HEK293T cells expressing D451UAA and labelled with Alkyne-Cy3 (left) and Alkyne-Cy5 (right). Scale bar, 15 µm. **b** Ribbon representation of crystal structures PDB ID: 5K5T (left) and PDB ID: 7DTV (right) showing approximate location of D451UAA labelling. Measured distance is between D451 Cα represented by black line. **c** smFRET population histogram in the presence of 3 mM EDTA, 10 mM Ca^{2+}, or 10 mM Ca^{2+} and 5 mM L-

Trp. Data represent mean ± s.e.m. of n=3 independent biological replicates. **d** Cross-correlation plots in the presence of 3 mM EDTA, 10 mM Ca^{2+}, or 10 mM Ca^{2+} + 5 mM L-Trp. Data represent ± s.e.m of n=3 independent biological replicates. Data was fit to a single exponential decay function. **E** Sample single molecule traces of D451UAA in 3 mM EDTA (top) and 10 mM Ca^{2+} (bottom) showing donor (green) and acceptor (red) intensities, corresponding FRET values (gray), and idealized FRET trajectory from HMM fit (blue). **f** Transition density plot of D451UAA. Dashed lines represent the most frequently observed transitions and were used for multiple-peak fitting of FRET histograms.

Amino acids facilitate VFT rearrangement beyond VFT closure.

In mGluRs and $GABA_B$Rs, binding of glutamate or GABA within the VFT domain ligand-binding site is sufficient for receptor activation. In CaSR, the canonical class C GPCR ligand binding site is promiscuous and binds different L-amino acids[29]. However, whether L-amino acid binding alone is sufficient or necessary for CaSR activation has been a matter of debate[29,73,74,77,80,115]. Moreover, while evidence suggests L-amino acids act as positive allosteric modulators (PAMs)[116], the dynamic mechanism of this modulatory effect is not well understood. We used the D451UAA sensor to investigate the effect of L-Trp on CaSR structure and dynamics. Published cryoEM structures show a distance change of -0.7 Å measured at the D451 Cα as the receptor transitions from the Ioo conformation to the Icc conformation upon L-Trp binding (Figure 3.3a). This change is below the resolution of smFRET and therefore these two states should appear as a single peak in our smFRET measurement. However, we observed that 2.5 mM L-Trp alone resulted in a smFRET peak centered between the active and inactive FRET states (Figure 3.3b).

This implies that amino acid binding is causing a change in conformation beyond that shown in the Icc structure. The unexpected change in FRET could be caused by the stabilization of a novel conformation or induction of rapid exchange between the 0.29 and 0.41 FRET states due to L-Trp binding. To test this, we performed an L-Trp titration, and we found that by increasing L-Trp concentration the FRET distribution peak moved towards lower FRET values (Figure 3.3b), consistent with L-Trp increasing transitions between the active and inactive states. Inspection of single-molecule traces in the presence of L-Trp alone also showed that CaSR can briefly visit the 0.29 FRET state (Figure 3.3c). HMM analysis also verified that in the presence of L-Trp, CaSR transitions between active and inactive states (FRET= 0.41 and FRET=0.29) (Figure 3.3d). However, like the unliganded receptor, the transitions are brief and do not substantially increase the active state occupancy and likely cannot result in signaling[74,77,80]. Therefore, these results are consistent with a model that amino acids not only induce closure of the VFT as observed in structures, but also increase the occupancy of the 0.29 FRET state suggesting transient rearrangement in the dimeric interface.

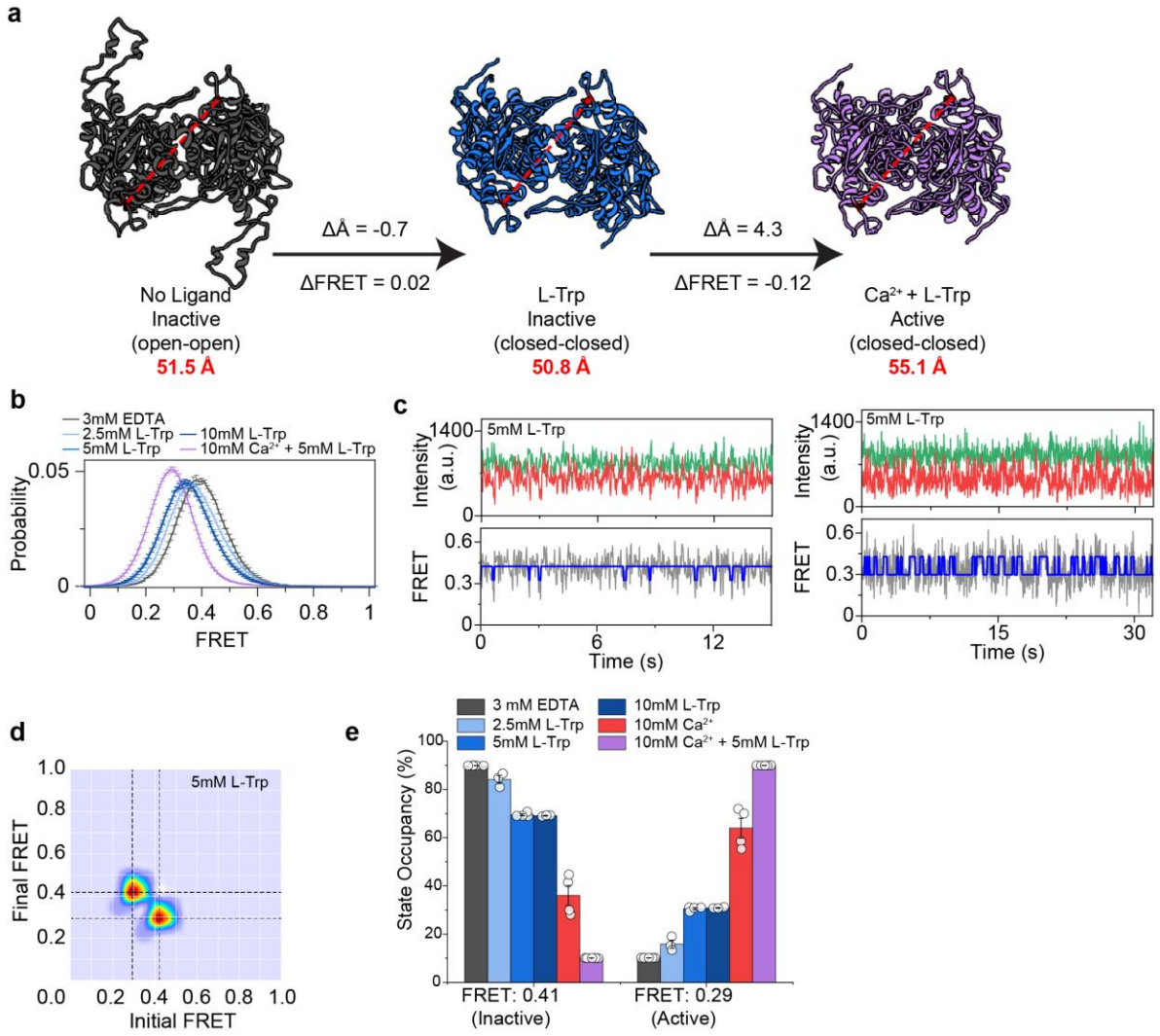

Figure 3.3 – L-Trp increases occupancy of the active state but is insufficient for activation.

a Top-down view of CaSR structures showing the distance between the Cα of D451 (red) for the Ioo, Icc, and Acc conformations (PDB IDs: 5K5T, 7DTU, and 7DTV respectively). Arrows show change in distance of the D451 Cα and the corresponding predicted change in FRET. **b** smFRET population histogram in the presence of 3 mM EDTA, 2.5 mM L-Trp, 5 mM L-Trp, 10 mM L-Trp, or 10 mM Ca^{2+} and 5 mM L-Trp. Histograms for 5 mM L-Trp and 10 mM L-Trp overlap. Data represent mean ± s.e.m. of n=3 individual independent biological replicates. **c** Sample single

molecule traces of D451UAA in 5 mM L-Trp showing donor (green) and acceptor (red) intensities, corresponding FRET (gray), and idealized FRET trajectory from HMM fit (blue). Sample traces show particles exhibiting different behaviors in the same condition with infrequent and very brief transitions (1-2 datapoints), or frequent and brief transitions (5-10 data points). **d** Transition density plot of D451UAA. Dashed lines represent the most frequently observed transitions and were used for multiple-peak fitting of FRET histograms. **e** Occupancy of the two FRET states of the VFT in the presence of increasing ligand concentrations. Values represent mean ± s.e.m. area under individual FRET peaks from n=3, 4, or 5 independent biological replicates.

To investigate the cooperative function of L-Trp with Ca^{2+}, we quantified the occupancy of each FRET state in different ligand concentrations (Figure 3.3e and Figure S3.2b). We found that while 10 mM Ca^{2+} alone significantly increases the occupancy of the active state, addition of 5 mM L-Trp fully shifts the occupancy of the active state. Importantly, higher concentrations of Ca^{2+} alone can fully shift the histogram to the lower FRET peak (Figure 3.1e). To ensure that our observation is not due to residual L-Trp bound to CaSR during the purification[64,68,73,74], we performed an extended wash of immobilized receptor and did not detect any change in the FRET distribution post-wash while the distribution again shifted to lower FRET in the presence of Ca^{2+} alone (Figure S3.2c). Furthermore, we collected smFRET data before, during, and after addition of 5 mM L-Trp. We found that 5 mM L-Trp reversibly shifted the FRET histogram (Figure S3.2d) suggesting we can remove amino acids bound to immobilized receptors. Based on these data, it is unlikely that the effect observed in the presence Ca^{2+} alone to be caused by residual amino acid

binding. Together, these observations are consistent with the role of amino acids as allosteric modulators[74,80].

Calcium is essential for the formation of the CRD-CRD interface

Next, we probed the propagation of conformational changes beyond the VFT. According to the canonical class C GPCR activation model, the extracellular domain controls the proximity and the relative orientation of the 7TM domains, and in the active state, the 7TM domains come into direct contact[74,75,99,107,110]. We used another UAA-based FRET sensor at amino acid 593 (E593UAA) to probe the conformation of the CRD of CaSR as it showed the highest labeling efficiency of CRD sensors tested (Figure S3.3a) and had an activity comparable to wild-type (Figure S3.3b). Since the CRD is closer to the 7-TM domain we expected that this sensor to be a more accurate reporter of receptor activation than the VFT domain sensor. SmFRET analysis showed that the CRD of CaSR is in dynamic equilibrium between at least 4 conformational states (Figure 3.4a,b), similar to mGluR2[99], and Ca^{2+} increases the occupancy of the higher FRET states consistent with the compaction of the receptor upon activation (Figure 3.4c and Figure S3.3c). Importantly, we found that L-Trp alone slightly increases the occupancy of the intermediate FRET states, but it does not increase the occupancy of the highest FRET state that corresponds to the Acc conformation (Figure 3.4c,d). This further confirms that L-Trp alone cannot stabilize the active conformation sufficiently to result in the receptor activation, as probed at the CRD. Importantly, the PAM effect of L-Trp is due to increasing the occupancy of intermediate transition states.

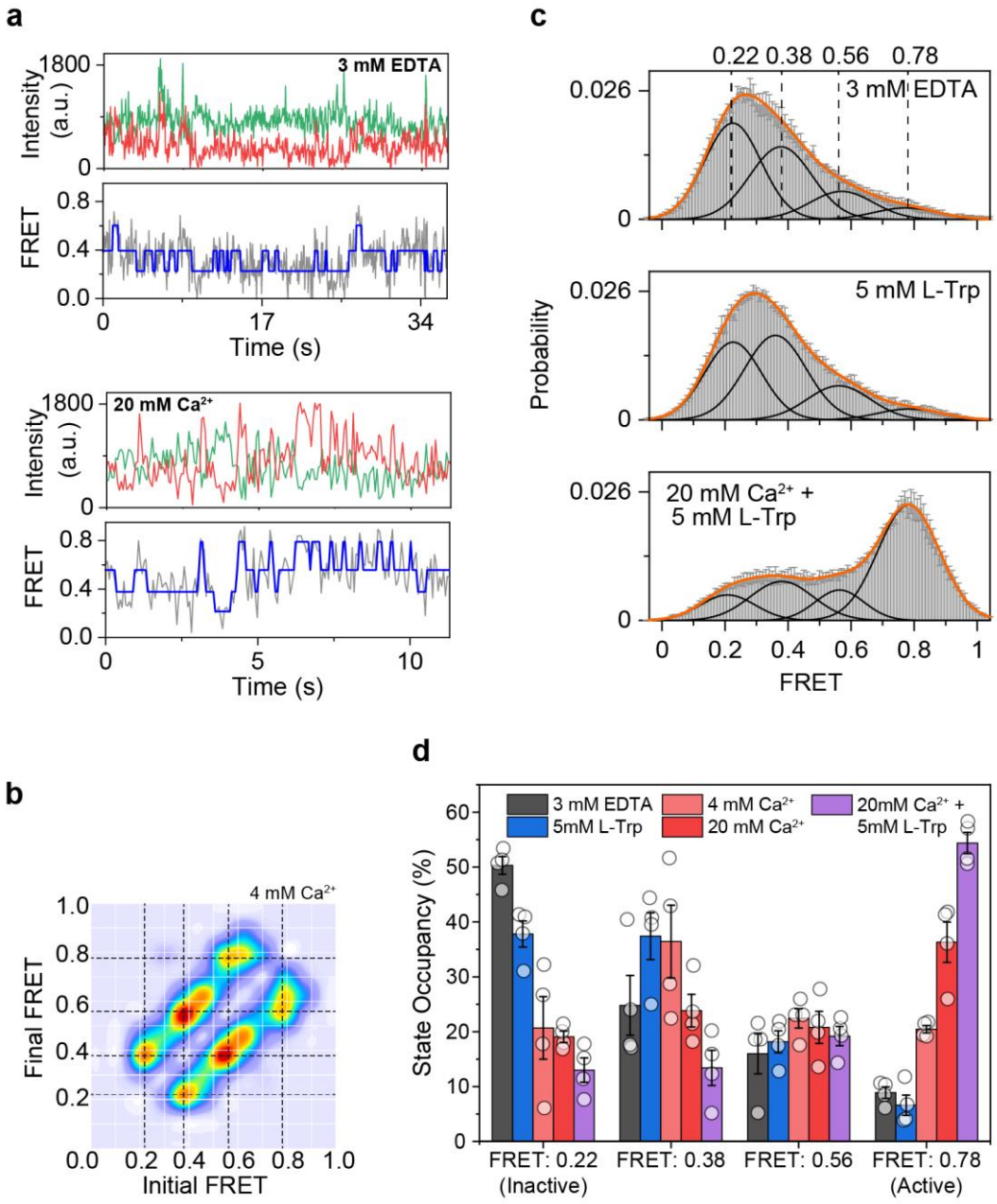

Figure 3.4 – CRD of CaSR is in equilibrium between four conformational states.

a Sample single molecule traces of E593UAA in 3 mM EDTA or 20 mM Ca^{2+} showing donor (green) and acceptor (red) intensities, corresponding FRET (gray), and idealized FRET trajectory from HMM fit (blue). **b** Transition density plot of E593UAA. Dashed lines represent the most

frequently observed transitions and were used for multiple-peak fitting of FRET histograms. **c** smFRET population histogram in the presence of 3 mM EDTA, 5 mM L-Trp, or 20 mM Ca^{2+} and 5 mM L-Trp. Data represent mean ± s.e.m. of n=4 independent biological replicates. Histograms were fit with four single gaussian distributions (black) centered at 0.22, 0.38, 0.56, 0.78, and the cumulative fit is overlaid (orange). **d** Occupancy of the four FRET states of the CRD in the presence of increasing ligand concentrations. Values represent mean ± s.e.m. area under individual FRET peaks from n=4 independent biological replicates.

An interprotomer loop reduces the role of amino acids in activation

To explore the molecular reasons for the unique outcome of amino acid binding in CaSR compared to mGluRs, we mapped the interaction area of the dimer interface of CaSR between active and inactive conformations (Figure 3.5a). A continuous strip of interactions along the LB1 interface of CaSR is maintained in both the active and inactive conformations (Figure 3.5a, left). This is in contrast with mGluR1, evolutionary the closest mGluR to CaSR, which shows a smaller and less distributed interaction area in LB1 (Figure 3.5a, right). We hypothesized that this difference in the distribution of intermolecular interactions at LB1 could be partly responsible for the distinct outcome of amino acid binding in CaSR compared to mGluRs. To investigate the structural elements underlying this, we compared the sequence of LB1 in CaSR and mGluRs (Figure 3.5b). We detected a conserved structured loop which is significantly elongated in CaSR compared to mGluRs (Figure 3.5c). In CaSR, this loop was observed in crystal structures and was suggested to be involved in receptor dimerization[68]. This loop extends from one protomer and

makes extensive contacts with and docks into the adjacent promoter through a highly conserved sequence (Figure S3.4a). Specifically, the highly conserved residue P55 makes contacts with Y161 and W458 in the adjacent promoter (Figure S3.4b). Multiple disease-associated mutations localize to this interprotomer loop including the P55L mutation[117,118]. We hypothesized that this loop, by restricting the movement of protomers through increased LB1 dimer interactions, could be part of the reason for smaller conformational rearrangement of CaSR compared to mGluR2 (Figure 3.1). Interestingly, the loop is disordered in a recent structure of a nanobody stabilized inactive CaSR that positioned the VFT domain in an mGluR-like inactive conformation[75]. To test this, we performed smFRET experiment on a D451UAA construct with P55L mutation in the presence of different ligand conditions. First, in the absence of ligands, we observed the same 0.41 inactive peak as wildtype CaSR (Figure 3.5d). Next, we detected a similar active peak as wildtype (Figure 3.5d) but at a much higher calcium concentration (40 mM Ca^{2+} + 5 mM L-Trp) consistent with the physiological loss-of-function phenotype for his mutant. Surprisingly, in the presence of 5 mM L-Trp alone the FRET distribution shifted to a new stable state centered at FRET=0.5 (Figure 3.5d, blue). The occupancy of this new FRET state decreased by adding increasing concentrations of Ca^{2+}. This suggests the loop controls the conformational space of L-Trp bound CaSR. Functional characterization showed that L-Trp still functions as a PAM for the P55L mutant (Figure S3.4c). To further investigate the role of this loop in amino acid modulation of Ca^{2+} potency, we truncated the loop to be more mGluR-like (Δ47-57) and quantified the effect of 10 mM L-Trp on Ca^{2+} potency for the new mutant. We observed a 40%, 45%, and 58% reduction of Ca^{2+} EC_{50} for wild-type, P55L, and Δ47-57 respectively (Figure S3.4c). The larger reduction of EC_{50} is indicative of amino acids becoming a more critical ligand for receptor activation when interprotomer loop

contacts are disrupted. Together, these results are consistent with the interpretation that this extended loop shapes the energy landscape of CaSR by restricting the movement of the LB1 and reduce the overall contribution of amino acid binding to receptor conformational rearrangement and activation.

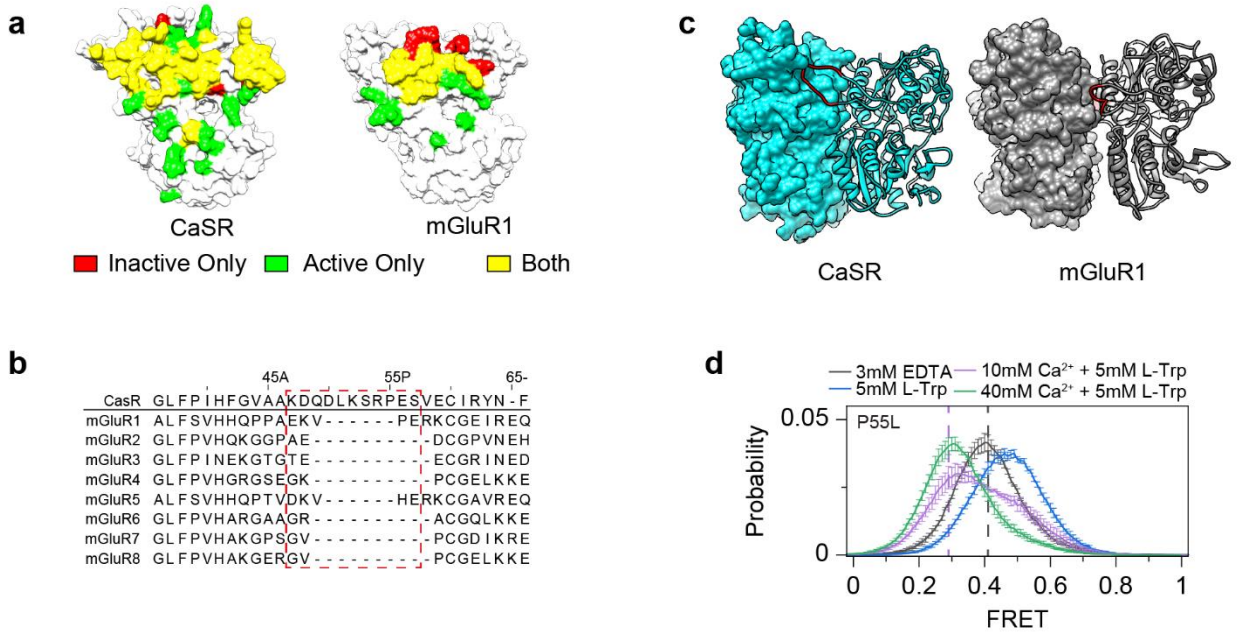

Figure 3.5 – An elongated interprotomer is critical for VFT coordination.

a Surface representation of CaSR (left, PDB 5K5S) and mGluR1 (right, PDB 1ISR) showing contacts made between monomers in the inactive structure only (red), active structure only (green), or both (yellow). **b** Multiple sequence alignment of human CaSR and mGluRs. CaSR is used as reference for residue numbering. Sequence of interprotomer loop indicated by red dashed line. **c** Surface and ribbon representation of CaSR (left, PDB 5K5S), and mGluR1 (right, PDB 1ISR) with interprotomer loop colored red. **d** smFRET population histogram for P55L in the presence of 3 mM EDTA, 5 mM L-Trp, 10 mM Ca^{2+} and 5 mM L-Trp, or 40mM Ca^{2+} and 5 mM L-Trp. For

reference, dashed lines indicate centers of wild-type distributions for EDTA (grey) and 10 mM Ca^{2+} + 5 mM L-Trp (purple). Data represent mean ± s.e.m. of n=3 independent biological replicates.

DISCUSSION

Our findings revealed the design of CaSR activation, which has evolved to measure concentration of extracellular Ca^{2+}. Despite very high overall structural similarities between CaSR and mGluRs (1.7 Å RMSD), these receptors evolved to sense signals with very different temporal profiles. In the case of mGluRs, synaptic glutamate is a signal that varies stepwise between very low to very high levels and over a fast timescale while CaSR must measure slow changes in extracellular Ca^{2+} that varies around ~2.4 mM over hours timescale. Signals preexist their receptor. Therefore, evolution of new receptors requires modification of the ancestral receptor to not only sense the chemical identity of the new signal, but also to adapt to its temporal structure in native context. Thus, a signal that changes over milliseconds timescale imposes different evolutionary mechanical constraints on the receptor than a signal that changes over hours timescale.

We found that several unique structural features of CaSR, compared to mGluRs, can partially account for the distinct activation mechanism of CaSR. First, an elongated intermolecular loop previously visualized in crystal structures and involved in linking the LB1s of CaSR[68] and second, an increased contact area for the LB1 interface. These features likely restrict movement of the ECD in CaSR and holds the LBDs closer, resulting in a unique activation mechanism. Our

results suggest that the energy barrier between the active and inactive states is lower in CaSR than in mGluR2 (Figure 4.2d) which enables CaSR to visit and sample the active state often and briefly, even in the absence of any ligand.

Binding of amino acids has been shown in structure models to induce closure of the VFT domain but not engagement of the LB2 interface that resemble the active conformation. Our results suggest that amino acids also induce conformational changes in the VFT that may include temporary or partial engagement of the LB2 interface. We observed the ability of L-Trp to induce an increase in occupancy of the 0.29 FRET active state for D451UAA, but we did not observe a similar increase in the occupancy of the 0.78 FRET active state for E593UAA which probes the CRD. This is possibly due to the loose coupling between these domains, as was also observed in mGluR2[99]. Because of this, we are not able to conclude that amino acid binding alone induces the Acc conformation characterized by engagement of both the LB2-LB2 interface and the CRD-CRD interface (Figure 3.6). Finally, it is possible additional intermediate states exist that we did not resolve due to the spatial and temporal limitations of smFRET measurements.

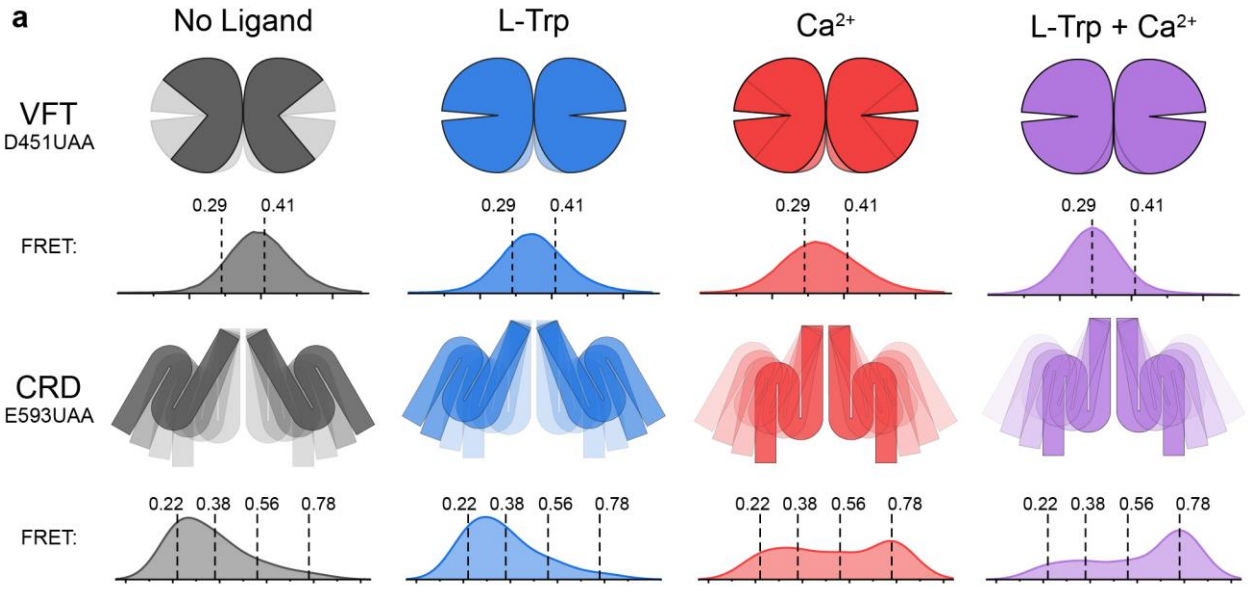

Figure 3.6 – Functional characterization smFRET histograms of CaSR mutants.

A Model schematic of CaSR showing the effect of ligands on the VFT and CRD domains and corresponding FRET distributions.

MATERIALS & METHODS

Molecular cloning

Same as previously described in Chapter 2.

Mutations of D451UAA CaSR (P55L and Δ47-57) were introduced using a QuikChange site-directed mutagenesis kit (Qiagen).

Cell culture conditions

Same as previously described in Chapter 2.

Transfection and protein expression

Same as previously described in Chapter 2.

SNAP-tag labeling in live cells

Same as previously described in Chapter 2.

Unnatural amino acid labeling in live cells by azide-alkyne click chemistry

Same as previously described in Chapter 2.

Single-molecule FRET measurements

Single-molecule FRET experiments were performed using flow cells prepared with glass coverslips (VWR) and slides (ThermoFisher Scientific) passivated with mPEG (Laysan Bio) and 1% (w/w) biotin-PEG to prevent nonspecific protein adsorption as previously described[57,119]. Before experiments, flow cells were prepared by first incubating with 500 nM NeutrAvidin (ThermoFisher Scientific) for 5 min followed by either 20 μM biotinylated FLAG antibody (A01429, GenScript) or 20 μM biotinylated GFP antibody (ab6658, Abcam) for 30 min. Washing removed unbound NeutrAvidin and biotinylated antibody. Washes and protein dilutions were done with T50 buffer (50 mM NaCl, 10 mM Tris, pH 7.4).

Post labeling, cells were recovered from 1 to 3 18-mm polylysine-coated glass coverslips (VWR) by incubating with DPBS (Ca^{2+}-free, Gibco) followed by gentle pipetting. After resuspension, cells were briefly kept on ice and then pelleted by centrifugation at 4,000*g* at 4 °C for 10 min. The cell pellet was lysed in 100 to 300 μl (depending on the number of coverslips transfected) of a lysis buffer consisting of 10 mM Tris, 150 mM NaCl, protease inhibitor tablet with EDTA (ThermoFisher Scientific) and 1.2% IGEPAL (Sigma), pH 7.4. After 1 h of gentle

mixing at 4 °C, lysate was centrifuged at 20,000*g* at 4 °C for 20 min. The supernatant was collected and diluted (two- to tenfold dilution depending on the concentration) and was then added to the flow chamber to achieve sparse surface immobilization of labeled receptors via their C-terminal tag (mEGFP or FLAG). Sample dilution and washes were done using a dilution buffer consisting of 10 mM Tris, 150 mM NaCl, and 0.05% IGEPAL (Sigma), pH 7.4. The flow chamber was washed extensively with dilution buffer to remove unbound proteins (>20× chamber volume) after optimal receptor density was achieved. Finally, labeled receptors were imaged in imaging buffer consisting of 4 mM Trolox, 128 mM NaCl, 2 mM KCl, 40 mM HEPES, 0.05% IGEPAL and an oxygen-scavenging system consisting of 4 mM protocatechuic acid (Sigma) and 1.6 U/mL bacterial protocatechuate 3,4-dioxygenase (rPCO) (Oriental Yeast), pH 7.35. All chemicals were purchased from Sigma or Millipore. All buffers were made using ultrapure distilled water (Invitrogen) or ultrapure filtered water (Milli-Q).

For the extended wash, a dataset was acquired prior to passing 50x chamber volume of wash buffer through the flow chamber every 30 minutes for 2 hours. After the fifth wash at 2 hours, a dataset was acquired to compare to the pre-wash data. Finally, a dataset was acquired in the presence of 10 mM Ca^{2+}. Samples were imaged with a 100× objective (Olympus, 1.49 numerical aperture, oil-immersion) on a TIRF microscope in the oblique illumination mode and using an excitation filter set with a quad-edge dichroic mirror (Di03-R405/488/532/635, Semrock) and a long-pass filter (ET542lp, Chroma), with 30 ms time resolution unless stated otherwise. Lasers at 532 nm and 638 nm (RPMC Lasers) were used for donor and acceptor excitation, respectively.

smFRET data analysis

Analysis of single-molecule fluorescence data was performed using smCamera (http://ha.med.jhmi.edu/resources/), custom MATLAB (MathWorks) scripts, custom Python scripts, and OriginPro (OriginLab). The selection of particles and generation of raw FRET traces was done automatically within the smCamera software. Only particles that showed acceptor signal upon donor excitation, acceptor brightness greater than 10% above background, and a Gaussian intensity profile were automatically selected (Figure SA1.1b). Donor and acceptor intensities were measured over all frames for the selected particles. Only particles that showed a single donor and a single acceptor bleaching step during the acquisition time (Figure SA1.1c), stable total intensity ($I_D + I_A$), anticorrelated donor and acceptor intensity behavior without blinking events and that lasted for more than 3 s were manually selected for further analysis (~10%–15% of total molecules per movie). Two individuals independently analyzed subsets of the data and the results were compared and shown to be identical. Furthermore, a subset of data was analyzed blind to ensure no bias in the analysis. Apparent FRET efficiency was calculated as $(I_A - 0.085 \times I_D)/(I_D + I_A)$, where I_D and I_A are raw donor and acceptor intensities, respectively. Every experiment was repeated in triplicate to ensure reproducibility of the results unless otherwise noted. A minimum of 300 FRET traces from 3 independent biological replicates were used to generate population smFRET histograms unless otherwise stated. Before trace compilation, FRET histograms of individual particles were normalized to 1 to ensure that each trace contributed equally, regardless of trace length. Error bars on histograms represent the standard error three independent biological replicates.

Peak fitting of smFRET histograms was performed using OriginPro with either 1, 2 or 4 Gaussian distributions as,

$$y(x) = \sum_{i=1}^{n} \frac{A_i}{w_i\sqrt{\frac{\pi}{2}}} e^{-2\cdot\frac{(x-xc_i)^2}{w_i^2}}$$

where n is the number of Gaussians, A is the peak area, *xc* is the FRET peak center and *w* is the full width half maximum for each peak. Peak centers (*xc*) were constrained as mean FRET efficiency of a conformational state ±0.02. The mean FRET efficiencies associated with different conformational states was determined based on the most frequent transitions between FRET efficiencies in transition density plots, which are denoted by dashed lines (Figures 3.2f, 3.3d, 3.4b). Peak fitting used the LevenBerg-Marquardt algorithm to determine the best fit by Chi-square with a tolerance of 1E-9 in OriginPro. This analysis is further described below. Peak widths were constrained as $0.1 \le w \le 0.24$. Peak areas were constrained as $A > 0.001$. Probability of state occupancy was calculated as area of specified peaks relative to the total area, which is defined as the cumulative area of all individual peaks.

Raw donor, acceptor, and FRET traces were idealized by fitting with a hidden Markov model (HMM) using ebFRET software[120]. Traces for which a single state was assigned were omitted from downstream analysis. Transition density plots were then generated by extracting all the transitions where $\Delta\text{FRET} > 0.1$ from the idealized traces.

The cross-correlation (CC) of donor and acceptor intensity traces at time τ is defined as $\text{CC}(\tau) = \delta I_D(t)\delta I_A(t+\tau)/(\langle I_D\rangle + \langle I_A\rangle)$, where $\delta I_D(t) = I_D(t) - \langle I_D\rangle$, and $\delta I_A(t) = I_A(t) - \langle I_A\rangle$. $\langle I_D\rangle$ and $\langle I_A\rangle$ are time average donor and acceptor intensities, respectively. Cross-correlation

calculations were performed on the same traces used to generate the histograms. Cross-correlation data were fit with a single exponential decay function $y(x) = y_0 + A \cdot e^{-\frac{x}{t}}$ by OriginPro (OriginLab).

Analysis of multiple sequence alignments

CaSR and mGluR sequences were pulled from ensembl[121] (version 103) and a multiple sequence alignment was generated using MUSCLE[122] and default parameters.

Structural analyses

Distances were measured in Chimera[123]. Based on the spectral overlap of Cy3 alkyne and Cy5 alkyne, a Förster radius (R_0) of 54 Å was used to convert raw FRET efficiency f to an approximate distance using FRET = $1/(1 + (R/R_0)^6)$.

Identification of interprotomer contacts was performed in Chimera. Inactive and active structures of CaSR and mGluR1 (PDB: 5K5T, 5K5S, 1EWT, 1ISR) were prepared prior to analysis using the Dock Prep tool. Residues involved in interprotomer contacts were identified using the FindContacts tool with a VDW Overlap threshold of -1Å and 0Å for hydrogen bonding pairs.

RMSD between CaSR and mGluR was calculated by superimposing the two structures (PDB: 7DTV, 6N51) using DeepView (SwissPDB Viewer)[124] using an iterative magic fit, which gave an RMSD of 1.7 Å over 2164 backbone atoms for only those parts where the structures overlayed well for the full-length monomer, and an RMSD of 1.8 Å over 3696 backbone atoms for the full-length dimer.

CHAPTER 4: EVOLUTIONARY MECHANISM OF TUNING CA^{2+}-SENSITIVITY OF THE CASR

INTRODUCTION

In all vertebrates from fish to humans, CaSR functions as the molecular sensor for the extracellular calcium concentration[22,125,126]. In this context, CaSR provides corrective feedback to keep serum calcium levels within a very narrow controlled range (2.2-2.6 mM in human)[4] by reducing blood plasma concentration through attenuation of PTH secretion from the parathyroid. However, the EC_{50} of CaSR varies widely between different animals, likely to match the Ca^{2+} homeostatic requirement and environmental niche of each organism. For example, published EC_{50} values range from 1 mM in goldfish to 7.5 mM in dogfish shark[54,127]. Because the set points of CaSR from different organisms varied, there must exist a means to finely tune the sensitivity of CaSR to Ca^{2+}, but how this is accomplished is unclear.

We hypothesized that the variable regions of the dimer interface could serve as a platform for sensitivity tuning by regulating the stability of the dimer interface. To determine if this is true, I analyzed the sequences of the 200 CaSR orthologs available in the Ensembl[121] database. In this work, I show an electrostatic surface is evolutionarily largely conserved across the 200 sequences available and variability in the conservation of charged residues (Asp, Glu, Lys, and Arg) can explain the observed variability of sensitivities (EC_{50}) of CaSR orthologs. Specifically, two disease-associated and 3 previously uncharacterized mutations all increase the Ca^{2+} sensitivity of

CaSR suggesting this surface could serve as an evolutionary platform for the fine-tuning of the set point of CaSR to fit the specific requirements of the organism.

RESULTS

Negative charge density of the dimer interface is a key regulator of CaSR activation.

To further investigate the structural determinants of the CaSR and mGluR adaptation for their physiological ligands we performed a multiple sequence alignment of CaSR, the mGluRs, and the taste receptors (Tas1Rs) (Figure S4.1a). We observed a significantly higher number of negatively charged residues on the lower lobe interface (LB2) in CaSR compared to other class C GPCRs (Figure S4.1a). This was previously highlighted in crystal structures and was suggested to be important for ion binding[68]. We quantified the electrostatic potential of CaSR and all other class C GPCRs with published structures (Figure 4.1a and Figure S4.1b) and found that the LB2 of the CaSR VFT domain is significantly more electronegative compared to all other class C GPCRs[74,80] (Figure 4.1a and Figure S4.1b).

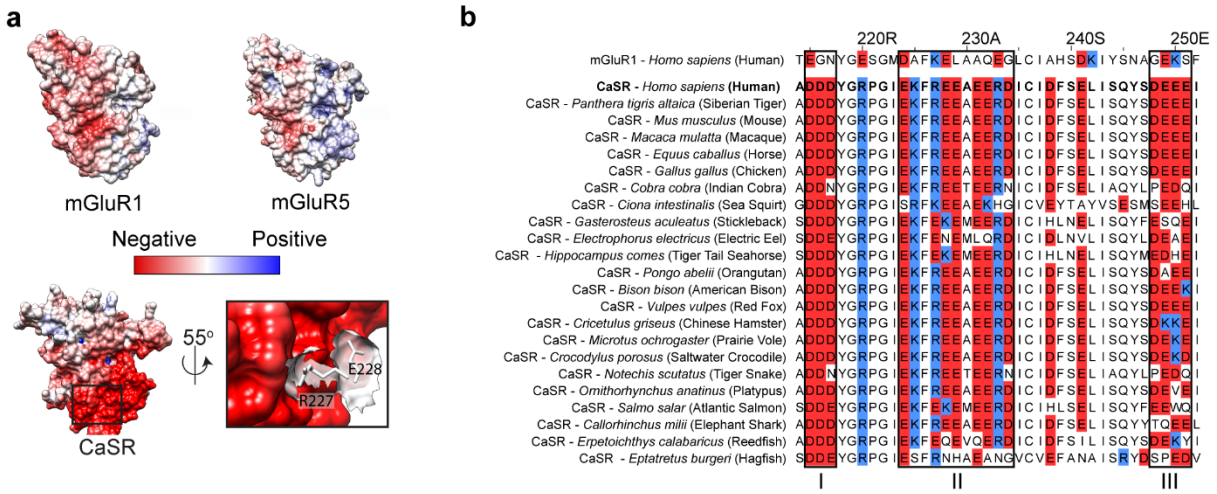

Figure 4.1 – The highly negative charge of the CaSR dimer interface is variable.

a Electrostatic potential map of mGluR1 (top left, PDB 1ISR), mGluR5 (top right, PDB 3LMK), and CaSR (bottom left, PDB 5K5S). Close up inset of CaSR (bottom right) showing stick and surface representation of R227 and E228 at the lower lobe interface. **b** Multiple sequence alignment of mGluR1, CaSR, and select CaSR orthologs with negatively charged residues (red) and positively charged residues (blue) highlighted. CaSR is used as reference for residue numbering. Boxes indicate regions of high charge density unique to CaSR.

To identify the functionally significant amino acids within this interface, we aligned CaSR and 200 orthologs (Figure 4.1b). This analysis revealed that the negative surface charges on the LB2 of CaSR are very conserved across different organisms (Figure 4.1b) emphasizing the universal functional role of this design. Notably, these surface charges occur in three distinct

patches within a structurally conserved helix-sheet-helix motif that, in human, includes a DDD motif (I), a EKFREEAERD motif (II), and a DEEE motif (III) (Figure 4.1b). Importantly, this topology is absent in other class C GPCRs (Figure S4.1a). Furthermore, many disease-associated mutations in CaSR such as D215G[128], R220W[129], R227L[117], R227Q[128], and E228K[130] localize to these structural elements highlighting their importance in CaSR function. Because the LB2 surface of the monomers come into proximity in the active state of (Figure 3.5a), the negative charge density of the intermolecular interface of LB2 modulates the stability of the active state via electrostatic repulsion.

To test this, we performed smFRET experiments on mutants that alter this surface charge density. Specifically, we tested R227L and E228K mutants within the EKFREEAERD segment which increase and decrease the surface negative charge, respectively. Both are disease-associated mutations in humans that result in loss-of-function (for R227L) or gain-of-function (for E228K) in CaSR and cause hyperparathyroidism and hypocalcemia respectively[117,130]. In smFRET experiments, both variants showed the same canonical FRET states as wildtype (Figure 4.1c), suggesting that the mutations do not alter the overall coordination of protomers within the dimer. However, we found that in the presence of 10 mM Ca^{2+}, E228K had substantially higher occupancy of the active state while R227L had lower occupancy of the active state, compared to the wildtype CaSR (Figure 4.1d). This observation is consistent with the gain-of-function and loss-of-function phenotypes for these mutants and our assignment of the active and inactive FRET conformations. Importantly, these residues are not part of known Ca^{2+} binding sites[68,73-75] (Figure S4.1d) and therefore this observed effect on receptor sensitivity is allosteric. Interestingly, the effect of these mutations on the occupancy of active state relative to wild-type CaSR is the same for L-Trp only

or Ca^{2+} only (Figure 4.1d), suggesting that binding of both ligands likely converge on the same downstream conformational pathway. The fact that increasing the negative charge of LB2 impedes and decreasing the negative charge facilitates activation of CaSR supports our interpretation that the very high negative charge density of LB2 in CaSR has evolved to control activation via electrostatic repulsion. This arrangement also limits spontaneous activation of CaSR via limiting the occupancy of active state in the ligand free receptor. This also could explain why spontaneous visits to the active state in the ligand free condition cannot result in receptor activation.

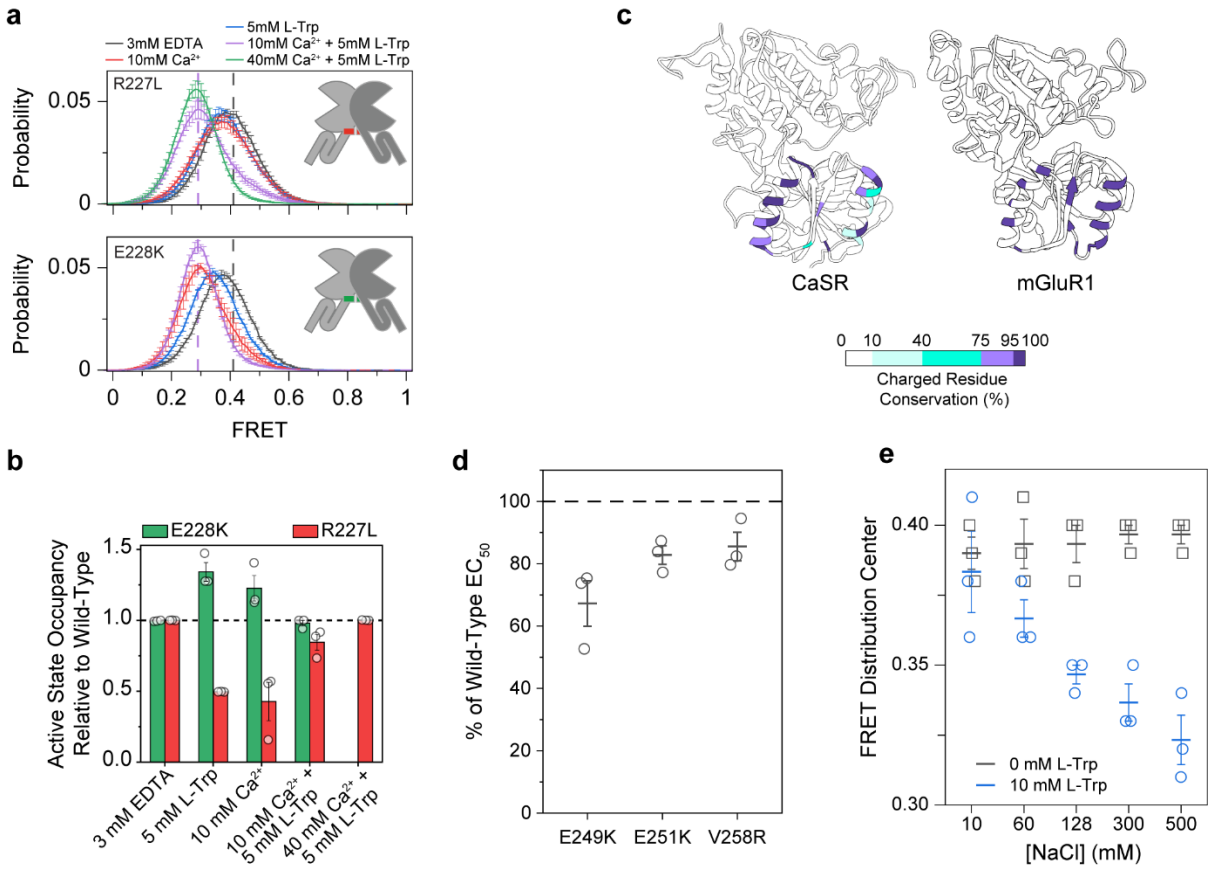

Figure 4.2 – Relative charge distribution of an electrostatic interface tunes calcium sensitivity of CaSR.

a smFRET population histograms of R227L and E228K in the presence of 3 mM EDTA, 5 mM L-Trp, 10 mM Ca^{2+}, 10 mM Ca^{2+} and 5 mM L-Trp, or 40mM Ca^{2+} and 5 mM L-Trp. For reference, dashed lines indicate centers of wild-type distributions for EDTA (grey) and 10 mM Ca^{2+} + 5 mM L-Trp (purple). Data represent mean ± s.e.m. of n=3 independent biological replicates. **b** Occupancy of the active FRET state of R227L and E228K for each condition normalized to wild-type. Values represent mean ± s.e.m. area under active FRET peaks from smFRET population histograms, averaged over 3 independent biological replicates, centered at 0.41 (inactive) and 0.29 (active). 40 mM Ca^{2+} + 5 mM L-Trp condition was not tested for E228K **c** Ribbon representation of CaSR (left) and mGluR1 (right) (PDB IDs: 5K5S & 1ISR) displaying the conservation of charged residues at each position in LB2 across 200 species. **D** EC_{50} for E249K, E251K, V258R CaSR as a percentage of wild-type. Data represents the mean ± s.e.m. of n=3 independent biological replicates. **e** Center of a single gaussian distribution fit to FRET histograms. Data represents the mean ± s.e.m. of n=3 fits to independent biological replicates.

To explore the possible evolutionary role of the above design we quantified the degree of variation in the charge distribution on LB2 in CaSR and mGluR1 in different organisms. We selected the location of charged residues in the LB2 interface of CaSR and mGluR1 from 200 organisms and mapped their conservation onto the canonical structure of human CaSR and mGluR1 (Figure 4.1e). Our analysis showed that the LB2 of CaSR is significantly more permissive

to the gain and loss of charged residues at each position than mGluR1. In other words, throughout evolution the location of charges is more mobile in CaSR compared to mGluR1 (Figure 4.1e and Figure S4.2a). As a comparison, this level of variability does not exist in LB1 of CaSR or mGluR1 (Figure S4.2b). We experimentally verified the ability of interface charge to modulate sensitivity with previously uncharacterized mutations E249K, E251K, and V258R, which are in the most variable region of LB2 (Figure S4.1d) and are not near any implicated ion binding sites from structures. All mutations reduce the negative surface charge density and showed increased calcium sensitivity compared to wild-type CaSR (Figure 4.2d). Finally, we performed smFRET experiments on WT CaSR and in the presence of increasing concentration of NaCl. We found that FRET distribution shifted further to the left in the presence of 5 mM L-Trp only when the concentration of NaCl increased (Figure 4.1g and Figure S4.1e) further suggesting the role of electrostatic repulsion in regulating occupancy of the 0.29 FRET state. The ability of NaCl to modulate the effect of L-Trp and in the absence of Ca^{2+} is consistent with our interpretation that amino acid binding induces a partial or transient engagement of the LB2-LB2 interface. Moreover, it suggests that the regulatory effect of the negatively charged LB2 patch is independent of Ca^{2+}. These data and the large variability of charge distribution on LB2 of CaSR among different organisms and the fact that the negative charge on the LB2 is a key controller of receptor activation raises the possibility that this electrostatic interface may have evolved as a mechanism for tuning the receptor sensitivity and the setpoint of CaSR activation, to match the needs of different organisms.

DISCUSSION

In Chapter 3, we showed that the VFT of CaSR visits the active FRET state. However, the large focused negative electrostatic surface charge of LB2 in CaSR impedes activation via electrostatic repulsion of the LB2 domains, which must come in proximity for receptor activation (Figure 4.2e). This likely prevents spontaneous activation of CaSR in the absence of ligand or by L-amino acids alone.

Receptor dimerization is a powerful design principle for initiating signal transduction. In this paradigm, ligand binding to monomeric receptors triggers dimerization or oligomerization of receptors, which then results in activation of intracellular enzymatic or signaling domains. However, while this model has been shown to be true to the first approximation, it does not explain how the signaling output of the receptor can be tuned by native or artificial ligands[131,132]. In this research we discovered a general mechanism through which the activation setpoint of CaSR, a dimeric class C GPCR, is finely tuned. We propose that this design is potentially prevalent in other dimeric receptors.

Existence of the negatively charged patch as an electrostatic control hub for activation could explain how CaSR can function as a salinity sensor as proposed in euryhaline fishes [54,55]. Interestingly, we showed that, between different species, the charge distribution on the LB2 of CaSR is extremely variable, much more than mGluRs or the LB1 of CaSR. We showed how this design element of CaSR enables tuning the sensitivity of the receptor. Evolution could have used this design feature to optimize CaSR to suit the environmental niche of an animal through discrete

evolutionary changes in the charge density of the dimeric interface. Variations of ligand binding pocket to tune ligand affinity is limited and does not map a large phase space. However, the electrostatic tuning mechanism that we described is generalizable and maps the phase space of interface charge distribution to the phase space of receptor sensitivity. Finally, while none of the atomic structures show Ca^{2+} binding at the negative patch on LB2 (Figure S4.1d), it is possible that transient or weak binding of Ca^{2+} at this region could contribute to CaSR activation via screening the negative charges. This interpretation is consistent with previous reports based on mutagenesis and fragment analysis[68,71] and positively charged residues emulate this proposed effect.

MATERIALS & METHODS

Molecular cloning

Same as previously described in Chapter 2.

Point mutations in D451UAA CaSR (R227L, E228K, E249K, E251K, V254R) were introduced using a QuikChange site-directed mutagenesis kit (Qiagen).

Cell culture conditions

Same as previously described in Chapter 2.

Transfection and protein expression

Same as previously described in Chapter 2.

Unnatural amino acid labeling in live cells by azide-alkyne click chemistry

Same as previously described in Chapter 2.

Single-molecule FRET measurements

Same as previously described in Chapter 3.

smFRET data analysis

Same as previously described in Chapter 3.

Calcium Mobilization Assay

Same as previously described in Chapter 2.

Analysis of multiple sequence alignments

CaSR and mGluR2 homologs were pulled from ensembl[121] (version 103) using the REST API (gene IDs: ENSG00000036828, ENSG00000164082). Two sequences shorter than 600 amino acids were discarded. All alignments were created using MUSCLE[122] and default parameters. The conservation of charged residues (Lys, Arg, Glu, Asp) was defined as: $\frac{\#\ Charged\ Residues\ Observed}{\#\ Sequences}$

Structural analyses

Prior to the calculation of electrostatic potential, hydrogens were added using the AddH tool in chimera and PROPKA[133,134] with pH of 7.4 was used to determine protonation state of residues. Electrostatic potential maps were calculated in Chimera using APBS[135] and PDB2PQR[136] using the PARSE force field.

CHAPTER 5: THE STRUCTURE-FUNCTION RELATIONSHIP OF DISEASE-ASSOCIATED MUTATIONS

INTRODUCTION

Numerous disease-associated mutations in CaSR have been identified[137], which generally cause hypercalcaemic or hypocalcaemic disorders as well as some cancers[45]. Many of these mutations are away from known ligand-binding sites on CaSR and exert their effect allosterically by modulating the intersubunit cooperativity and crosstalk. A general framework for understanding how these mutations alter receptor topology and dynamics to influence the strength of signal output is unknown. An improvement in understanding the relationship between the structure and function of disease-associated mutations could inform the design of additional therapeutics for CaSR and give insight into the process of activation. Here, I characterize 9 disease-associated mutations of CaSR by smFRET. I show that point mutations can alter both the unliganded and fully liganded conformation of the VFT of CaSR with receptor dynamics and not specific receptor topology correlating with altered phenotype.

RESULTS

We asked how disease-associated mutations in CaSR distort the canonical structure and conformational dynamics of the receptor to cause the pathological effect. There are over 200 known disease-associated mutations in CaSR that generally cause hypercalcemia, hyperparathyroidism, hypocalcemic hypercalciuria, and Bartter syndrome type V[45,118,138,139]. Many

of these mutations map to the extracellular dimer interface and away from the residues that are known to be involved in ligand coordination and therefore exert their effect allosterically (Figure 5.1a). We tested several of these mutations that either sensitize (reduce EC_{50}) or desensitize (increase EC_{50}) the receptor to Ca^{2+}.

Characterization of SNAP-tagged mutants by smFRET showed that, while all the tested mutants can signal (Figure S5.1a,b) with altered EC_{50}, they adopt a diverse range of architecture at the extracellular domain in their active and inactive states, as measured from smFRET histograms (Figure 5.1b and Figure S5.1c). Moreover, we found no correlation between the physiological effect of a mutation and how FRET distribution changed compared to the canonical receptor (Figure 5.1b). For example, $C129S^{140}$ and C131G are both sensitizing mutations, but they have opposite effect on the FRET distribution. However, we found that all sensitizing mutations that we tested showed a reduction in the cross-correlation amplitude in the absence of ligand compared to the wildtype CaSR (Figure 4.2c). By contrast, the cross-correlation amplitude of desensitizing mutations was higher in the presence of Ca^{2+} (Figure 5.1c). Overall, these results reveal a large degree of permissiveness in CaSR dimer architecture that was previously unknown and indicate a complex relationship between subtle sequence variations, coordination of the ECD of CaSR, and the receptor sensitivity.

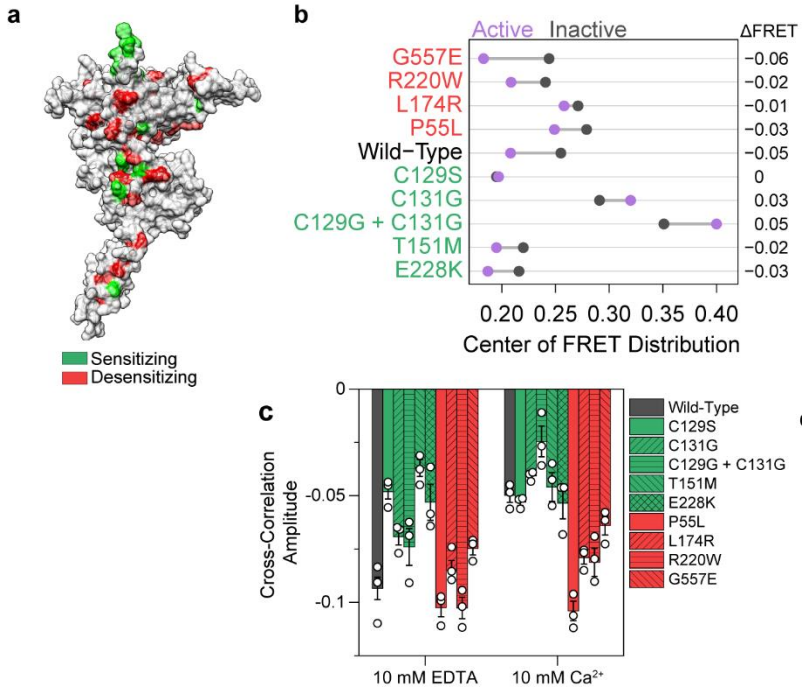

Figure 5.1 – Changes in CaSR dynamics by mutation predict calcium sensitivity.

A Surface representation of CaSR (PDB 5K5T) with known sensitizing (green) and desensitizing (red) mutations mapped to the structure. **B** Barbell plot showing the center of the FRET distribution in the inactive condition (10 mM EDTA, gray) and active condition (10 mM Ca^{2+} + 5 mM L-Trp, purple) for CaSR mutants. Mutants that desensitize (red) or sensitize the receptor (green) are grouped together. The amplitude of the FRET shift is shown on the right. **C** Amplitude of receptor cross correlation of wild-type (gray), sensitizing (green) mutations, and desensitizing (red) mutations in the presence of 10 mM EDTA or 10 mM Ca^{2+}.

DISCUSSION

We found that many disease-associated mutations considerably distort the arrangement of the ECD of CaSR without abolishing its ability to signal (with altered EC_{50}). This result indicates that the ECD conformation of CaSR is promiscuous and tolerates a range of alternative topologies. This conformational flexibility was likely used throughout evolution of class C GPCRs to explore the structural landscape. Furthermore, modifying the topology of the extracellular domain of CaSR to compensate for the effect of disease-associated mutations may be utilized for drug-based therapies. Such therapeutic strategy could potentially be applied to similar bilobed shaped receptors such as other class C GPCRs and the ionotropic glutamate receptors.

MATERIALS & METHODS

Molecular cloning

Same as previously described in Chapter 2.

Point mutations in SNAP-tag CaSR (P55L, C129S, C131G, C129G + C131G, T151M, L174R, R220W, R227L, E228K, G557E) were introduced using a QuikChange site-directed mutagenesis kit (Qiagen). T

Cell culture conditions

Same as previously described in Chapter 2.

Transfection and protein expression

Same as previously described in Chapter 2.

SNAP-tag labeling in live cells

Same as previously described in Chapter 2.

Single-molecule FRET measurements

Same as previously described in Chapter 3.

smFRET data analysis

Same as previously described in Chapter 3.

Calcium Mobilization Assay

Same as previously described in Chapter 2.

CHAPTER 6: CONCLUSIONS & FUTURE WORK

CONCLUSIONS

Unnatural Amino Acids are an efficient platform for bioconjugation

Optimizing fluorophore bioconjugation is a time-intensive step in smFRET experiments. The kinetics of the labeling method play a significant role in labeling efficiency, but in our data, accessibility of the labeling site is the most important factor to consider. The difficulty of predicting the folding, orientation, or non-specific interactions of a peptide tag make it incredibly challenging to rationally engineer labeling sites, but advances in the prediction of protein folding with AlphaFold2[141] and RoseTTAFold[142] may make this more feasible in the future.

The results in chapter 2 demonstrate that incorporation of unnatural amino acids is the most successful strategy for the bioconjugation of fluorescent probes. Due to their small size, unnatural amino acids are the least perturbative strategy, and the use of copper-free Tetrazine-TCO click chemistry results in efficient labeling for both *in vivo* and smFRET experimentation. Another advantage of this method is the ease of generating potential FRET sensors. The incorporation of UAAs can be done with site-directed mutagenesis, but the size of peptide-based tags necessitates the use of more complex cloning strategies (e.g., blunt-end ligation or Gibson assembly) that are more likely to fail or have errors. This makes the UAA method of bioconjugation appealing as a greater number of FRET sensors can be created and screened more easily.

In the future, this system could be improved by the use of multiple labeling chemistries and additional codons (e.g., the *opal* codon) to facilitate simultaneous, orthogonal labeling. This would enable the development of sensors for 3-color FRET experiments capable of tracking

multiple domains simultaneously. It would also provide better information regarding the proteins 3-dimensional configuration, which would result in better models of protein function.

CaSR activation is best modeled by conformational selection

Ligand-induced protein conformational change is broadly observed in proteins, and it is thought to occur through one of two possible mechanisms: (1) ligand-induced conformational change or (2) conformational selection[143]. In chapter 3, we demonstrated the ability of the CaSR VFT to frequently sample the active FRET state in the absence of ligand, and this contrasts with the mGluRs, which only undergo conformational change when glutamate is present[57,144]. In fact, CaSR is at its most dynamic in the absence of ligands as quantified by the width of FRET histograms (Figure S3.1d). This behavior is consistent with a low energy barrier between conformations (Figure 6.1a) and a conformational selection model where calcium binds preferentially once the VFT adopts the active FRET state. Our analysis of disease-associated mutations presented in Chapter 5 highlights the importance of protein dynamics in CaSR activation, and it is appealing to think that the phenotype of a mutation is driven by how the ability of CaSR to sample the active FRET state is altered.

Chapter 3 successfully revealed the activation of CaSR for two domains allowing us to build a more complete model of CaSR activation (Figure 3.6). Consistent with published literature, there is a loose allosteric coupling[99] between the VFT and the CRD. Calcium is both necessary and sufficient for activation of the receptor, and without calcium, the CRD fails to reach the active FRET state – a necessary step for receptor activation.

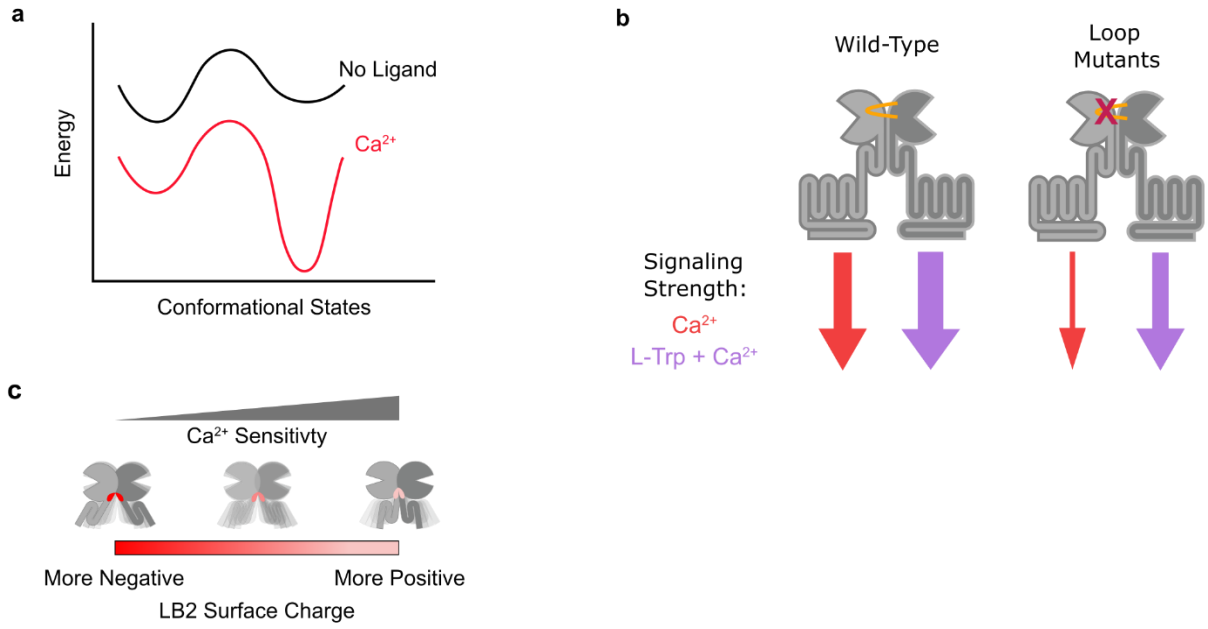

Figure 6.1 – Graphical summary of primary findings.

a Schematic conformational energy landscape of CaSR in the absence of ligand (black) and in the presence of Ca^{2+} (red). **b** Cartoon schematic of CaSR showing the effect of interprotomer loop mutations on the relative contribution of L-Trp to signaling strength. **c** Model of CaSR illustrating how the LB2 surface charge modulates sensitivity. As the LB2 becomes more positive, the stability of the active interface increases resulting in increased receptor sensitivity.

Amino acids are PAMs

In Chapter 3, we demonstrate the reversibility of amino acid binding and demonstrate calcium is sufficient for activation, which has been debated in the literature[68,73,80,145]. Instead of acting as co-agonists, amino acids purely act as PAMs whose molecular basis of action is to close

the flytrap as seen in CryoEM structures[74] and potentially increase engagement of the LB2-LB2 interface, which has not been observed before. This is in stark contrast to other class C members that require amino acids to activate. One structural feature that partially explains the divergence of amino acids in CaSR compared to other class C receptors is an interprotomer loop.

This loop increases the surface contact area of the LB1-LB1 interface (Figure 3.5), and a recent structure shows that these contacts are incompatible with an mGluR-like inactive conformation[75]. It makes it likely that this loop is responsible for the more 'active-like' resting state of CaSR that has been observed in many structures. We demonstrate that mutations or truncation of this loop increase the contribution of L-Trp to receptor activation, and this results in a larger PAM effect for the mutant receptors than wild-type CaSR (Figure 6.1b).

An electrostatic surface is a platform for tuning Ca^{2+} sensitivity

In Chapter 4, we explored the possibility that calcium sensitivity could be related with the difference in CaSR sequence observed in various species. Particularly, we observed variation of charged residues in a highly electronegative surface that is effective at adjusting CaSR sensitivity Figure 6.1c). This surface may also act to tune sensitivity given other parameters of the physiological environment it is expressed (e.g., pH, salt, nutrient concentration). For instance, CaSR is expressed in multiple fish organs and has been suggested it acts as a salinity sensor[54,55,127]. From a broader perspective, context-dependent oligomerization is a ubiquitous means of communicating information in biology. It is exciting to speculate that the method of indirectly regulating a receptor's ligand affinity through protein interfaces observed in CaSR is applicable to other receptor families.

FUTURE WORK

CaSR conformational dynamics

One of the major limitations of this work is the inability to probe structural dynamics faster than 5 ms, which is the current limit of the experimental setup. This could be overcome by two methods. First, a strobeascopic approach to illumination has been used to improve temporal resolution of FRET states[146,147]and would help to illuminate any intermediates we were not able to visualize; however, this approach would not provide the sequence of FRET states like the current method of constant illumination does. Second, advancements in detector technology have greatly improved sCMOS, and it is now possible to produce detectors that are capable of very fast read speeds and low noise making them attractive alternatives to emCCD detectors for single-molecule experiments.

One area of ambiguity is the effect of amino acid binding on the VFT structure. Our data indicate that amino acids increase the occupancy of the active FRET state for the VFT and NaCl modulates the magnitude of this effect, which we interpret to mean engagement of the LB2-LB2 interface. But whether amino acid binding is capable of bring the LB2s of each protomer into proximity has not been specifically demonstrated. The creation of a FRET sensor to specifically detect this conformational change would help to further clarify the full activation process of CaSR. Another question that remains is if the spontaneous visits to the active FRET state observed in the absence of ligand involve closure of the VFT domain, and the creation of an LB1-LB2 intra-protomer sensor would answer this.

In Chapter 5 we demonstrate the effect of a mutation on receptor dynamics is a better predictor of phenotype than the effect on the structure. While their effect on dynamics appears to be the driving factor of its impact, they likely act on different parts of the CaSR activation mechanism. Interestingly, there are 3 residues (Q27, N178, and P221) that functionally serve as allosteric switches where, depending upon the specific mutation, can have opposing effects on receptor function[148]. It would be interesting to see if the switch mutants have opposing effects on the structure and dynamics of the CaSR activation mechanism or if these switch mutants operate through independent pathways.

Detailed mechanism electrostatic tuning

Chapter 4 demonstrated the ability to modulate ligand sensitivity and active state occupancy by altering the distribution of negatively and positively charged residues in the LB2 interface, but it is unclear if the increase of active state occupancy is caused by an increase in the lifetime of or the rate of transition to the active state. In our data, we observed brief (2-5 data point) transitions to active FRET states quite frequently. Because of this, quantifying the lifetime of the active FRET state was not reasonable, which would have answered this question. Unfortunately, without increased temporal resolution, it may not be possible to answer this question with smFRET.

It is important to point out that the novel mutations made in the helix-sheet-helix LB2 fold do not appear to make direct contact with the adjacent protomer in the active state. While this does not invalidate a model of electrostatic tuning, it does suggest that they may not directly affect the stability of the fully active conformation. Instead, it is probable that they make intermediate

interactions with the adjacent protomer, and instead of increasing active FRET state occupancy by stabilizing the LB2-LB2 interface, they increase the frequency of transitions to the active FRET state. Molecular dynamics simulations can provide insight into what, if any, transient contacts are made, and it can be a source of new hypotheses to test.

Dimer interfaces are a general platform for sensitivity-tuning

Every cell must translate extracellular information from chemical or physical signals to the biochemical language of the cell. This task is usually initiated by membrane receptors and often requires allosteric communication between the extracellular ligand-binding region and the intracellular effector region of the receptor. Receptor dimerization upon ligand binding is a ubiquitous mechanism to initiate signal transduction and is widely used in receptors, such as bacterial chemotaxis receptors, receptor tyrosine kinases (RTKs), cytokine receptors, and some GPCRs[103,149,150]. This approach is generalizable and has been used to engineer synthetic switches or modulate signaling output of native receptors by artificial ligands[149,151,152]. While this approach seems applicable more broadly to other dimeric receptors, the next step would be a demonstration that interface modification can alter ligand sensitivity for other receptor families.

REFERENCES

1 Ringer, S. A further Contribution regarding the influence of the different Constituents of the Blood on the Contraction of the Heart. *J. Physiol.* **4**, 29-42.23, doi:10.1113/jphysiol.1883.sp000120 (1883).

2 Clapham, D. E. Calcium Signaling. *Cell* **131**, 1047-1058, doi:10.1016/j.cell.2007.11.028 PMID - 18083096 (2007).

3 Goldstein, D. A. in *Clinical Methods: The History, Physical, and Laboratory Examinations* (eds rd, H. K. Walker, W. D. Hall, & J. W. Hurst) (1990).

4 Bushinsky, D. A. & Monk, R. D. Electrolyte quintet: Calcium. *Lancet* **352**, 306-311, doi:10.1016/s0140-6736(97)12331-5 (1998).

5 Maccallum, W. G. & Voegtlin, C. On the Relation of Tetany to the Parathyroid Glands and to Calcium Metabolism. *J. Exp. Med.* **11**, 118-151, doi:10.1084/jem.11.1.118 (1909).

6 Maccallum, W. G., Lambert, R. A. & Vogel, K. M. The Removal of Calcium from the Blood by Dialysis in the Study of Tetany. *J. Exp. Med.* **20**, 149-168, doi:10.1084/jem.20.2.149 (1914).

7 Westerdahl, J., Lindblom, P., Valdemarsson, S., Tibblin, S. & Bergenfelz, A. Risk factors for postoperative hypocalcemia after surgery for primary hyperparathyroidism. *Arch. Surg.* **135**, 142-147, doi:10.1001/archsurg.135.2.142 (2000).

8 Vasher, M., Goodman, A., Politz, D. & Norman, J. Postoperative calcium requirements in 6,000 patients undergoing outpatient parathyroidectomy: easily avoiding symptomatic hypocalcemia. *J. Am. Coll. Surg.* **211**, 49-54, doi:10.1016/j.jamcollsurg.2010.03.019 (2010).

9 Fox, J. & Heath, H., 3rd. The "calcium clamp": effect of constant hypocalcemia on parathyroid hormone secretion. *Am. J. Physiol.* **240**, E649-655, doi:10.1152/ajpendo.1981.240.6.E649 (1981).

10 Conlin, P. R., Fajtova, V. T., Mortensen, R. M., LeBoff, M. S. & Brown, E. M. Hysteresis in the relationship between serum ionized calcium and intact parathyroid hormone during recovery from induced hyper- and hypocalcemia in normal humans. *J. Clin. Endocrinol. Metab.* **69**, 593-599, doi:10.1210/jcem-69-3-593 (1989).

11 Raisz, L. G. Bone Resorption in Tissue Culture. Factors Influencing the Response to Parathyroid Hormone. *J. Clin. Invest.* **44**, 103-116, doi:10.1172/JCI105117 (1965).

12 Agus, Z. S., Gardner, L. B., Beck, L. H. & Goldberg, M. Effects of parathyroid hormone on renal tubular reabsorption of calcium, sodium, and phosphate. *Am. J. Physiol.* **224**, 1143-1148, doi:10.1152/ajplegacy.1973.224.5.1143 (1973).

13 Bilezikian, J. P., Marcus, R. & Levine, M. A. *The parathyroids : basic and clinical concepts*. 2nd edn, (Academic Press, 2001).

14 Brown, E. M. Clinical lessons from the calcium-sensing receptor. *Nat Clin Pract Endocrinol Metab* **3**, 122-133, doi:10.1038/ncpendmet0388 (2007).

15 Brown, E. M., Hurwitz, S. & Aurbach, G. D. Preparation of viable isolated bovine parathyroid cells. *Endocrinology* **99**, 1582-1588, doi:10.1210/endo-99-6-1582 (1976).

16 Morrissey, J. J. & Cohn, D. V. The effects of calcium and magnesium on the secretion of parathormone and parathyroid secretory protein by isolated porcine parathyroid cells. *Endocrinology* **103**, 2081-2090, doi:10.1210/endo-103-6-2081 (1978).
17 Birnbaumer, M. E., Schneider, A. B., Palmer, D., Hanley, D. A. & Sherwood, L. M. Secretion of parathyroid hormone by abnormal human parathyroid glands in vitro. *J. Clin. Endocrinol. Metab.* **45**, 105-113, doi:10.1210/jcem-45-1-105 (1977).
18 Brown, E. M. *et al.* Dispersed cells prepared from human parathyroid glands: distinct calcium sensitivity of adenomas vs. primary hyperplasia. *J. Clin. Endocrinol. Metab.* **46**, 267-275, doi:10.1210/jcem-46-2-267 (1978).
19 Brown, E. M. *et al.* Calcium-regulated parathyroid hormone release in primary hyperparathyroidism: studies in vitro with dispersed parathyroid cells. *Am. J. Med* **66**, 923-931, doi:10.1016/0002-9343(79)90446-7 (1979).
20 Blum, J. W. *et al.* Rapidity of plasma 1,25-dihydroxyvitamin D responses to hypo- and hypercalcemia in steers. *Endocrinology* **113**, 523-526, doi:10.1210/endo-113-2-523 (1983).
21 Brown, E. M. *et al.* Mechanisms underlying the inverse control of parathyroid hormone secretion by calcium. *Soc. Gen. Physiol. Ser.* **44**, 251-268 (1989).
22 Brown, E. M. *et al.* Cloning and characterization of an extracellular Ca2+-sensing receptor from bovine parathyroid. *Nature* **366**, 575-580, doi:10.1038/366575a0 PMID - 8255296 (1993).
23 Smith, J. S., Lefkowitz, R. J. & Rajagopal, S. Biased signalling: from simple switches to allosteric microprocessors. *Nat Rev Drug Discov* **17**, 243, doi:10.1038/nrd.2017.229 PMID - 29302067 (2018).
24 Zhang, C. *et al.* Molecular Basis of the Extracellular Ligands Mediated Signaling by the Calcium Sensing Receptor. *Front. Physiol.* **7**, 441, doi:10.3389/fphys.2016.00441 (2016).
25 Brown, E. M. & MacLeod, R. J. Extracellular Calcium Sensing and Extracellular Calcium Signaling. *Physiol Rev* **81**, 239-297, doi:10.1152/physrev.2001.81.1.239 PMID - 11152759 (2001).
26 Zhang, C. *et al.* Role of Ca2+ and L-Phe in Regulating Functional Cooperativity of Disease-Associated "Toggle" Calcium-Sensing Receptor Mutations. *Plos One* **9**, e113622, doi:10.1371/journal.pone.0113622 PMID - 25420019 (2014).
27 Conigrave, A. D., Mun, H. C. & Lok, H. C. Aromatic L-amino acids activate the calcium-sensing receptor. *J. Nutr.* **137**, 1524S-1527S; discussion 1548S, doi:10.1093/jn/137.6.1524S (2007).
28 Conigrave, A. D., Quinn, S. J. & Brown, E. M. Cooperative multi-modal sensing and therapeutic implications of the extracellular Ca2+ sensing receptor. *Trends Pharmacol Sci* **21**, 401-407, doi:10.1016/s0165-6147(00)01546-7 PMID - 11050321 (2000).
29 Conigrave, A. D., Quinn, S. J. & Brown, E. M. L-amino acid sensing by the extracellular Ca2+-sensing receptor. *Proc. Natl. Acad. Sci. USA* **97**, 4814-4819, doi:10.1073/pnas.97.9.4814 (2000).
30 Alfadda, T. I., Saleh, A. M. A., Houillier, P. & Geibel, J. P. Calcium-sensing receptor 20 years later. *Am J Physiology Cell Physiology* **307**, C221-231, doi:10.1152/ajpcell.00139.2014 PMID - 24871857 (2014).

31 Tfelt-Hansen, J. & Brown, E. M. The calcium-sensing receptor in normal physiology and pathophysiology: a review. *Crit Rev Clin Lab Sci* **42**, 35-70, doi:10.1080/10408360590886606 (2005).

32 Brown, E. M. Role of the calcium-sensing receptor in extracellular calcium homeostasis. *Best Pract. Res. Clin. Endocrinol. Metab.* **27**, 333-343, doi:10.1016/j.beem.2013.02.006 (2013).

33 Loot, A. E. *et al.* Ca2+-sensing receptor cleavage by calpain partially accounts for altered vascular reactivity in mice fed a high-fat diet. *J. Cardiovasc. Pharmacol.* **61**, 528-535, doi:10.1097/FJC.0b013e31828d0fa3 (2013).

34 Schepelmann, M. *et al.* The vascular Ca2+-sensing receptor regulates blood vessel tone and blood pressure. *Am. J. Physiol., Cell Physiol.* **310**, C193-204, doi:10.1152/ajpcell.00248.2015 (2016).

35 Oda, Y., Tu, C. L., Pillai, S. & Bikle, D. D. The calcium sensing receptor and its alternatively spliced form in keratinocyte differentiation. *J. Biol. Chem.* **273**, 23344-23352, doi:10.1074/jbc.273.36.23344 (1998).

36 Vizard, T. N. *et al.* Regulation of axonal and dendritic growth by the extracellular calcium-sensing receptor. *Nat Neurosci* **11**, 285-291, doi:10.1038/nn2044 (2008).

37 Garrett, J. E. *et al.* Molecular cloning and functional expression of human parathyroid calcium receptor cDNAs. *J. Biol. Chem.* **270**, 12919-12925, doi:10.1074/jbc.270.21.12919 (1995).

38 Riccardi, D. *et al.* Cloning and functional expression of a rat kidney extracellular calcium/polyvalent cation-sensing receptor. *Proc Natl Acad Sci U S A* **92**, 131-135, doi:10.1073/pnas.92.1.131 (1995).

39 Pidasheva, S., D'Souza-Li, L., Canaff, L., Cole, D. E. & Hendy, G. N. CASRdb: calcium-sensing receptor locus-specific database for mutations causing familial (benign) hypocalciuric hypercalcemia, neonatal severe hyperparathyroidism, and autosomal dominant hypocalcemia. *Hum. Mutat.* **24**, 107-111, doi:10.1002/humu.20067 (2004).

40 Kooistra, A. J. *et al.* GPCRdb in 2021: integrating GPCR sequence, structure and function. *Nucleic Acids Res.* **49**, D335-D343, doi:10.1093/nar/gkaa1080 (2021).

41 Yano, S., Brown, E. M. & Chattopadhyay, N. Calcium-sensing receptor in the brain. *Cell Calcium* **35**, 257-264, doi:10.1016/j.ceca.2003.10.008 (2004).

42 Ye, C. *et al.* Amyloid-beta proteins activate Ca(2+)-permeable channels through calcium-sensing receptors. *J. Neurosci. Res.* **47**, 547-554, doi:10.1002/(sici)1097-4547(19970301)47:5<547::aid-jnr10>3.0.co;2-v (1997).

43 Kapoor, A. *et al.* An idiopathic epilepsy syndrome linked to 3q13.3-q21 and missense mutations in the extracellular calcium sensing receptor gene. *Ann. Neurol.* **64**, 158-167, doi:10.1002/ana.21428 (2008).

44 Stepanchick, A., McKenna, J., McGovern, O., Huang, Y. & Breitwieser, G. E. Calcium sensing receptor mutations implicated in pancreatitis and idiopathic epilepsy syndrome disrupt an arginine-rich retention motif. *Cell Physiol. Biochem.* **26**, 363-374, doi:10.1159/000320560 (2010).

45 Hannan, F. M., Kallay, E., Chang, W., Brandi, M. L. & Thakker, R. V. The calcium-sensing receptor in physiology and in calcitropic and noncalcitropic diseases. *Nat. Rev. Endocrinol.* **15**, 33-51, doi:10.1038/s41574-018-0115-0 (2018).

46 Liao, J., Schneider, A., Datta, N. S. & McCauley, L. K. Extracellular Calcium as a Candidate Mediator of Prostate Cancer Skeletal Metastasis. *Cancer Res* **66**, 9065-9073, doi:10.1158/0008-5472.can-06-0317 PMID - 16982748 (2006).
47 Tfelt-Hansen, J. *et al.* High calcium activates the EGF receptor potentially through the calcium-sensing receptor in Leydig cancer cells. *Growth Factors* **23**, 117-123, doi:10.1080/08977190500126272 (2005).
48 Tfelt-Hansen, J. *et al.* Calcium-sensing receptor activation induces nitric oxide production in H-500 Leydig cancer cells. *Am. J. Physiol. Endocrinol. Metab.* **288**, E1206-1213, doi:10.1152/ajpendo.00492.2004 (2005).
49 Yano, S. *et al.* Calcium-sensing receptor activation stimulates parathyroid hormone-related protein secretion in prostate cancer cells: role of epidermal growth factor receptor transactivation. *Bone* **35**, 664-672, doi:10.1016/j.bone.2004.04.014 (2004).
50 Tennakoon, S., Aggarwal, A. & Kállay, E. The calcium-sensing receptor and the hallmarks of cancer. *Biochimica Et Biophysica Acta Bba - Mol Cell Res* **1863**, 1398-1407, doi:10.1016/j.bbamcr.2015.11.017 PMID - 26608608 (2016).
51 Joeckel, E. *et al.* High calcium concentration in bones promotes bone metastasis in renal cell carcinomas expressing calcium-sensing receptor. *Mol Cancer* **13**, 42, doi:10.1186/1476-4598-13-42 PMID - 24576174 (2014).
52 Feng, J. *et al.* Prostate Cancer Metastatic to Bone has Higher Expression of the Calcium-Sensing Receptor (CaSR) than Primary Prostate Cancer. *Recept Clin Investigation* **1**, doi:10.14800/rci.270 PMID - 26065011 (2014).
53 Herberger, A. L. & Loretz, C. A. Vertebrate extracellular calcium-sensing receptor evolution: selection in relation to life history and habitat. *Comp. Biochem. Physiol. Part D Genomics Proteomics* **8**, 86-94, doi:10.1016/j.cbd.2012.12.004 (2013).
54 Nearing, J. *et al.* Polyvalent cation receptor proteins (CaRs) are salinity sensors in fish. *Proc. Natl. Acad. Sci. USA* **99**, 9231-9236, doi:10.1073/pnas.152294399 (2002).
55 Loretz, C. A. Extracellular calcium-sensing receptors in fishes. *Comp. Biochem. Physiol. Part A Mol. Integr. Physiol.* **149**, 225-245, doi:10.1016/j.cbpa.2008.01.037 (2008).
56 Pin, J. P. *et al.* Allosteric functioning of dimeric class C G-protein-coupled receptors. *Febs J* **272**, 2947-2955, doi:10.1111/j.1742-4658.2005.04728.x PMID - 15955055 (2005).
57 Vafabakhsh, R., Levitz, J. & Isacoff, E. Y. Conformational dynamics of a class C G-protein-coupled receptor. *Nature* **524**, 497-501, doi:10.1038/nature14679 (2015).
58 Kim, S.-K., Chen, Y., Abrol, R., Goddard, W. A. & Guthrie, B. Activation mechanism of the G protein-coupled sweet receptor heterodimer with sweeteners and allosteric agonists. *Proc National Acad Sci* **114**, 2568-2573, doi:10.1073/pnas.1700001114 PMID - 28228527 (2017).
59 Gutzeit, V. A. *et al.* Conformational dynamics between transmembrane domains and allosteric modulation of a metabotropic glutamate receptor. *Elife* **8**, e45116, doi:10.7554/elife.45116 PMID - 31172948 (2019).
60 Chéron, J.-B. *et al.* Conserved Residues Control the T1R3-Specific Allosteric Signaling Pathway of the Mammalian Sweet-Taste Receptor. *Chem Senses* **44**, 303-310, doi:10.1093/chemse/bjz015 PMID - 30893427 (2019).

61 Ellaithy, A., Gonzalez-Maeso, J., Logothetis, D. A. & Levitz, J. Structural and Biophysical Mechanisms of Class C G Protein-Coupled Receptor Function. *Trends Biochem Sci* **45**, 1049-1064, doi:10.1016/j.tibs.2020.07.008 PMID - 32861513 (2020).
62 Xue, L. *et al.* Rearrangement of the transmembrane domain interfaces associated with the activation of a GPCR hetero-oligomer. *Nat Commun* **10**, 2765, doi:10.1038/s41467-019-10834-5 PMID - 31235691 (2019).
63 Liu, J. *et al.* Allosteric control of an asymmetric transduction in a G protein-coupled receptor heterodimer. *Elife* **6**, e26985, doi:10.7554/elife.26985 PMID - 28829739 (2017).
64 Gao, Y. *et al.* Asymmetric activation of the calcium-sensing receptor homodimer. *Nature* **595**, 455-459, doi:10.1038/s41586-021-03691-0 (2021).
65 Seven, A. B. *et al.* G-protein activation by a metabotropic glutamate receptor. *Nature* **595**, 450-454, doi:10.1038/s41586-021-03680-3 (2021).
66 Hauser, A. S. *et al.* GPCR activation mechanisms across classes and macro/microscales. *Nat Struct Mol Biol* **28**, 879-888, doi:10.1038/s41594-021-00674-7 (2021).
67 Kunishima, N. *et al.* Structural basis of glutamate recognition by a dimeric metabotropic glutamate receptor. *Nature* **407**, 971-977, doi:10.1038/35039564 (2000).
68 Zhang, C. *et al.* Structural basis for regulation of human calcium-sensing receptor by magnesium ions and an unexpected tryptophan derivative co-agonist. *Sci. Adv.* **2**, DOI: 10.1126/sciadv.1600241, doi:10.1126/sciadv.1600241 (2016).
69 Quinn, S. J. *et al.* Sodium and ionic strength sensing by the calcium receptor. *J. Biol. Chem.* **273**, 19579-19586, doi:10.1074/jbc.273.31.19579 (1998).
70 Huang, Y. *et al.* Identification and dissection of Ca(2+)-binding sites in the extracellular domain of Ca(2+)-sensing receptor. *J Biol Chem* **282**, 19000-19010, doi:10.1074/jbc.M701096200 (2007).
71 Huang, Y. *et al.* Multiple Ca2+-Binding Sites in the Extracellular Domain of the Ca2+-Sensing Receptor Corresponding to Cooperative Ca2+Response†. *Biochemistry-us* **48**, 388-398, doi:10.1021/bi8014604 PMID - 19102677 (2009).
72 Jones, E. M. *et al.* Structural and functional characterization of G protein-coupled receptors with deep mutational scanning. *Elife* **9**, doi:10.7554/eLife.54895 (2020).
73 Geng, Y. *et al.* Structural mechanism of ligand activation in human calcium-sensing receptor. *Elife* **5**, e13662, doi:10.7554/eLife.13662 (2016).
74 Ling, S. *et al.* Structural mechanism of cooperative activation of the human calcium-sensing receptor by Ca(2+) ions and L-tryptophan. *Cell Res.* **31**, 383-394, doi:10.1038/s41422-021-00474-0 (2021).
75 Chen, X. *et al.* Structural insights into the activation of human calcium-sensing receptor. *Elife* **10**, doi:10.7554/eLife.68578 (2021).
76 Wen, T. *et al.* Structural basis for activation and allosteric modulation of full-length calcium-sensing receptor. *Sci. Adv.* **7**, DOI: 10.1126/sciadv.abg1483, doi:10.1126/sciadv.abg1483 (2021).
77 Mun, H.-C. *et al.* A Double Mutation in the Extracellular Ca2+-sensing Receptor's Venus Flytrap Domain That Selectively Disables L-Amino Acid Sensing. *J. Biol. Chem.* **280**, 29067-29072, doi:10.1074/jbc.m500002200 PMID - 15888439 (2005).
78 Zhang, C. *et al.* Identification of an l-Phenylalanine Binding Site Enhancing the Cooperative Responses of the Calcium-sensing Receptor to Calcium. *Journal of*

Biological Chemistry **289**, 5296-5309, doi:10.1074/jbc.m113.537357 PMID - 24394414 (2014).

79 Mun, H. C. *et al.* A double mutation in the extracellular Ca2+-sensing receptor's Venus flytrap domain that selectively disables L-amino acid sensing. *Journal of Biological Chemistry* **280**, 29067-29072, doi:10.1074/jbc.M500002200 (2005).

80 Liu, H. *et al.* Illuminating the allosteric modulation of the calcium-sensing receptor. *Proc. Natl. Acad. Sci. USA* **117**, 21711-21722, doi:10.1073/pnas.1922231117 (2020).

81 Keppler, A. *et al.* A general method for the covalent labeling of fusion proteins with small molecules in vivo. *Nat. Biotechnol.* **21**, 86-89, doi:10.1038/nbt765 (2003).

82 Gautier, A. *et al.* An engineered protein tag for multiprotein labeling in living cells. *Chem. Biol.* **15**, 128-136, doi:10.1016/j.chembiol.2008.01.007 (2008).

83 Wilhelm, J. *et al.* Kinetic and Structural Characterization of the Self-Labeling Protein Tags HaloTag7, SNAP-tag, and CLIP-tag. *Biochemistry-us* **60**, 2560-2575, doi:10.1021/acs.biochem.1c00258 (2021).

84 Conigrave, A. D. & Ward, D. T. Calcium-sensing receptor (CaSR): Pharmacological properties and signaling pathways. *Best Pract Res Cl En* **27**, 315-331, doi:10.1016/j.beem.2013.05.010 PMID - 23856262 (2013).

85 McCormick, W. D. *et al.* Increased receptor stimulation elicits differential calcium-sensing receptor(T888) dephosphorylation. *J. Biol. Chem.* **285**, 14170-14177, doi:10.1074/jbc.M109.071084 (2010).

86 Bai, M., Trivedi, S., Kifor, O., Quinn, S. J. & Brown, E. M. Intermolecular interactions between dimeric calcium-sensing receptor monomers are important for its normal function. *Proc National Acad Sci* **96**, 2834-2839, doi:10.1073/pnas.96.6.2834 PMID - 10077597 (1999).

87 Grant, M. P., Stepanchick, A., Cavanaugh, A. & Breitwieser, G. E. Agonist-driven maturation and plasma membrane insertion of calcium-sensing receptors dynamically control signal amplitude. *Sci Signal* **4**, ra78, doi:10.1126/scisignal.2002208 (2011).

88 Cavanaugh, A., McKenna, J., Stepanchick, A. & Breitwieser, G. E. Calcium-sensing receptor biosynthesis includes a cotranslational conformational checkpoint and endoplasmic reticulum retention. *J. Biol. Chem.* **285**, 19854-19864, doi:10.1074/jbc.M110.124792 (2010).

89 Zhou, Z. *et al.* Genetically Encoded Short Peptide Tags for Orthogonal Protein Labeling by Sfp and AcpS Phosphopantetheinyl Transferases. *Acs Chem Biol* **2**, 337-346, doi:10.1021/cb700054k PMID - 17465518 (2007).

90 George, N., Pick, H., Vogel, H., Johnsson, N. & Johnsson, K. Specific labeling of cell surface proteins with chemically diverse compounds. *J. Am. Chem. Soc.* **126**, 8896-8897, doi:10.1021/ja048396s (2004).

91 Lecat-Guillet, N. *et al.* FRET-Based Sensors Unravel Activation and Allosteric Modulation of the GABAB Receptor. *Cell Chem Biol* **24**, 360-370, doi:10.1016/j.chembiol.2017.02.011 PMID - 28286129 (2017).

92 Zhou, Z., Koglin, A., Wang, Y., McMahon, A. P. & Walsh, C. T. An eight residue fragment of an acyl carrier protein suffices for post-translational introduction of fluorescent pantetheinyl arms in protein modification in vitro and in vivo. *J. Am. Chem. Soc.* **130**, 9925-9930, doi:10.1021/ja802657n (2008).

93 Pessino, V., Citron, Y. R., Feng, S. & Huang, B. Covalent Protein Labeling by SpyTag–SpyCatcher in Fixed Cells for Super-Resolution Microscopy. *Chembiochem* **18**, 1492-1495, doi:10.1002/cbic.201700177 PMID - 28514494 (2017).

94 Hatlem, D., Trunk, T., Linke, D. & Leo, J. C. Catching a SPY: Using the SpyCatcher-SpyTag and Related Systems for Labeling and Localizing Bacterial Proteins. *Int. J. Mol. Sci.* **20**, doi:10.3390/ijms20092129 (2019).

95 Keeble, A. H. *et al.* Evolving Accelerated Amidation by SpyTag/SpyCatcher to Analyze Membrane Dynamics. *Angew. Chem. Int. Ed. Engl.* **56**, 16521-16525, doi:10.1002/anie.201707623 (2017).

96 Noren, C. J., Anthony-Cahill, S. J., Griffith, M. C. & Schultz, P. G. A general method for site-specific incorporation of unnatural amino acids into proteins. *Science* **244**, 182-188, doi:10.1126/science.2649980 (1989).

97 Huber, T., Naganathan, S., Tian, H., Ye, S. & Sakmar, T. P. Unnatural amino acid mutagenesis of GPCRs using amber codon suppression and bioorthogonal labeling. *Meth. Enzymol.* **520**, 281-305, doi:10.1016/B978-0-12-391861-1.00013-7 (2013).

98 Serfling, R. & Coin, I. Incorporation of Unnatural Amino Acids into Proteins Expressed in Mammalian Cells. *Meth. Enzymol.* **580**, 89-107, doi:10.1016/bs.mie.2016.05.003 (2016).

99 Liauw, B. W., Afsari, H. S. & Vafabakhsh, R. Conformational rearrangement during activation of a metabotropic glutamate receptor. *Nat. Chem. Biol.* **17**, 291-297, doi:10.1038/s41589-020-00702-5 (2021).

100 Presolski, S. I., Hong, V. P. & Finn, M. G. Copper-Catalyzed Azide-Alkyne Click Chemistry for Bioconjugation. *Curr. Protoc. Chem. Biol.* **3**, 153-162, doi:10.1002/9780470559277.ch110148 (2011).

101 Hong, V., Steinmetz, N. F., Manchester, M. & Finn, M. G. Labeling live cells by copper-catalyzed alkyne-azide click chemistry. *Bioconjug. Chem.* **21**, 1912-1916, doi:10.1021/bc100272z (2010).

102 Schindelin, J. *et al.* Fiji: an open-source platform for biological-image analysis. *Nat. Methods* **9**, 676-682, doi:10.1038/nmeth.2019 (2012).

103 Bai, M., Trivedi, S. & Brown, E. M. Dimerization of the extracellular calcium-sensing receptor (CaR) on the cell surface of CaR-transfected HEK293 cells. *J. Biol. Chem.* **273**, 23605-23610, doi:10.1074/jbc.273.36.23605 (1998).

104 Nuemket, N. *et al.* Structural basis for perception of diverse chemical substances by T1r taste receptors. *Nat. Commun.* **8**, 15530, doi:10.1038/ncomms15530 (2017).

105 Mao, C. *et al.* Cryo-EM structures of inactive and active GABAB receptor. *Cell Res.* **30**, 564-573, doi:10.1038/s41422-020-0350-5 (2020).

106 Park, J. *et al.* Symmetric activation and modulation of the human calcium-sensing receptor. *Proc Natl Acad Sci U S A* **118**, doi:10.1073/pnas.2115849118 (2021).

107 Koehl, A. *et al.* Structural insights into the activation of metabotropic glutamate receptors. *Nature* **566**, 79-84, doi:10.1038/s41586-019-0881-4 PMID - 30675062 (2019).

108 Geng, Y. *et al.* Structure and functional interaction of the extracellular domain of human GABA(B) receptor GBR2. *Nat. Neurosci.* **15**, 970-978, doi:10.1038/nn.3133 (2012).

109 Geng, Y., Bush, M., Mosyak, L., Wang, F. & Fan, Q. R. Structural mechanism of ligand activation in human GABA(B) receptor. *Nature* **504**, 254-259, doi:10.1038/nature12725 (2013).

110 Shaye, H. *et al.* Structural basis of the activation of a metabotropic GABA receptor. *Nature* **584**, 298-303, doi:10.1038/s41586-020-2408-4 (2020).

111 Park, J. *et al.* Structure of human GABAB receptor in an inactive state. *Nature* **584**, 304-309, doi:10.1038/s41586-020-2452-0 (2020).

112 Papasergi-Scott, M. M. *et al.* Structures of metabotropic GABAB receptor. *Nature* **584**, 310-314, doi:10.1038/s41586-020-2469-4 (2020).

113 Xue, L. *et al.* Major ligand-induced rearrangement of the heptahelical domain interface in a GPCR dimer. *Nat. Chem. Biol.* **11**, 134-140, doi:10.1038/nchembio.1711 (2015).

114 Muto, T., Tsuchiya, D., Morikawa, K. & Jingami, H. Structures of the extracellular regions of the group II/III metabotropic glutamate receptors. *Proc. Natl. Acad. Sci. USA* **104**, 3759-3764, doi:10.1073/pnas.0611577104 (2007).

115 Young, S. H. & Rozengurt, E. Amino acids and Ca2+ stimulate different patterns of Ca2+ oscillations through the Ca2+-sensing receptor. *Am. J. Physiol., Cell Physiol.* **282**, C1414-C1422, doi:10.1152/ajpcell.00432.2001 PMID - 11997256 (2002).

116 Saidak, Z., Brazier, M., Kamel, S. & Mentaverri, R. Agonists and allosteric modulators of the calcium-sensing receptor and their therapeutic applications. *Mol. Endocrinol.* **76**, 1131-1144, doi:10.1124/mol.109.058784 (2009).

117 Pearce, S. H. *et al.* Functional characterization of calcium-sensing receptor mutations expressed in human embryonic kidney cells. *J. Clin. Investig.* **98**, 1860-1866, doi:10.1172/JCI118987 (1996).

118 Pearce, S. H. *et al.* Calcium-sensing receptor mutations in familial benign hypercalcemia and neonatal hyperparathyroidism. *J. Clin. Investig.* **96**, 2683-2692, doi:10.1172/JCI118335 (1995).

119 Jain, A., Liu, R., Xiang, Y. K. & Ha, T. Single-molecule pull-down for studying protein interactions. *Nat. Protoc.* **7**, 445-452, doi:10.1038/nprot.2011.452 (2012).

120 van de Meent, J. W., Bronson, J. E., Wiggins, C. H. & Gonzalez, R. L., Jr. Empirical Bayes methods enable advanced population-level analyses of single-molecule FRET experiments. *Biophys.* **106**, 1327-1337, doi:10.1016/j.bpj.2013.12.055 (2014).

121 Yates, A. D. *et al.* Ensembl 2020. *Nucleic Acids Res.* **48**, D682-D688, doi:10.1093/nar/gkz966 (2020).

122 Edgar, R. C. MUSCLE: multiple sequence alignment with high accuracy and high throughput. *Nucleic Acids Res.* **32**, 1792-1797, doi:10.1093/nar/gkh340 (2004).

123 Pettersen, E. F. *et al.* UCSF Chimera--a visualization system for exploratory research and analysis. *J. Comput. Chem.* **25**, 1605-1612, doi:10.1002/jcc.20084 (2004).

124 Guex, N. & Peitsch, M. C. SWISS-MODEL and the Swiss-PdbViewer: an environment for comparative protein modeling. *Electrophoresis* **18**, 2714-2723, doi:10.1002/elps.1150181505 (1997).

125 Hofer, A. M. & Brown, E. M. Extracellular calcium sensing and signalling. *Nat. Rev. Mol. Cell Biol.* **4**, 530-538, doi:10.1038/nrm1154 PMID - 12838336 (2003).

126 Magno, A. L., Ward, B. K. & Ratajczak, T. The calcium-sensing receptor: a molecular perspective. *Endocr. Rev.* **32**, 3-30, doi:10.1210/er.2009-0043 (2011).

127 Hubbard, P. C., Ingleton, P. M., Bendell, L. A., Barata, E. N. & Canario, A. V. Olfactory sensitivity to changes in environmental [Ca(2+)] in the freshwater teleost Carassius auratus: an olfactory role for the Ca(2+)-sensing receptor? *J. Exp. Biol.* **205**, 2755-2764 (2002).
128 White, E., McKenna, J., Cavanaugh, A. & Breitwieser, G. E. Pharmacochaperone-mediated rescue of calcium-sensing receptor loss-of-function mutants. *Mol. Endocrinol.* **23**, 1115-1123, doi:10.1210/me.2009-0041 (2009).
129 D'Souza-Li, L. *et al.* Identification and functional characterization of novel calcium-sensing receptor mutations in familial hypocalciuric hypercalcemia and autosomal dominant hypocalcemia. *J. Clin. Endocrinol. Metab.* **87**, 1309-1318, doi:10.1210/jcem.87.3.8280 (2002).
130 Mayr, B., Glaudo, M. & Schofl, C. Activating Calcium-Sensing Receptor Mutations: Prospects for Future Treatment with Calcilytics. *Trends Endocrinol. Metab.* **27**, 643-652, doi:10.1016/j.tem.2016.05.005 (2016).
131 Liang, S. I. *et al.* Phosphorylated EGFR Dimers Are Not Sufficient to Activate Ras. *Cell Rep.* **22**, 2593-2600, doi:10.1016/j.celrep.2018.02.031 (2018).
132 Moraga, I. *et al.* Tuning cytokine receptor signaling by re-orienting dimer geometry with surrogate ligands. *Cell* **160**, 1196-1208, doi:10.1016/j.cell.2015.02.011 (2015).
133 Sondergaard, C. R., Olsson, M. H., Rostkowski, M. & Jensen, J. H. Improved Treatment of Ligands and Coupling Effects in Empirical Calculation and Rationalization of pKa Values. *J. Chem. Theory Comput.* **7**, 2284-2295, doi:10.1021/ct200133y (2011).
134 Olsson, M. H., Sondergaard, C. R., Rostkowski, M. & Jensen, J. H. PROPKA3: Consistent Treatment of Internal and Surface Residues in Empirical pKa Predictions. *J. Chem. Theory Comput.* **7**, 525-537, doi:10.1021/ct100578z (2011).
135 Jurrus, E. *et al.* Improvements to the APBS biomolecular solvation software suite. *Protein Sci.* **27**, 112-128, doi:10.1002/pro.3280 (2018).
136 Dolinsky, T. J., Nielsen, J. E., McCammon, J. A. & Baker, N. A. PDB2PQR: an automated pipeline for the setup of Poisson-Boltzmann electrostatics calculations. *Nucleic Acids Res.* **32**, W665-667, doi:10.1093/nar/gkh381 (2004).
137 Hendy, G. N., Guarnieri, V. & Canaff, L. Calcium-sensing receptor and associated diseases. *Prog. Mol. Biol. Transl. Sci.* **89**, 31-95, doi:10.1016/S1877-1173(09)89003-0 (2009).
138 Pollak, M. R. *et al.* Autosomal dominant hypocalcaemia caused by a Ca(2+)-sensing receptor gene mutation. *Nat. Genet.* **8**, 303-307, doi:10.1038/ng1194-303 (1994).
139 Watanabe, S. *et al.* Association between activating mutations of calcium-sensing receptor and Bartter's syndrome. *Lancet* **360**, 692-694, doi:10.1016/s0140-6736(02)09842-2 PMID - 12241879 (2002).
140 Hirai, H. *et al.* A novel activating mutation (C129S) in the calcium-sensing receptor gene in a Japanese family with autosomal dominant hypocalcemia. *J. Hum. Genet.* **46**, 41-44, doi:10.1007/s100380170124 (2001).
141 Jumper, J. *et al.* Highly accurate protein structure prediction with AlphaFold. *Nature* **596**, 583-+, doi:10.1038/s41586-021-03819-2 (2021).
142 Baek, M. *et al.* Accurate prediction of protein structures and interactions using a three-track neural network. *Science* **373**, 871-+, doi:10.1126/science.abj8754 (2021).

143 Changeux, J. P. & Edelstein, S. Conformational selection or induced fit? 50 years of debate resolved. *F1000 Biol. Rep.* **3**, 19, doi:10.3410/B3-19 (2011).
144 Vafabakhsh, R., Levitz, J. & Isacoff, E. Y. The Activation Dynamics of Class C Gpcrs Revealed by Single Molecule FRET. *Biophys J* **106**, 194a, doi:10.1016/j.bpj.2013.11.1149 (2014).
145 Young, S. H., Rey, O. & Rozengurt, E. Intracellular Ca2+ oscillations generated via the extracellular Ca2+-sensing receptor (CaSR) in response to extracellular Ca2+ or L-phenylalanine: Impact of the highly conservative mutation Ser170Thr. *Biochem Bioph Res Co* **467**, 1-6, doi:10.1016/j.bbrc.2015.09.144 (2015).
146 Farooq, S. & Hohlbein, J. Camera-based single-molecule FRET detection with improved time resolution. *Phys. Chem. Chem. Phys.* **17**, 27862-27872, doi:10.1039/c5cp04137f (2015).
147 Nicholson, D. A. & Nesbitt, D. J. Pushing Camera-Based Single-Molecule Kinetic Measurements to the Frame Acquisition Limit with Stroboscopic smFRET. *J. Phys. Chem. B* **125**, 6080-6089, doi:10.1021/acs.jpcb.1c01036 (2021).
148 Gorvin, C. M. *et al.* Calcium-sensing receptor residues with loss- and gain-of-function mutations are located in regions of conformational change and cause signalling bias. *Hum Mol Genet* **27**, 3720-3733, doi:10.1093/hmg/ddy263 PMID - 30052933 (2018).
149 Klemm, J. D., Schreiber, S. L. & Crabtree, G. R. Dimerization as a regulatory mechanism in signal transduction. *Annu. Rev. Immunol.* **16**, 569-592, doi:10.1146/annurev.immunol.16.1.569 (1998).
150 Stroud, R. M. & Wells, J. A. Mechanistic diversity of cytokine receptor signaling across cell membranes. *Science Signaling* **2004**, re7, doi:10.1126/stke.2312004re7 (2004).
151 Mohan, K. *et al.* Topological control of cytokine receptor signaling induces differential effects in hematopoiesis. *Science* **364**, eaav7532, doi:10.1126/science.aav7532 (2019).
152 Chang, H. J. & Bonnet, J. Synthetic receptors to understand and control cellular functions. *Meth. Enzymol.* **633**, 143-167, doi:10.1016/bs.mie.2019.11.011 (2020).
153 Ritz, C., Baty, F., Streibig, J. C. & Gerhard, D. Dose-Response Analysis Using R. *Plos One* **10**, e0146021, doi:10.1371/journal.pone.0146021 PMID - 26717316 (2015).

APPENDIX 1: Supplementary Figures

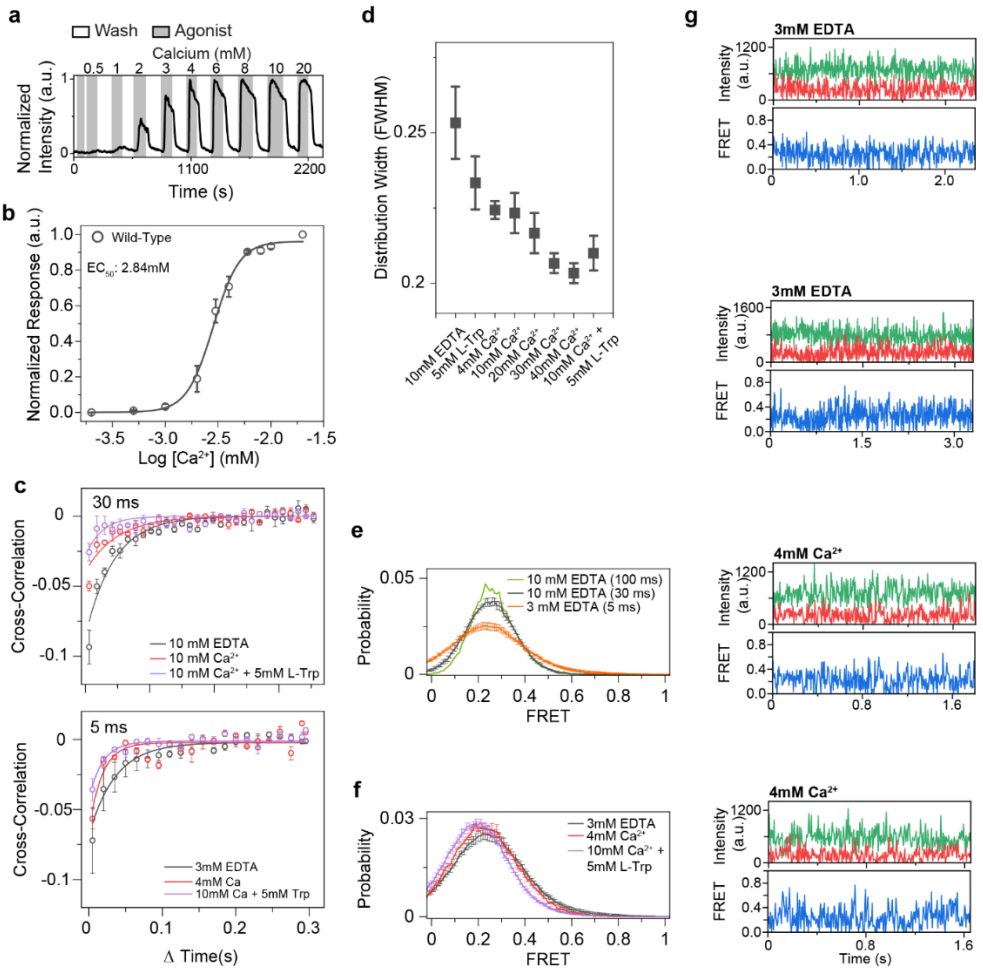

Figure S3.1 – Functional test of SNAP-CaSR and additional single-molecule characterization at different time resolution (100, 30, 5ms) with sample traces.

a Response profile of HEK293T cells expressing SNAP CaSR. Shaded regions indicate when cells were stimulated with calcium. **b** Dose-response curve for wild-type SNAP-CaSR. Data represents mean ± s.e.m. of n=3 independent biological replicates. Data was fit to the hill equation to calculate EC_{50}. **c** Cross-correlation plot quantifying the dynamics of receptors in the presence of 10 mM EDTA, 10 mM Ca^{2+}, or 10 mM Ca^{2+} + 5 mM L-Trp at 5ms (top) and 30ms (bottom) time resolutions. Data represent ± s.e.m of n=3 independent biological replicates. Data was fit to a single exponential decay function. **d** Width of a single gaussian distribution fit to FRET histograms. Data represents the mean ± s.e.m. of n=3 fits to independent biological replicates. **e** smFRET population histogram comparing 100ms, 30ms, and 5ms time resolution in the presence of EDTA. Data represent mean ± s.e.m. of n=3 independent biological replicates for 30 and 5 ms time resolutions and n=1 for 100 ms. **f** smFRET population histogram in the presence of 3 mM EDTA, 10 mM Ca^{2+}, or 10 mM Ca^{2+} and 5 mM L-Trp collected at 5ms time resolution. Data represent mean ± s.e.m. of n=3 independent biological replicates except for 10mM EDTA (100ms), which is Nv=1. **g** Sample single-molecule trace at 5ms time-resolution for SNAP-CaSR in 3 mM EDTA (top) and 4 mM Ca^{2+} (bottom) showing donor (green) and acceptor (red) intensities and corresponding FRET values (blue).

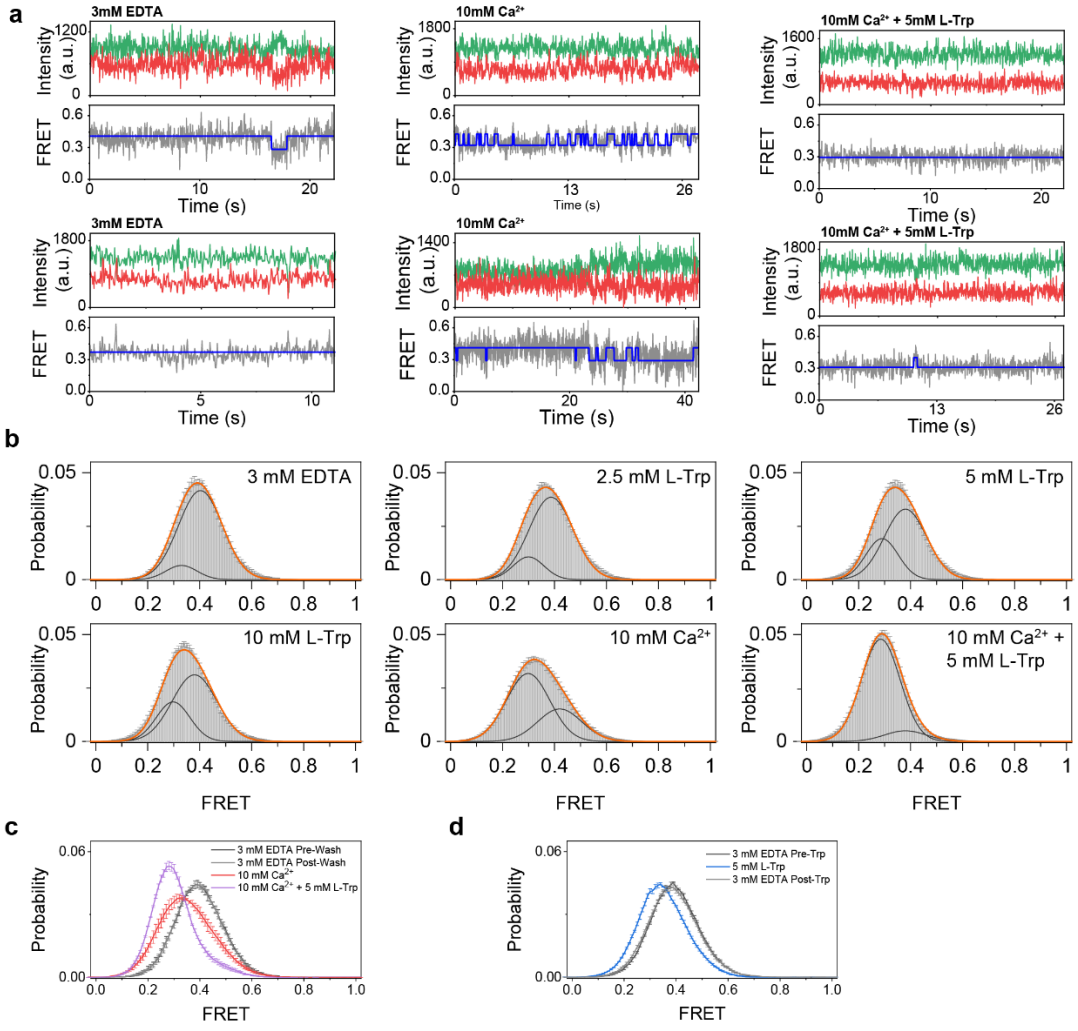
a
3mM EDTA
10mM Ca2+
10mM Ca2+ + 5mM L-Trp
Intensity (a.u.)
FRET
Time (s)
b
3 mM EDTA
2.5 mM L-Trp
5 mM L-Trp
10 mM L-Trp
10 mM Ca2+
10 mM Ca2+ + 5 mM L-Trp
Probability
FRET
c
3 mM EDTA Pre-Wash
3 mM EDTA Post-Wash
10 mM Ca2+
10 mM Ca2+ + 5 mM L-Trp
d
3 mM EDTA Pre-Trp
5 mM L-Trp
3 mM EDTA Post-Trp

Figure S3.2 – Sample traces for D451UAA CaSR.

a Sample single molecule traces of D451UAA in 3 mM EDTA (top), 10 mM Ca^{2+} (middle), and 10 mM Ca^{2+} + 5 mM L-Trp (bottom) showing donor (green) and acceptor (red) intensities, corresponding FRET values (gray), and idealized FRET trajectory from HMM fit (blue). **b** smFRET population histogram in the presence of 3 mM EDTA, 10 mM Ca^{2+}, 2.5 mM L-Trp, 5 mM L-Trp, 10 mM L-Trp, or 10 mM Ca^{2+} and 5 mM L-Trp. Data represent mean ± s.e.m. of n=3 independent biological replicates. Histograms were fit with two single gaussian distributions (black) centered at 0.41 and 0.29, and the cumulative fit is overlaid (orange). **c** smFRET population histograms comparing CaSR before a 2-hour wash (dark gray), after the 2-hour wash (light gray), and in the presence of 10 mM Ca^{2+} (red) and 10 mM Ca^{2+} + 5 mM L-Trp (purple). Pre and post wash histograms overlap. Data represent ± s.e.m of n=3 independent biological replicates. **d** smFRET population histograms comparing 3 mM EDTA before the addition of L-Trp (dark gray), in the presence of L-Trp (blue), and after L-Trp has been washed out (light gray). Pre and post L-Trp histograms overlap. Data represent ± s.e.m of n=3 independent biological replicates.

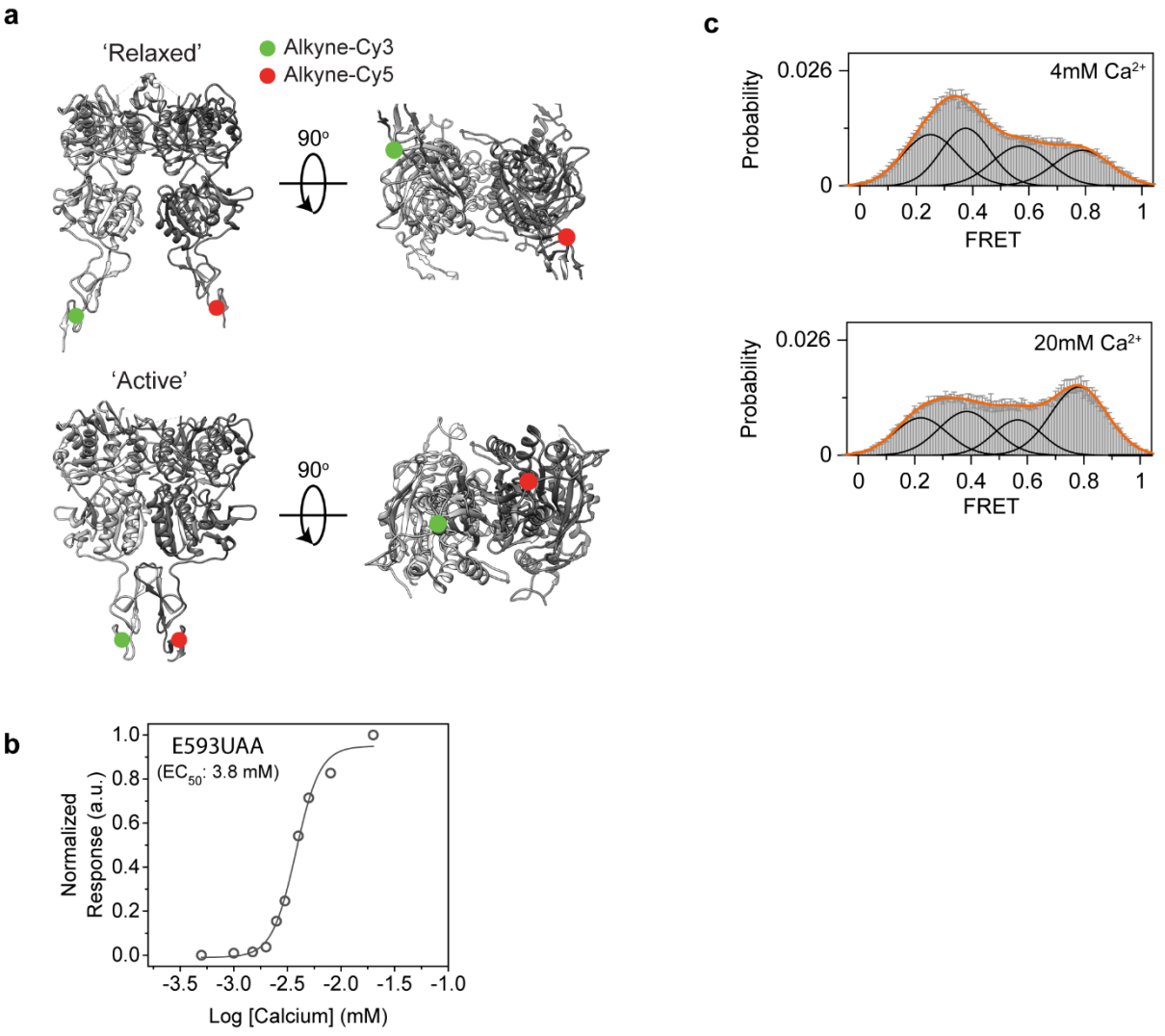
a
'Relaxed'
Alkyne-Cy3
Alkyne-Cy5
90°
'Active'
90°
b
E593UAA
(EC50: 3.8 mM)
Normalized Response (a.u.)
1.0
0.8
0.6
0.4
0.2
0.0
-3.5
-3.0
-2.5
-2.0
-1.5
-1.0
Log [Calcium] (mM)
c
Probability
0.026
0
4mM Ca2+
0
0.2
0.4
0.6
0.8
1
FRET
Probability
0.026
0
20mM Ca2+
0
0.2
0.4
0.6
0.8
1
FRET

Figure S3.3 – smFRET population histograms of D451UAA and E593UAA.

a Ribbon representation of crystal structures PDB 5K5T (top) and PDB 5K5S (bottom) showing approximate location of E593UAA labelling. **b** Dose-response curve of E593UAA. Data represent n=1 independent biological replicate. Data was fit to the hill equation to calculate EC_{50}. **c** smFRET population histogram in the presence of 4 mM Ca^{2+}, or 20 mM Ca^{2+}. Data represent mean ± s.e.m. of n=3 independent biological replicates. Histograms were fit with four single gaussian distributions (black) centered at 0.22, 0.38, 0.56, 0.78, and the cumulative fit is overlaid (orange).

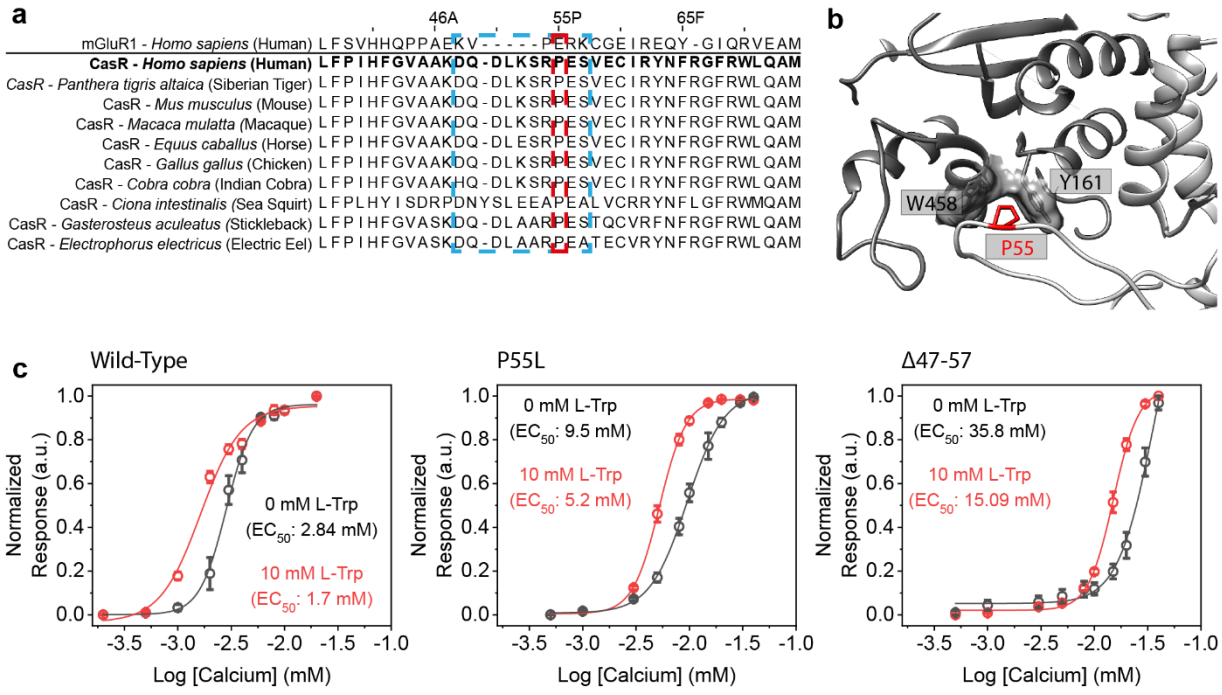

Figure S3.4 – A conserved proline makes critical contacts between protomers.

a Multiple sequence alignment of human mGluR1, human CaSR, and select CaSR orthologues. CaSR is used as reference for residue numbering. Dashed boxes indicate the interprotomer loop (blue) or the conserved proline (red). **b** Close up view of interprotomer loop of CaSR (PDB ID: 5K5S) showing the interaction of P55 (red) and adjacent residues W458 and Y161 with surface representation. **c** Dose-response curves Wild-Type, P55L, and Δ47-57 CaSR in the absence and presence of 10 mM L-Trp. Data represent mean ± s.e.m. of n=3 independent biological replicates. Data was fit to the hill equation to calculate EC_{50}.

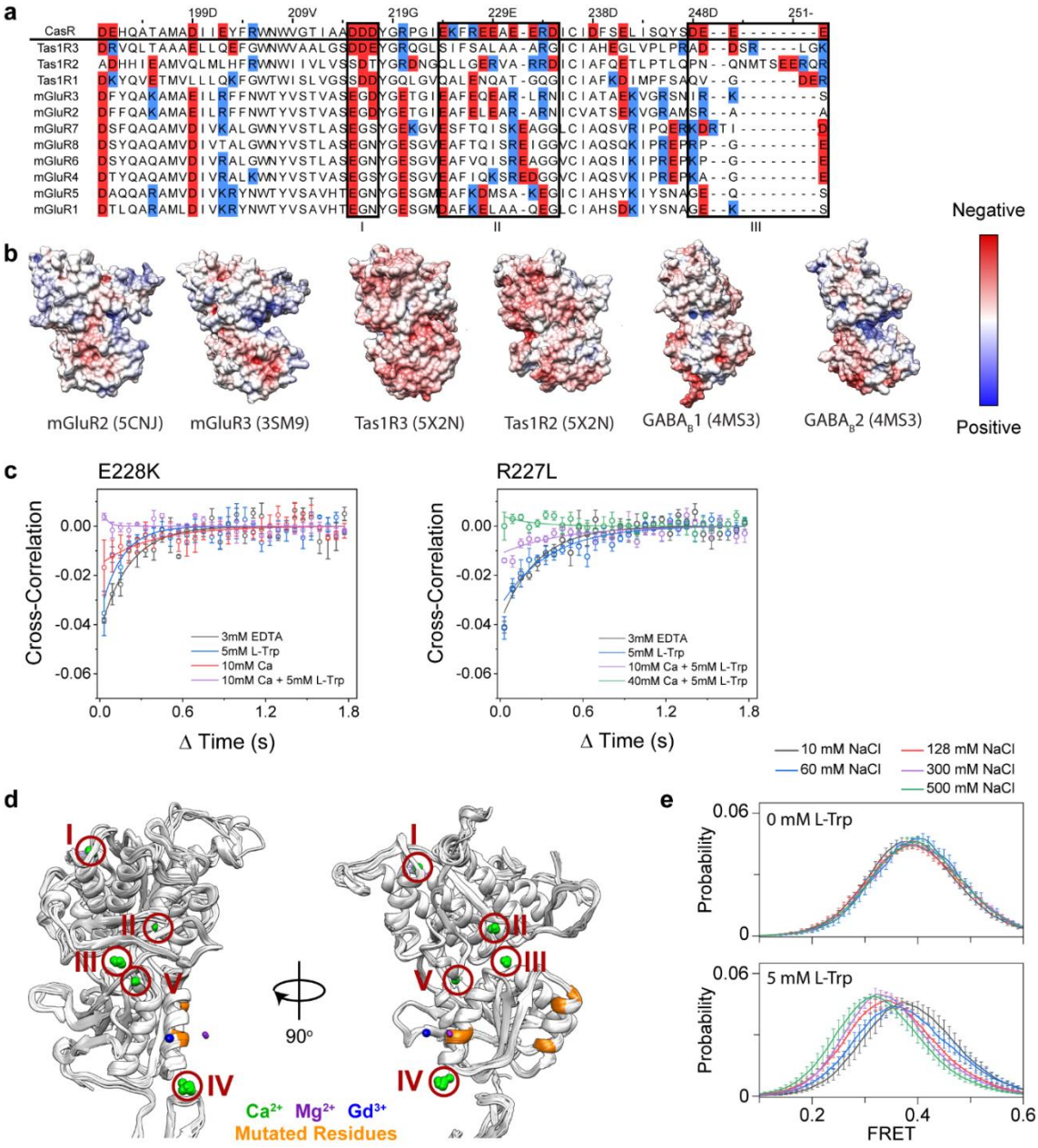
a
199D
209V
219G
229E
238D
248D
251-
CasR
Tas1R3
Tas1R2
Tas1R1
mGluR3
mGluR2
mGluR7
mGluR8
mGluR6
mGluR4
mGluR5
mGluR1
I
II
III
Negative
Positive
b
mGluR2 (5CNJ)
mGluR3 (3SM9)
Tas1R3 (5X2N)
Tas1R2 (5X2N)
GABA$_B$1 (4MS3)
GABA$_B$2 (4MS3)
c
E228K
R227L
Cross-Correlation
Δ Time (s)
3mM EDTA
5mM L-Trp
10mM Ca
10mM Ca + 5mM L-Trp
40mM Ca + 5mM L-Trp
d
90°
Ca2+ Mg2+ Gd3+
Mutated Residues
e
10 mM NaCl
60 mM NaCl
128 mM NaCl
300 mM NaCl
500 mM NaCl
0 mM L-Trp
5 mM L-Trp
Probability
FRET

Figure S4.1 – Multiple sequence alignment and electrostatic surface potential maps of Class C GPCRS.

a Multiple sequence alignment of human CaSR and its human paralogs with negatively charged residues (red) and positively charged residues (blue) highlighted. CaSR is used as reference for residue position. Boxes indicate regions of high charge density unique to CaSR. **b** Electrostatic potential maps for mGluR2, $GABA_B1$, $GABA_B2$, mGluR3, Tas1R3, and Tas1R2. **c** Cross-correlation plot quantifying the dynamics of mutant receptors E228K (left) and R227L (right). Data represent ± s.e.m of n=3 independent biological replicates. Data was fit to a single exponential decay function. **d** Ribbon representation of CaSR structures bound to ions with Ca^{2+} binding sites I-V circled in red. Mutated residues R227, E228, E249, E251, and V258 colored orange. **e** smFRET population histograms with varying concentrations of NaCl and 0 mM L-Trp (top) or 5 mM L-Trp (bottom). Data represent ± s.e.m of n=3 independent biological replicates.

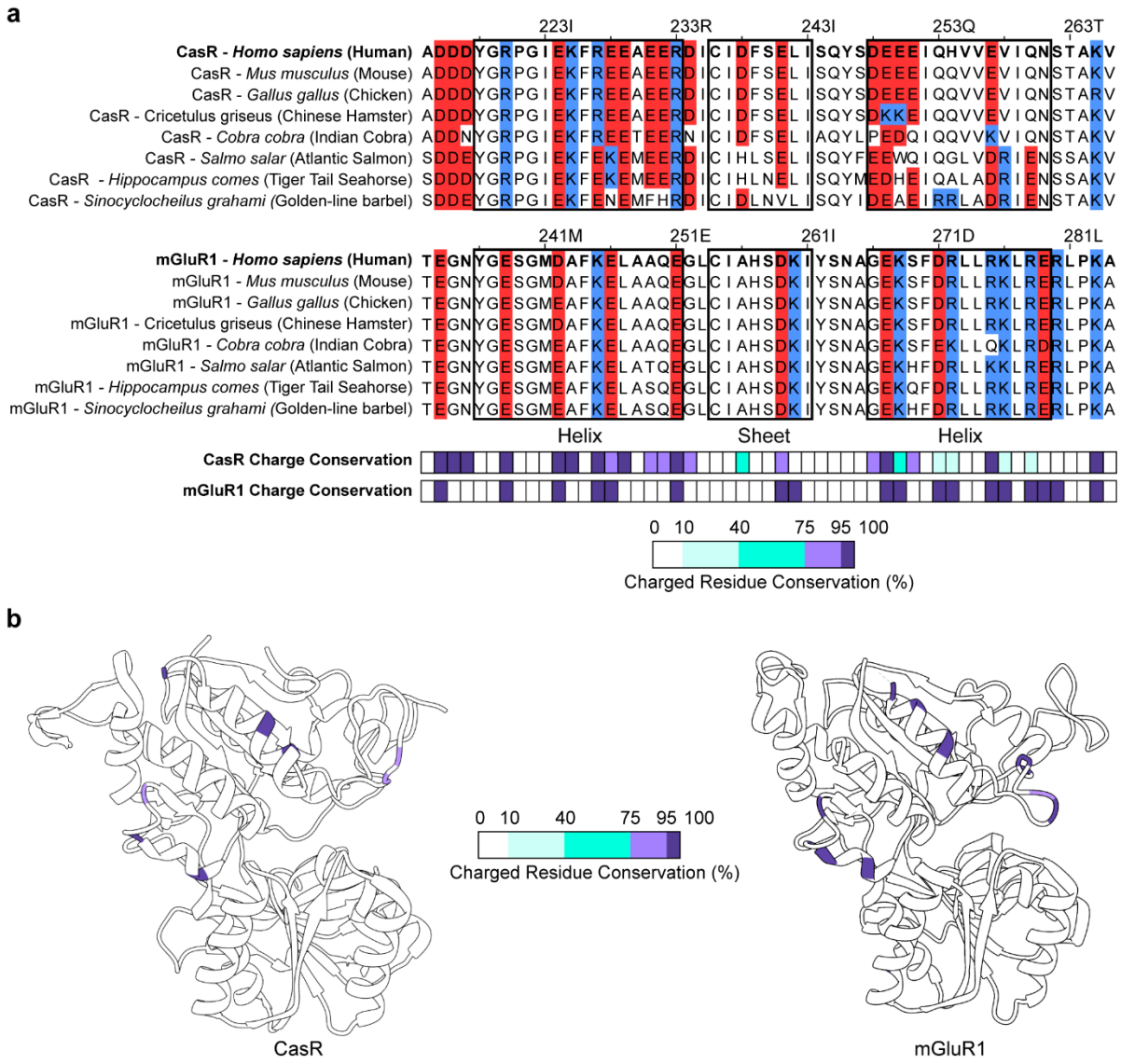
a
223I
233R
243I
253Q
263T
CasR - Homo sapiens (Human) ADDDYGRPGIEKFREEAEERDICIDFSELISQYSDEEEIQHVVEVIQNSTAKV
CasR - Mus musculus (Mouse) ADDDYGRPGIEKFREEAEERDICIDFSELISQYSDEEEIQQVVEVIQNSTAKV
CasR - Gallus gallus (Chicken) ADDDYGRPGIEKFREEAEERDICIDFSELISQYSDEEEIQQVVEVIQNSTARV
CasR - Cricetulus griseus (Chinese Hamster) ADDDYGRPGIEKFREEAEERDICIDFSELISQYSDKKEIQQVVEVIQNSTAKV
CasR - Cobra cobra (Indian Cobra) ADDNYGRPGIEKFREETEERNICIDFSELIAQYLPEDQIQQVVKVIQNSTAKV
CasR - Salmo salar (Atlantic Salmon) SDDEYGRPGIEKFEKEMEERDICIHLSELISQYFEEWQIQGLVDRIENSSAKV
CasR - Hippocampus comes (Tiger Tail Seahorse) SDDDYGRPGIEKFEKEMEERDICIHLNELISQYMEDHEIQALADRIENSSAKV
CasR - Sinocyclocheilus grahami (Golden-line barbel) SDDEYGRPGIEKFENEMFHRDICIDLNVLISQYIDEAEIRRLADRIENSTAKV
241M
251E
261I
271D
281L
mGluR1 - Homo sapiens (Human) TEGNYGESGMDAFKELAAQEGLCIAHSDKIYSNAGEKSFDRLLRKLRERLPKA
mGluR1 - Mus musculus (Mouse) TEGNYGESGMDAFKELAAQEGLCIAHSDKIYSNAGEKSFDRLLRKLRERLPKA
mGluR1 - Gallus gallus (Chicken) TEGNYGESGMEAFKELAAQEGLCIAHSDKIYSNAGEKSFDRLLRKLRERLPKA
mGluR1 - Cricetulus griseus (Chinese Hamster) TEGNYGESGMDAFKELAAQEGLCIAHSDKIYSNAGEKSFDRLLRKLRERLPKA
mGluR1 - Cobra cobra (Indian Cobra) TEGNYGESGMEAFKELAAQEGLCIAHSDKIYSNAGEKSFEKLLQKLRDRLPKA
mGluR1 - Salmo salar (Atlantic Salmon) TEGNYGESGMEAFKELATQEGLCIAHSDKIYSNAGEKHFDRLLKKLRERLPKA
mGluR1 - Hippocampus comes (Tiger Tail Seahorse) TEGNYGESGMEAFKELASQEGLCIAHSDKIYSNAGEKQFDRLLRKLRERLPKA
mGluR1 - Sinocyclocheilus grahami (Golden-line barbel) TEGNYGESGMEAFKELASQEGLCIAHSDKIYSNAGEKHFDRLLRKLRERLPKA
Helix
Sheet
Helix
CasR Charge Conservation
mGluR1 Charge Conservation
0 10 40 75 95 100
Charged Residue Conservation (%)
b
0 10 40 75 95 100
Charged Residue Conservation (%)
CasR
mGluR1

Figure S4.2 – Alignment of helix-sheet-helix motif and conservation of charged residues in upper lobe.

a Multiple sequence alignment of human CaSR with select orthologs (top), human mGluR1 with select orthologs (middle), and conservation of charged residues for each position (bottom). A conserved helix-sheet-helix structural motif in Class C lower lobe shown in boxes. Negatively charged (red) and positively charged (blue) residues are highlighted. Human sequences for CaSR and mGluR1 used as reference for residue positions. **b** Ribbon representation of CaSR (left, PDB 5K5S) and mGluR1 (right, PDB 1ISR) crystal structures displaying the conservation of charged residues for the upper lobe interface.

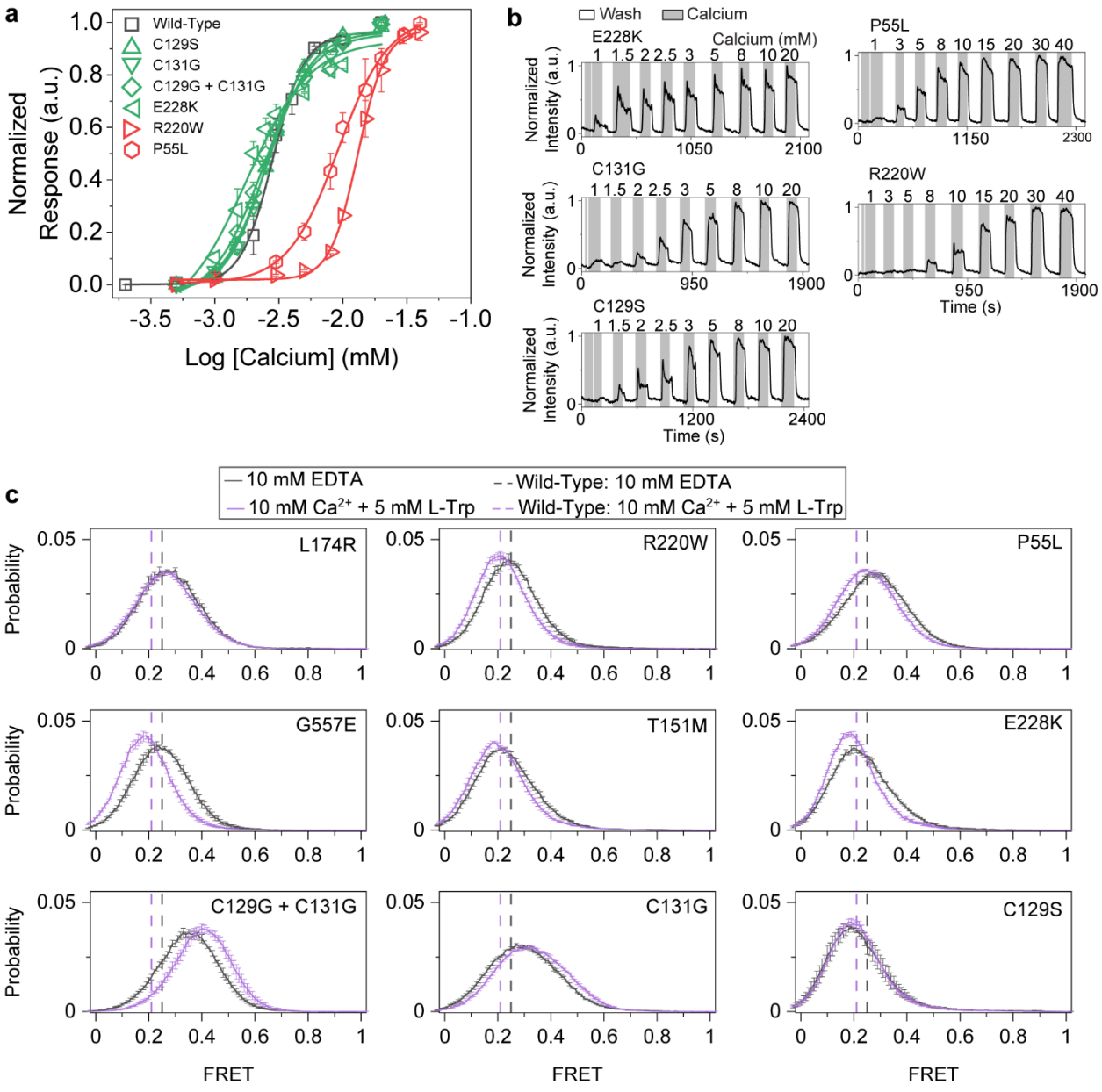
a
Wild-Type
C129S
C131G
C129G + C131G
E228K
R220W
P55L
Normalized Response (a.u.)
Log [Calcium] (mM)
b
Wash
Calcium
E228K
Calcium (mM)
C131G
C129S
P55L
R220W
Normalized Intensity (a.u.)
Time (s)
c
10 mM EDTA
10 mM Ca2+ + 5 mM L-Trp
Wild-Type: 10 mM EDTA
Wild-Type: 10 mM Ca2+ + 5 mM L-Trp
L174R
R220W
P55L
G557E
T151M
E228K
C129G + C131G
C131G
C129S
Probability
FRET

Figure S5.1 – Functional characterization smFRET histograms of CaSR mutants.

a Dose-response curve of wild-type (gray), sensitizing (green), and desensitizing (red) mutations. **b** Cell response traces showing normalized response to increasing concentrations of calcium. Shaded regions indicate times when cells were stimulated with calcium. **c** smFRET population histograms of N-Terminal SNAP CaSR mutants in the presence of 10 mM EDTA or 10 mM Ca^{2+} and 5 mM L-Trp. Dashed lines indicate centers of Wild-Type distributions for reference. Data represent mean ± s.e.m. of n=3 independent biological replicates.

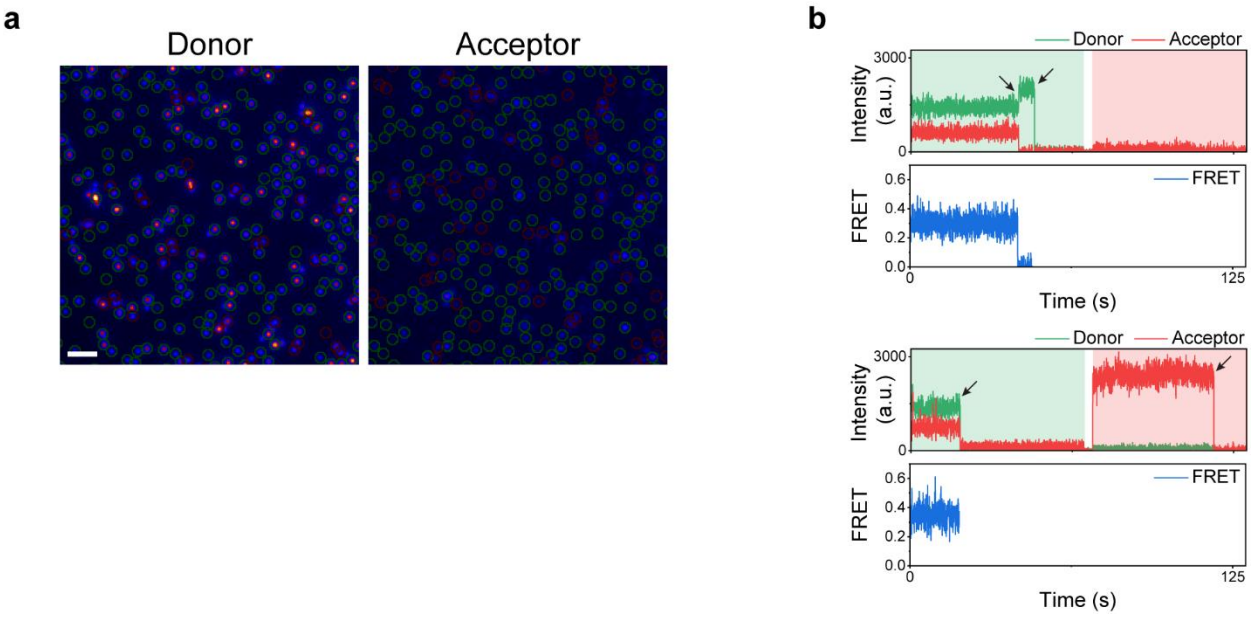

Figure SA1.1 – Functional characterization smFRET histograms of CaSR mutants.

a Sample image of smFRET movie showing the donor channel (left) and acceptor channel (right). Scale bar, 3 μM. **b** Sample single-molecule traces. Shaded regions correspond to excitation by donor (green) and acceptor (red) lasers. Arrows indicate points of single step photobleaching events that demonstrate the presence of a single donor and single acceptor fluorophore.

APPENDIX 2: *calcium-analysis:* An R package for analysis of calcium signaling

PREFACE

The *calcium-analysis* package is a small collection of functions in R that allow users to easily analyze data generated using the calcium sensitive dye – Oregon Green BAPTA-1 AM (OGB1-AM). It contains functions that will normalize intensity trajectories obtained in Fiji[102] if desired and quantify the strength of response to differing ligand concentrations so that a dose-response curve can be determined. It is based on the use of other, well-established, R packages that are widely available. In this section, I explain the utility of the functions and briefly describe their design. A brief description of the package and its functions are available at: https://github.com/FafferMcgee/calcium-analysis.

FUNCTIONALITY

This package assumes that extraction of intensity data from the raw data is done in Fiji. To import the data from Fiji, the data must be in a csv format consisting only of the Area and Integrated density measurements for each region of interest. Fiji will calculate two integrated density values: (1) RawIntDen - the SUM of intensity units in the ROI and (2) IntDen – the MEAN gray values of the ROI * number of pixels in the ROI. There are multiple functions that have the same general utility, and most will fall into two categories: (1) functions that import or import and

normalize raw data from Fiji and (2) quantification of response to differing concentrations of ligand.

PackageInstaller.r

This is a small script in the main github directory that will install the packages I routinely used and some of the dependencies *calcium-analysis* needs to function and the *calcium-analysis* package itself.

Import and Normalization

This is the first step of the workflow and depending upon the goals of the user different import functions can be utilized. In my experience, normalizeCalciumData is the most reliable method, but I have left other normalization methods in the package if desired.

importRawIntData

importRawIntData will read the raw csv data file and perform some minor clean up of the data. First, it will remove the IntDen column leaving only the RawIntDen data and a ‘time’ column that corresponds to the frame number of analyzed movie. The function generates two forms of this data. First, it generates a wide form where each column corresponds to a single ROI and is similar in structure to the raw output from Fiji.

The function will expect a path to a csv file as input, and its output will be a list of the two data frames. A wide data format is the first entry in the list, and a long data format is the second entry in the list.

normalizeCalciumData

normalizeCalciumData is the first step of data analysis and has the same functionality as *importRawIntData*, but it will also normalize each ROI to the equation:

$$Normalized\ Intensity(t) = (I_t - I_{min})/(I_{max} - I_{min})$$

The function will expect a path to a csv file as input, and its output will be a list of the two data frames. A wide data format is the first entry in the list, and a long data format is the second entry in the list.

Visualizing intensity trajectories

plotsCellCalciumData

This function was designed as a wrapper for the *ggplot* function to make visualizing the ROI intensity trajectories less repetitive. It will create a grid visualization using *ggplot*'s *facet_wrap* parameter and element of the grid is an individual ROI. It has parameters pre-defined for formatting the graph and the function expects three arguments as input: (1) *data*: the long-format data (2) *conditions*: a numerical list containing time points where the extracellular condition was changed, and (3) *columns*: an integer value telling the function how many columns to include in the grid.

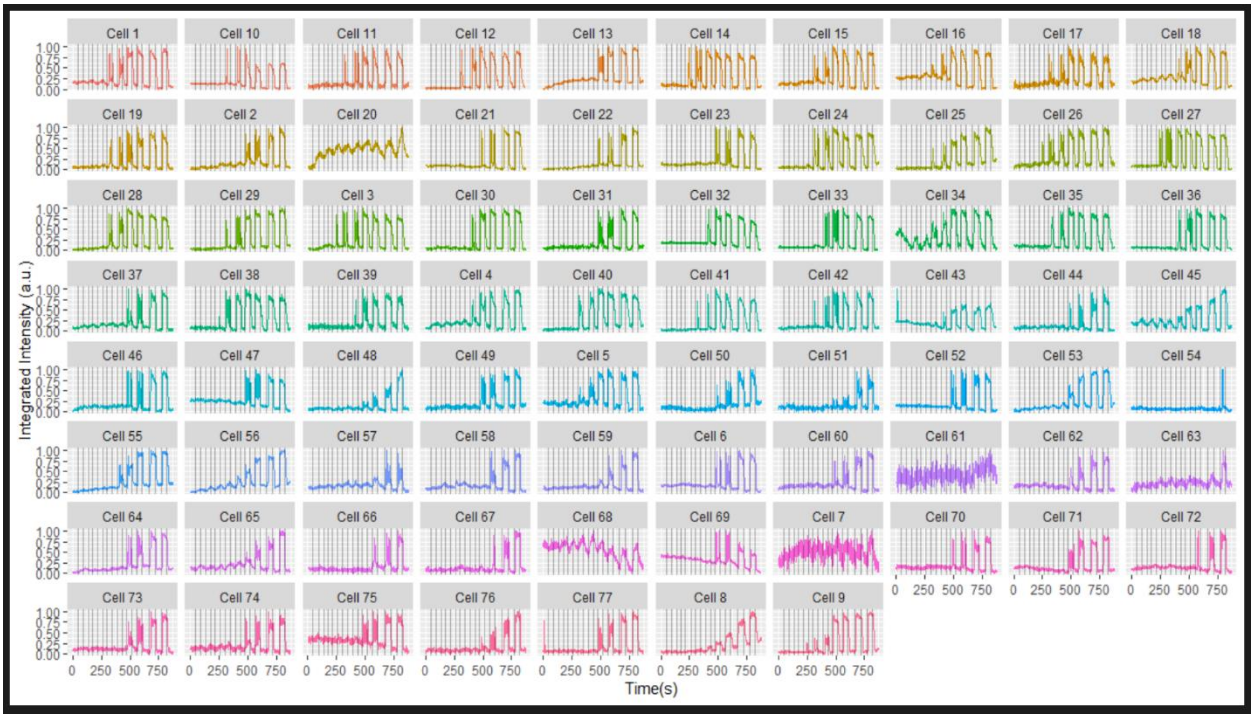

Figure A1.1 – Sample output of plotsCellCalciumData.

plotsRawCalciumData

plotsRawCalciumData functions almost identically to *plotsCellCalciumData*, but it will automatically determine the y-axis limits for each subplot of the figure.

Response Quantification

integrateCurve

Calculates the area under the curve for a specified range. It takes as input a wide-form *dataframe* (where each column is an ROI) and two integer values (*min, max*). The function will

use the *MESS* package to calculate the area under the curve for each column in the data frame between the specified minimum time value and the maximum time value. This integrated response is then normalized to the length of the stimulus window defined by *min* & *max* so that duration of stimulus does not affect the quantified response.

quantDeltaF_Fo

One of the primary downsides to the use of OGB1-AM as a dye is the inability to control for differential loading of the dye into each cell. Because of this, we cannot draw meaningful inferences from the amplitude of the raw data – especially when the data is normalized to [0,1]. I attempted to overcome this limitation by normalizing the fluorescence intensity relative to a baseline calculated by the average intensity immediately preceding stimulation of the cells:

$$Normalized\ Intensity\ (t) = \frac{F_t - F_o}{F_o}$$

Where F_t is the fluorescence intensity at time t and F_o is the mean fluorescence over some window *m* before time *t* such that:

$$F_o = MEAN(F_{t-m}, F_t)$$

The normalized values generated by this method are then integrated to quantify the response. In practice, this seemed to result in a less reliable measure of sensitivity; however, if it is important to quantify a ligand's efficacy, this quantification method may prove useful.

Visualizing the DRC

Fitting to a DRC is done through tools created in the peer-reviewed *drc* package[153]. Please refer to its documentation for a more detailed description of its utility. The output of this function can be visualized with the standard R function *plot* (as is shown in the *sample-analysis* file), but the following functions are useful for visualizing the cell response heterogeneity.

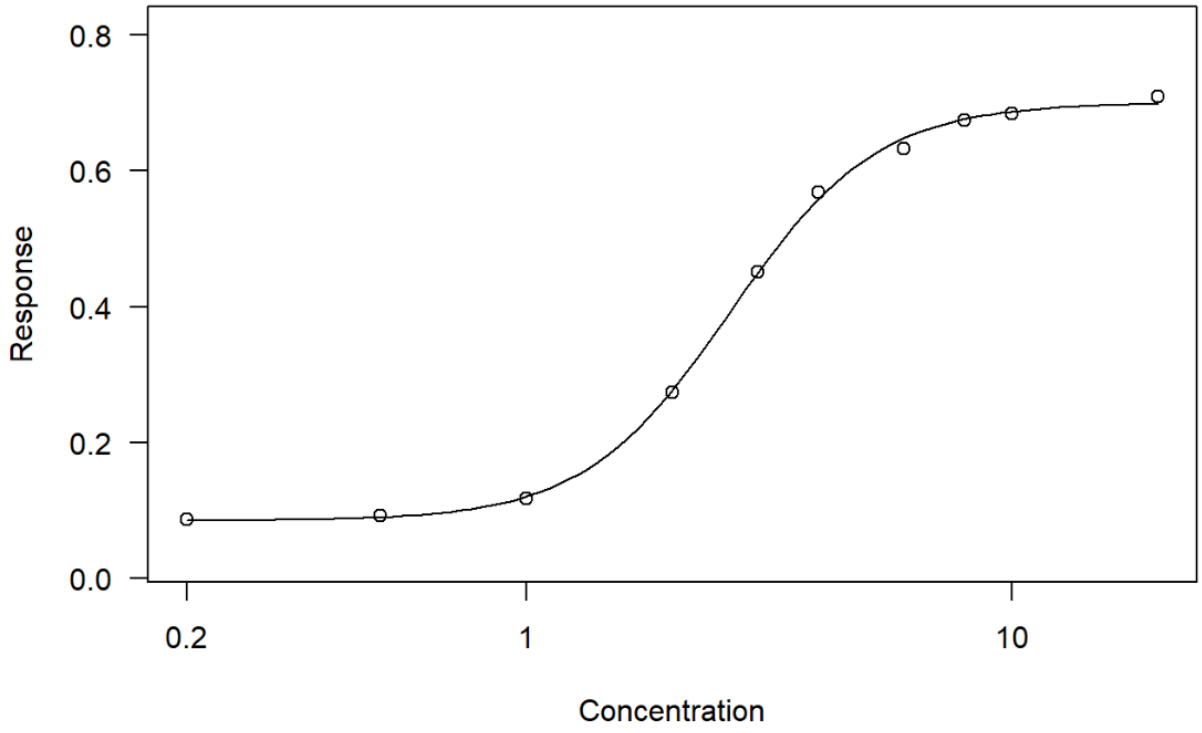

Figure A1.2 – Sample output of the standard *plot* function.

groupsData

When the response of individual cells is quantified, the *groupsData* can be used to classify cells by their response strength. It takes in a long dataframe and will add a new column classifying

cells into weak, medium, and strong responders. This classification looks at the user specified *concentration* and classifies the response based on the user specified values: *firstquartile* and *thirdquartile*. The quartile values can be obtained by using the base R function, *summary* on the dataframe being classified.

plotDRC

plotDRC is a wrapper for function used for a plotting method outlined in the *drc* package. It will plot the DRC with 95% confidence interval as well as data points for individual cells. The color of the data points correspond to the output of the *groupsData* function.

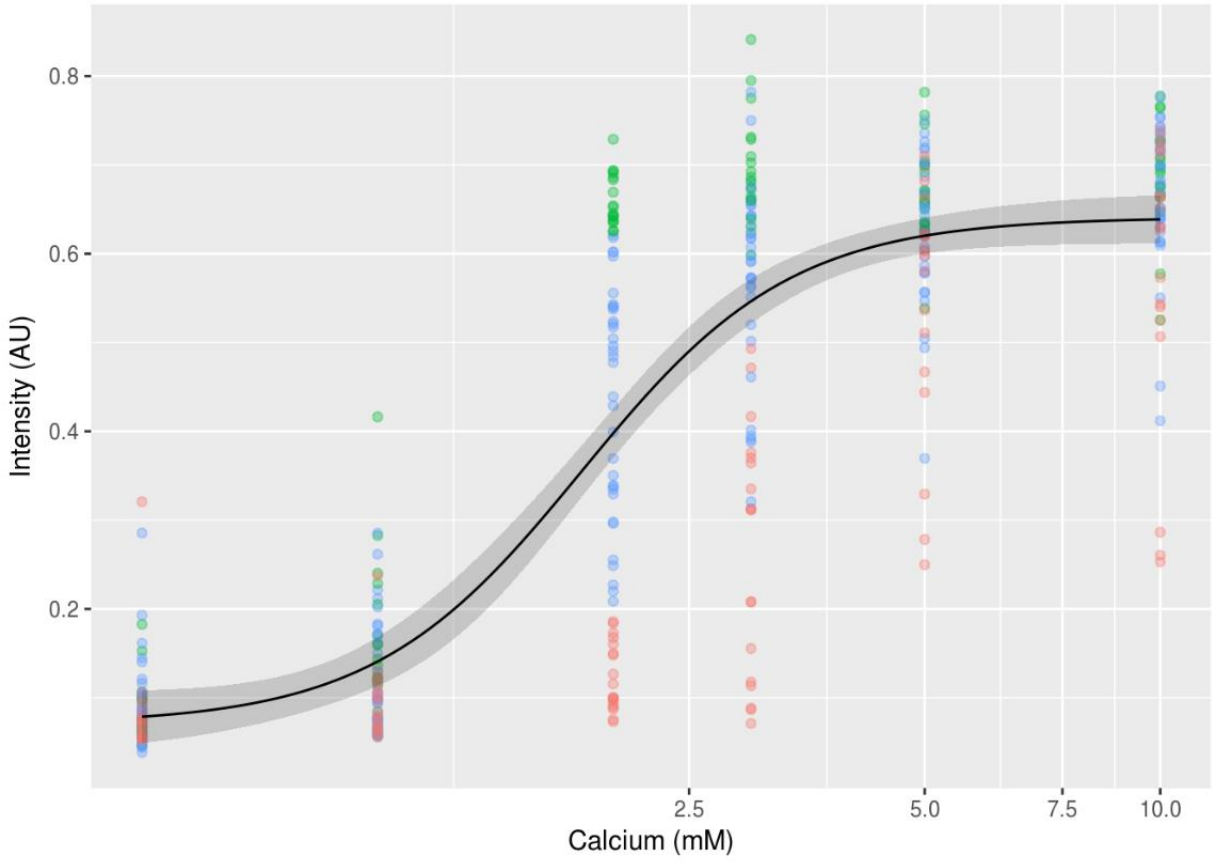

Figures A1.3 – Sample DRC with individual cells plotted.

The black curve represents the dose-response profile and shaded region is the 95% CI for the DRC. Individual data points represent the response of single cells for a given concentration, and the color represents the strength of response (red is weak, blue is medium, green is strong).

sample-analysis.md

Represents a sample workflow in markdown format. It goes through the loading necessary packages, importing and normalizing the data, how to remove cells with undesirable drift or non-responsive cells, response quantification, preliminary dose-response fitting, summarization of results, and the export of data for use in other software – like OriginPro.

RESUME

EDUCATION

Northwestern University, Interdisciplinary Biological Sciences Evanston, IL
Ph.D. in Biological Sciences Expected Aug. 2022

University of California, Santa Cruz Santa Cruz, CA
B.S., Biochemistry & Molecular Biology 2010

PROFESSIONAL EXPERIENCE

Northwestern University Evanston, IL
Ph.D Candidate 2016-Present

- Engineered proteins with unnatural amino acids that are suitable for bioconjugation
- Bioconjugated proteins with fluorophores using unnatural amino acids and click chemistry
- Rationally engineered FRET sensors for different domains of a multi-domain protein
- Assessed conformational dynamics of GPCR activation using single-molecule FRET microscopy
- Developed a single-cell functional assay of GPCR signaling using confocal calcium imaging
- Developed data analysis pipelines using R and Python Jupyter notebooks
- Designed and engineered protein variants for a desired phenotype
- Cultured and transfected HEK293T cells

California Institute of Technology Pasadena, CA
Research Technician 2013-2016

- Purified over 10 proteins weekly via affinity, ion exchange, and size exclusion chromatography
- Performed protein crystallization screens & crystal harvesting for x-ray crystallography
- Transiently transfected & expressed proteins from 20 liters of mammalian cells weekly
- Developed protocol for 96-well PEI transfection utilizing Tecan liquid handling robot
- Optimized polyethylenemine-mediated transfection of HEK2936E suspension cells
- Performed 96-well plasmid mini-prep utilizing a Tecan liquid handling robot

Amgen Thousand Oaks, CA
QC Sr. Associate 2011-2012

- Used qPCR for quantification of host cell genomic DNA in drug substance samples

- Maintained multiple mammalian cell lines such as human erythroleukemia cells
- Assessed the stability of cell lines for cell banks of product cell lines
- Responsible for ordering & organization of materials used in the lab

University of California, Santa Cruz Santa Cruz, CA
Undergraduate Researcher 2009-2010

- Expressed & purified recombinant protein in *E. coli*
- Used isothermal titration calorimetry to determine binding of retinoblastoma to cyclin A
- Created mutants of the retinoblastoma protein using site-directed mutagenesis
- Maintained HeLa cells in anticipation of ChIP assay optimization

PUBLICATIONS

Laiuw, B.W., Foroutan, A., **Schamber, M.R.**, Lu, W., Afsari, H.S., Vafabakhsh, R. (2022) Conformational fingerprinting of allosteric modulators in metabotropic glutamate receptor 2 *eLife* **11:**e78982. (2022).

Schamber, M.R. & Vafabakhsh R. Mechanism of sensitivity modulation in the calcium-sensing receptor via electrostatic tuning. *Nature Communications **13(1)**, 2194.* (2022).

Gristick, H. B., von Boehmer, L., West, A. P., **Schamber, M.**, Gazumyan, A., Golijanin, J., … Bjorkman, P. J. Natively glycosylated HIV-1 Env structure reveals new mode for antibody recognition of the CD4-binding site. *Nature Structural & Molecular Biology* **23(10)**, 906–915 (2016).

Hirschi, A., Cecchini, M., Steinhardt, R.C., **Schamber, M.R.**, Dick, F.A., Rubin, S.M., An overlapping kinase & phosphatase docking site regulates activity of the retinoblastoma protein. *Nature Structural & Molecular Biology* **17(9)**, 1051-1057 (2010).

ABSTRACTS

Schamber, M.R., Vafabakhsh, R. Mechanism of Sensitivity Modulation in a Class C GPCR via Electrostatic Tuning. Abstracts of GPCRs: An Odyssey from Structure, Signaling and Regulation to Therapeutics Keystone Symposia, 2022. Poster presentation.

Schamber, M.R., Vafabakhsh, R. Mechanism of Sensitivity Modulation in a Class C GPCR via Electrostatic Tuning. Abstracts of St. Jude National Graduate Student Symposium, 2022. Oral presentation.

Schamber, M.R., Vafabakhsh, R. Mechanism of Activation & Modulation of the Calcium-Sensing Receptor Revealed by Single-Molecule FRET. Abstracts of the GPCR Retreat, 2019. Poster presentation.

Schamber, M.R., Vafabakhsh, R. Mechanism of activation & modulation of the Calcium-Sensing Receptor. Abstracts of Northwestern Biophysics Symposium, 2019. Oral presentation.

Schamber, M.R., Vafabakhsh, R. Conformational Dynamics of the Calcium-Sensing Receptor Probed by Single-Molecule FRET, 2018. Abstracts of 5th Midwest Single Molecule Workshop, 2018. Oral presentation.

GRANTS & AWARDS

Molecular Biophysics Training Program 2017-2019
National Institute of General Medical Sciences, National Institutes of Health 5T32GM00838